(12)

AFCRL-TR-75-0623

IR WINDOW STUDIES

Ferdinand A. Kröger
John H. Marburger

Electronic Sciences Laboratory
University of Southern California
Los Angeles, California 9000[illegible]

DDC
RECEIVED
APR 9 1976
C

30 September 1975

Final Report for Period
1 September 1974 - 31 August 1975

Approved for public release; distribution unlimited

Sponsored by:

Defense Advanced Research Projects Agency
ARPA Order No. 2055

Monitored by

AIR FORCE CAMBRIDGE RESEARCH LABORATORIES
AIR FORCE SYSTEMS COMMAND
UNITED STATES AIR FORCE
HANSCOM AFB, MASSACHUSETTS 01731

ARPA Order No. 2055

Program Code No. 3D10

Effective Date of Contract:
1 September 1974

Contractor: University of
Southern California

Contract No.

Principal Investigator and Phone No.:
Prof. F. A. Kroger: (213) 746-6224
Prof. John H. Marburger:
(213) 746-6213

AFCRL Project Scientist and Phone No.:
Alfred Kahan: (617) 861-4014

Contract Expiration Date 31 August 1975

Qualified requestors may obtain additional copies from the Defense Documentation Center. All others should apply to the National Technical Information Service.

UNCLASSIFIED

SECURITY CLASSIFICATION OF THIS PAGE (When Data Entered)

18 19 **REPORT DOCUMENTATION PAGE**

READ INSTRUCTIONS BEFORE COMPLETING FORM

1. ~~REPORT NUMBER~~ AFCRL-TR-75-0623

2. GOVT ACCESSION NO.

3. RECIPIENT'S CATALOG NUMBER

4. TITLE (and Subtitle)

6 IR WINDOW STUDIES.

5. ~~TYPE OF REPORT & PERIOD COVERED~~
9 [redacted] - Final ~~for~~ rept.
~~Period~~ 1 Sept. 74-31 Aug 75

6. ~~PERFORMING ORG. REPORT NUMBER~~

7. AUTHOR(s)

10 Ferdinand A. Kröger
John H. Marburger

8. CONTRACT OR GRANT NUMBER(s)

15 F19628-75-C-0080
VARPA Order-2055

9. PERFORMING ORGANIZATION NAME AND ADDRESS

University of Southern California
Electronic Sciences Laboratory
Los Angeles, California 90007

10. ~~PROGRAM ELEMENT, PROJECT, TASK~~ AREA & WORK UNIT NUMBERS

Project # 5621-08-03
~~DoD Element 61101D~~

11. CONTROLLING OFFICE NAME AND ADDRESS

Air Force Cambridge Research Labs (LQ)
Hanscom AFB, Massachusetts 01731
Contract Monitor: A. Kahan/LQS

12. ~~REPORT DATE~~ 11 30 Sept. 1975

13. ~~NUMBER OF PAGES~~ 131

14. MONITORING AGENCY NAME & ADDRESS (if different from Controlling Office)

16 AF-5621 17 562108

15. SECURITY CLASS. (of this report)

UNCLASSIFIED

15a. DECLASSIFICATION/DOWNGRADING SCHEDULE

16. DISTRIBUTION STATEMENT (of this Report)

A--Approved for public release; distribution unlimited

12 136p.

17. DISTRIBUTION STATEMENT (of the abstract entered in Block 20, if different from Report)

18. SUPPLEMENTARY NOTES

This Research was sponsored by Defense Advanced Research Projects Agency ARPA Order No. 2055

19. KEY WORDS (Continue on reverse side if necessary and identify by block number)

IR Windows	II-VI Semiconductors
Alkali Halides	Thermal Lensing
III-V Semiconductors	IR Absorption

20. ABSTRACT (Continue on reverse side if necessary and identify by block number)

This document describes the results of a variety to studies of IR window materials and systems performed at the University of Southern California during 1974-75. The studies fall under three categories: A) IR window material characterization, B) IR window failure mechanisms, and C) window system evaluation. Projucts under A include applications of scanning cathodoluminescence microscopy, thin foil transmission electron microscopy, and IR over

DD FORM 1 JAN 73 1473 EDITION OF 1 NOV 65 IS OBSOLETE
S/N 0102-014-6601

UNCLASSIFIED

SECURITY CLASSIFICATION OF THIS PAGE (When Data Entered)

361 620 LB

Block 20 (cont'd.)

absorption spectroscopy to window materials characterization. Emphasis was on semiconductor materials, including ZnSe, CdTe and GaAs. Measurements of strain optic coefficients were performed on GaAs, and the temperature and frequency dependence of the refractive index of ZnSe was determined precisely. A surface acoustical wave technique for distinguishing between bulk and surface absorption was perfected and applied to uncoated KCl window samples.

Projects in category B included examination of the effect of reactive atmospheres on alkali halide window materials, and extensive measurements of optical breakdown properties at 10.6μm. Window system evaluation work included the estimation of induced birefringence effects in polycrystalline windows, and quantitative experiments on thermal lensing.

CONTENTS

Page

ABSTRACT i

1. INTRODUCTION 1

2. PROGRESS BY PROJECT

A. Materials Characterization

Scanning Electron Beam Studies of Laser Window Materials*(D.B. Wittry) 2

An Electron Microscope Investigation of the Structural Imperfections in II-VI Compounds (CdTe and ZnSe). (G.H. Narayanan and S.H. Rustomji) 9

Absorption Studies of CdTe and ZnSe. (W.G. Spitzer and B.V. Dutt) 15

Study of Defects in II-VI Compounds. (F.A. Kröger, F.A. Selim and A. Ray) 30

Optimization of Alkali Halide Window Materials* (P.J. Shlichta, J.F. Yee and E.A. Miller) 37

Strain-Optic Coefficients* (W. Steier, R. Joiner, C.P. Christensen) 55

Theoretical Studies of Absorption Mechanisms in IR Window Materials. (R.W. Hellwarth and M. Mangir) 58

Surface Studies with Acoustic Probe Techniques* (J.H. Parks and D.A. Rockwell) 60

B. Window Failure Mechanisms

The Interaction Between Alkali Halides and Chemically Active Transient Species* (C. Wittig) 70

Pulsed 10.6μ Laser Damage Studies. (M. Bass and K.M. Leung) 77

C. Window System Evaluation

Thermal Lensing. (W. Steier, C.P. Christensen, R. Joiner) 108

Strain Optic Tensors for Polycrystalline Aggregate Materials. (J. Marburger and M. Flannery) 113

3. DISCUSSION 125

4. PUBLICATIONS AND PRESENTATIONS 128

INTRODUCTION

The reports which follow describe work performed prior to September 1, 1975, and the titles of projects which terminated on that date are followed by an asterisk. The reports for such projects are final. Other projects are still in progress, and this is reflected in the reports. The reader wishing to obtain an overview of the work described here will find the summary and discussion (page125)helpful. Additional material on each project may be found in the semiannual technical report AFCRL-TR-75-0236 (15 March 1975) and in prior reports published in connection with the USC Infrared Window Program. The final report for the previous contract period appeared as AFCRL-TR-74-0557 (15 Sept. 1974).

Scanning Electron Beam Studies of Laser Window Materials

D.B. Wittry

This research is concerned with three methods of characterizing potential materials for laser windows, namely: Scanning Electron Microscopy (SEM), Scanning Cathodoluminescence Microscopy (SCM), and modulation of cathodoluminescence or specimen currents by illumination with photons of less than band gap energy. By these techniques, we can obtain information concerning surface topography, grain size in polycrystalline materials, and energy levels in the forbidden energy gap.

During the past 6 months, the following was done:

(1) Study of grain structure of Raytheon ZnSe by Cathodoluminescence scanning microscopy

In order to obtain suitable damage-free surfaces for these investigations, four different etchants were evaluated. These include the following:

a) 0.5% Br_2 in CH_3OH (ref. 1)

b) 3 parts HNO_3 + 1 part HCl (ref. 1)

c) 900ml H_2O + 270gm $K_3Fe(CH)_6$ + 5.5g KOH (ref. 2)

d) 40 parts HCl + 4 parts H_2O (30%) + 1 part H_2O (ref. 3)

For the present work, an etchant is desired that removes surface damage while producing a minimum of preferential attack or surface staining. Of the etchants investigated we found that etchant (d) worked best. Cathodoluminescence and backscattered electron images of a typical specimen treated with this etchant for 90 seconds are shown in Fig. 1a and 1b.

The significance of these results for evaluation of practical laser window materials may be summarized as follows:

i. Grain boundaries are clearly revealed in the cathodoluminescence images because of non-radiative recombination of excess carriers at these boundaries. A comparison of Figs. 1a and 1b show that the cathodoluminescence image does not show any contrast due to twinning, i.e. there is no change in cathodoluminescence efficiency on either side of a twin boundary or at the boundary itself. The backscattered electron image however, shows different contrast on either side of a twin boundary (this contrast may be due to preferential etching, or to electron "channeling" effects). Optical metallography of etched surfaces also tends to reveal twin boundaries as well as grain boundaries. Therefore, for purposes of characterizing polycrystalline laser window materials consisting of direct gap semiconductors, cathodoluminescence scanning images are superior to images obtained by the optical metallograph, or by the scanning electron microscope using secondary or backscattered electrons. The cathodoluminescence images of a scratch free surface could be used directly in image analyzing computers for determining grain structure parameters such as average size, size distribution, and shape parameters.

ii. Inclusions also produce contrast in cathodoluminescence images. These appear as dark regions, similar to grain boundaries and often may be seen as a widening of the grain boundaries. or as dark areas at the point of intersection three grain goundaries. Statistics concerning the number and size of these inclusions could also be obtained by use of image analyzing computers.

iii. Because of non-radiative recombination in damaged regions, residual damage due to mechanical polishing will be observable in cathodoluminescence images even though this damage may be invisible by ordinary metallography or SEM. Thus, cathodoluminescence images should be an important tool in the study of laser induced damage. For example one could confirm that the statistics in laser damage experiments[4] are related to the probability that the laser beam strikes a grain boundary, an inclusion, or a region of sub-surface damage.

(2) Study of deep levels in ZnSe by light modulated specimen current

In these experiments, we have used small single crystals of ZnSe and the technique previously reported[5-7] in which the specimen is irradiated simultaneously by photons of varying energy and by a focussed electron beam using a modified electron probe x-ray microanalyzer. This previous work has shown that for semi-insulating specimens the changes in specimen current may be correlated with the changes in specimen resistivity due to the optical illumination. Because of the generation of excess carriers by x-rays absorbed in the bulk of the specimen during electron bombardment[8], both "enhancement" and "quenching" effects may be observed in a manner similar to photoconductivity experiments using simultaneous irradiation with photons of two different energies[9,10].

A light-modulated specimen current spectrum for "undoped" ZnSe[11] is shown in Fig. 2. This spectrum appears to exhibit thresholds for enhanced specimen current at photon energies of 2.127 eV, 2.231 eV, ~2.40 eV, and ~2.54 eV and a threshold for decrease of specimen current at ~2.59 eV. For comparison, the cathodoluminescence spectrum of another specimen of ZnSe is shown. This exhibits a single peak at a value close to the band gap energy (the precise relationship of the photon energy and the peak in the cathodoluminescence spectrum will depend on the dominant radiative recombination mechanism (i.e. band to band, radiative decay of excitons, band to shallow impurity level, etc.).

The interpretation of these experiments must take account of the difference in mobility of holes and electrons, and also the different lifetime of these carriers. For similar experiments on GaAs, it was proposed[7] that enhancement effects ($\Delta I_s/I_s$ increasing with increasing photon energy) were due to excitation of electrons from a deep acceptor level to the conduction band. For Cr doped GaAs, the lifetime of holes is small because of strong hole trapping at the occupied Cr levels and the mobility of holes is also small. Thus, illumination by light of energy $h\nu_1$, as shown in Fig. 3 will increase the average electron carrier density and decrease specimen resistivity. When the specimen resistivity decreases, the IR drop across the specimen is reduced and the beam landing energy is increased. Thus, the secondary electron yield will be reduced and I_s will increase.

For a photon energy $h\nu_2 \geq$ the energy to excite an electron from the valence band to a donor level, excess holes will be generated; these excess holes will cause the occupation of the Cr levels to decrease, resulting in a larger number of electrons being trapped at the Cr levels/second and a decrease of electron lifetime. Since $\mu_e >> \mu_h$, the net result will be a decrease in photoconductivity for $h\nu_1 > h\nu_2$. We believe that a similar explanation may account for the present results since in ZnSe $\mu_e \approx 10\mu_h$[12].

On this basis assuming Eg = 1.667 eV we would interpret the present results as indicating acceptor levels at $E_V + E_A$ where $E_A = 0.54$, and (with possible additional levels at 0.44 ~0.27 and ~0.13 eV. The level at $E_A = 0.54$ may be that due to a Zn vacancy as previously reported[13]. A donor level at E_C 0.075 eV also would be indicated by our present results.

The nature of the levels and also their location in the energy band gap would be modified if other possible levels are considered (for example levels due to double acceptors or double donors). Nevertheless the present work indicates the possibilities of this technique for study of deep energy levels in ZnSe.

References

1. B. Tuck, J. Mat. Sci. 10, 321-339 (1975).
2. Suggested by Hughes Research Laboratories.
3. Suggested by H. Narayanan.
4. D. Milan, R.A. Bradbury, R.H. Picard, and M. Bass, National Bureau of Standards Spec. Pub. 414, p. 189.
5. W.N. Lin and D.B. Wittry, Bull. Am. Phys. Soc. II-17, 1194 (1972).
6. W.N. Lin and D.B. Wittry, Proc. 8th National Conference on Electron Probe Analysis, New Orleans, La., Paper No. 73.
7. W.N. Lin and D.B. Wittry, submitted to J. Appl. Phys.
8. D.B. Wittry and C.J. Wu, Proc. 8th Annual SEM Symposium, IIT Research Institute, 1975, pp. 441-446.
9. R.F. Broom. J. Appl. Phys. 38, 3483 (1967).
10. D.R. Heath, P.R. Selway, and C.C. Tooke, J. Phys. D. (Appl. Phys.), 1, 29 (1968).
11. Eagle Picher Industries, Inc. Miami, Oklahoma.
12. J.L. Heaton III, et at, Appl. Letters 20, 333 (1973).
13. G.B. Stringfellow and R.H. Bube, Phys. Rev. 171, 903 (1968).

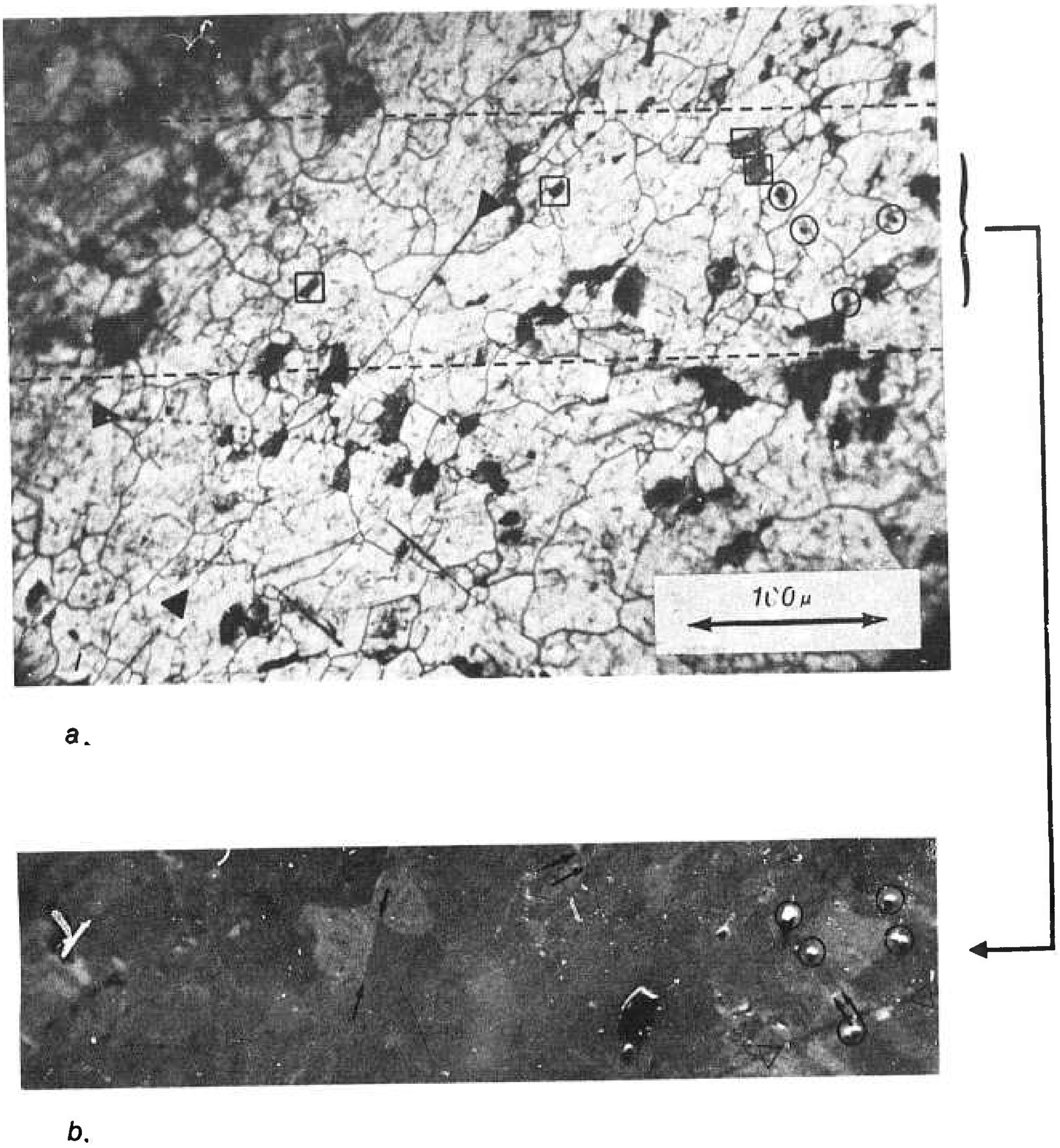

Figure 1. Cathodoluminescence image (a) and backscattered electron image (b) of Raytheon ZnSe. By comparison of the two images it is possible to identify grain boundaries (network of black lines in a), twin boundaries (arrows in b), surface scratches (∇ in b), sub-surface damage (▲ in a), inclusions (◻ in a), and surface particles (o in a and b).

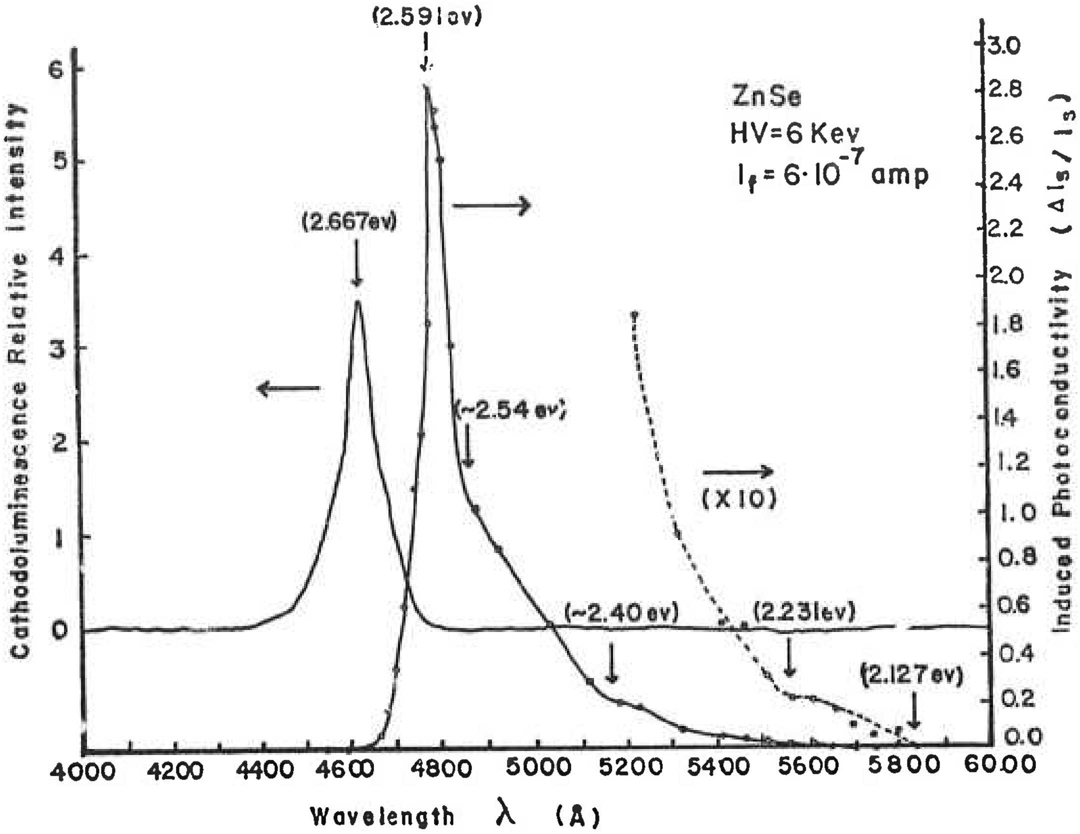

Figure 2. IR modulated specimen current spectrum of single crystal ZnSe compared with cathodoluminescence spectrum (Raytheon ZnSe).

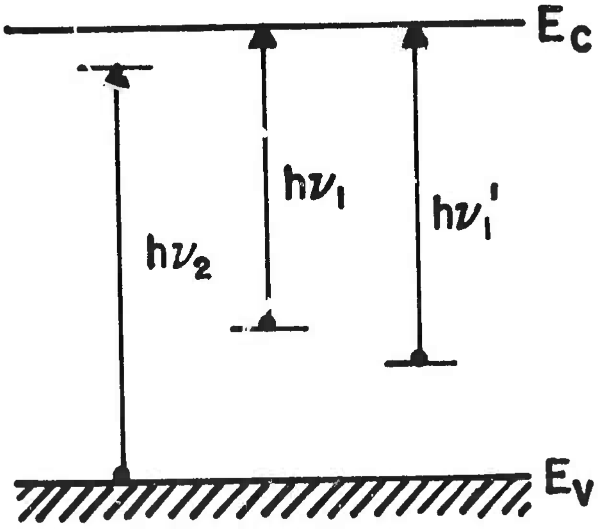

Figure 3. Models for transitions giving thresholds for enhancement ($h\nu_1$) and quenching ($h\nu_2$) of specimen current.

An Electron Microscope Investigation of the Structural Imperfections in II-VI compounds (CdTe and ZnSe)

G.H. Narayanan and S.H. Rustomji

It is the goal of this part of the research program to investigate the effects of both donor (Al,Ga,In,B etc.) acceptor (P,As,Sb etc.) impurities on the defect structures of CdTe and ZnSe and to determine how they are influenced by post-growth annealing treatments. The identification and characterization of the lattice defects are being carried out by using thin foil transmission electron microscopy. In continuation of the program as described in the previous report, the work in this period was concentrated on (i) CdTe doped with different concentrations of P and on (ii) undoped ZnSe which has been subjected to various annealing treatments under both excess Zn and excess Se atmospheres.

CdTe:P

CdTe ingots with phosphorus concentrations of 5×10^{19}, 5×10^{18}, 2×10^{17} and $5 \times 10^{16} cm^{-3}$ were grown by horizontal Bridgman method and provided to us by Dr. B.V. Dutt of our laboratory. Specimens from all the crystals were thinned to electron transparency by a chemical jet polishing technique using a solution containing 10ml HNO_3, 20ml H_2O and 4gr $K_2Cr_2O_7$. This solution was found to yield better results than the one reported by us previously (1). All CdTe:P crystals were virtually free of defects such as stacking faults, twins and precipitates. The average dislocation density in these crystals was estimated to be the order of $\sim 10^4/cm^2$. In the case of the crystal containing $5 \times 10^{19}/cm^3$ of P, some decoration of the dislocations by precipitates was observed; however no precipitates were present in the matrix. An example is shown in Fig. 1. These observations indicate that P can form solid solutions with CdTe at least up to a concentration of $5 \times 10^{19}/cm^3$. In addition to the P-doped CdTe, we have also examined the microstructure of CdTe doubly doped with P and In. The diffusion of In into P-doped CdTe has been found to produce a dispersion of fine precipitates throughout the matrix as shown in Fig. 2. Since no diffraction effects attributable to these precipitates appeared in the selected area electron diffraction patterns, positive identification of the crystal structure and composition of these precipitates could not be made.

A series of other ingots with double doping such as P + Ga, P + Ag and P + Cu will be examined shortly. It is also proposed to examine the microstructure CdTe:P crystal when annealed at different temperatures under several different partial pressures of Cd. As reported in section C.1 of previous report (2) these annealing treatments are known to have significant effects on the electrical properties of CdTe:P.

ZnSe

In the previous report (1) it was shown that the microstructure of as-received polycrystalline ZnSe grown by chemical vapour deposition contained a host of lattice defects such as massive inclusions, fine precipitates, stacking faults, twins and a high density of dislocations. In order to examine how these defects are affected by post-growth heat treatments, as-grown crystals were annealed at 880°C under excess Zn and excess Se atmospheres for ~5 hrs. A partial pressure of 0.5 atm was used in both cases. Annealing under both Zn and Se atmospheres caused appreciable grain growth to occur and the elimination of most of the massive inclusions and precipitates originally present. Virtually no stacking faults were observed in either of these crystals. There was also a significant reduction in the density of dislocations and twins. During annealing under Zn partial pressure, residual dislocations appeared to form three dimensional networks [Fig. 3(a)] and subboundary walls through fine poligonization [Fig. 3(b)]. The isolated dislocations were often found to be decorated with precipitates as shown in Fig. 4. An extremely small volume fraction of precipitates was also found distributed in the matrix. Owing to their small size and volume fraction, no positive identification of these precipitates could be made. In comparison to the crystals annealed under Zn atmospheres, those annealed under Se atmospheres exhibited lower dislocation densities. Furthermore, no precipitates were observed in these crystals.

During the remainder of this contract period, we propose to initiate examination of ZnSe doped with various concentrations of Al and to study the effects of various annealing treatments on their defect structures.

References

1. G.H. Narayanan and S.H. Rustomji, "I.R. Window Studies" Ed: F.A. Kroger and J.H. Marburger, USC Semi-annual Technical Report #1, (March 15, 1975), AFCRL-TR-75-0236 pp. 8-15.
2. F.A. Kroger and F.A. Selim, "I.R. Window Studies", USC Semi-annual Technical Report #1 March 1 (1975) AFCRL-TR-75-0236 pp. 16-23.

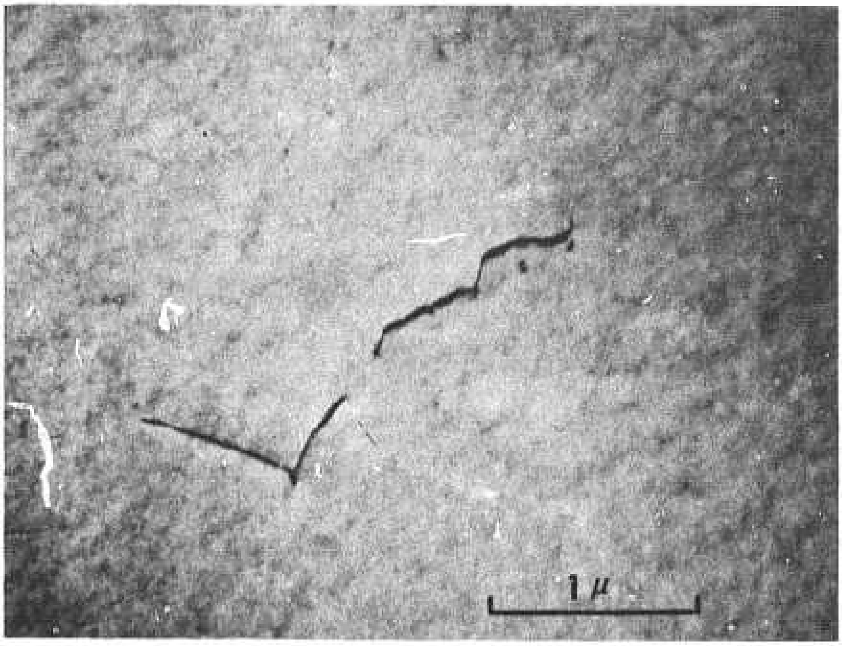

Figure 1 Brightfield electron micrograph of as-grown CdTe crystal doped with 5 x 10^{19}cm^{-3} of P, showing the pinning of dislocations by fine precipitates.

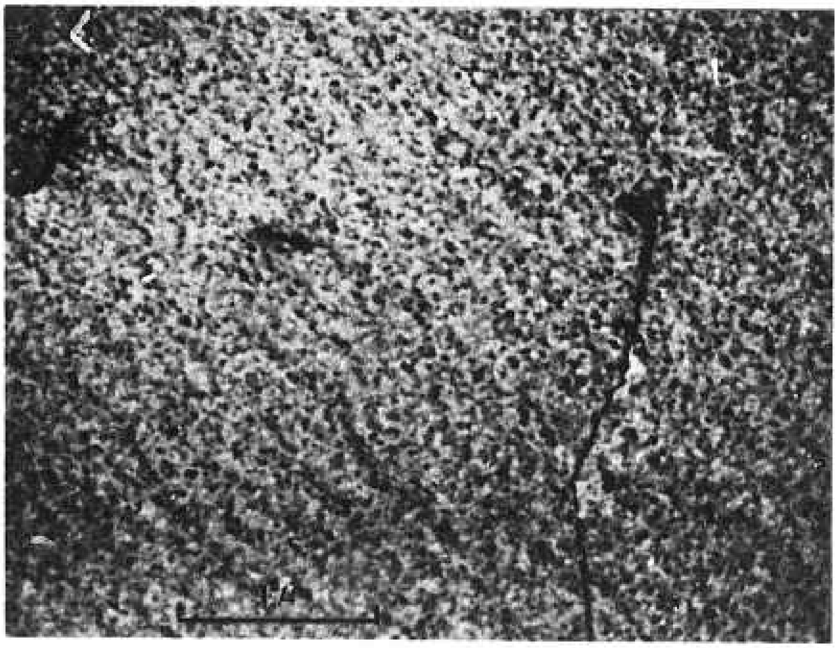

Figure 2 Microstructure of CdTe doubly doped with P and In, in the as-grown condition showing the presence of fine precipitates.

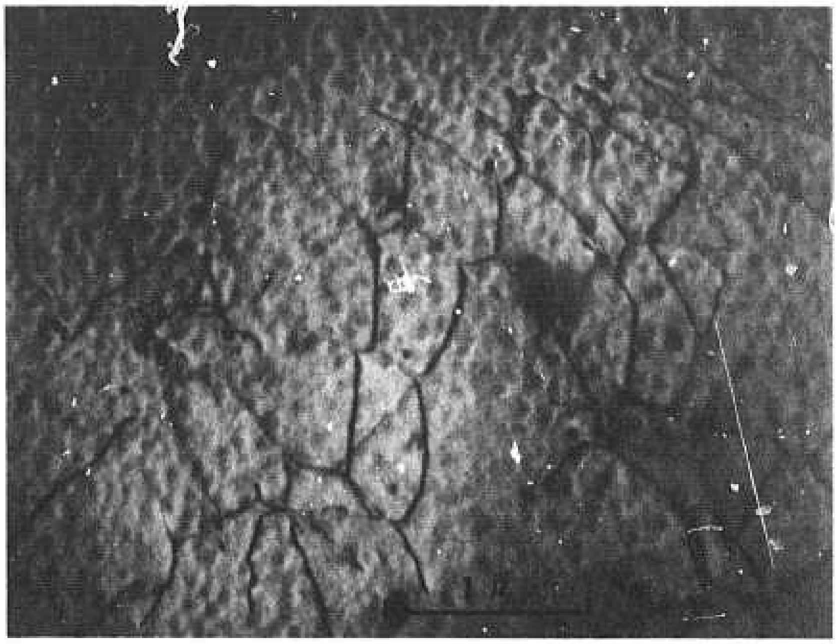

Figure 3(a) Three-dimensional hexagonal dislocation network in CVD grown undoped ZnSe following annealing at 885°C for 5 hours under Zn partial pressure of 0.5 atoms.

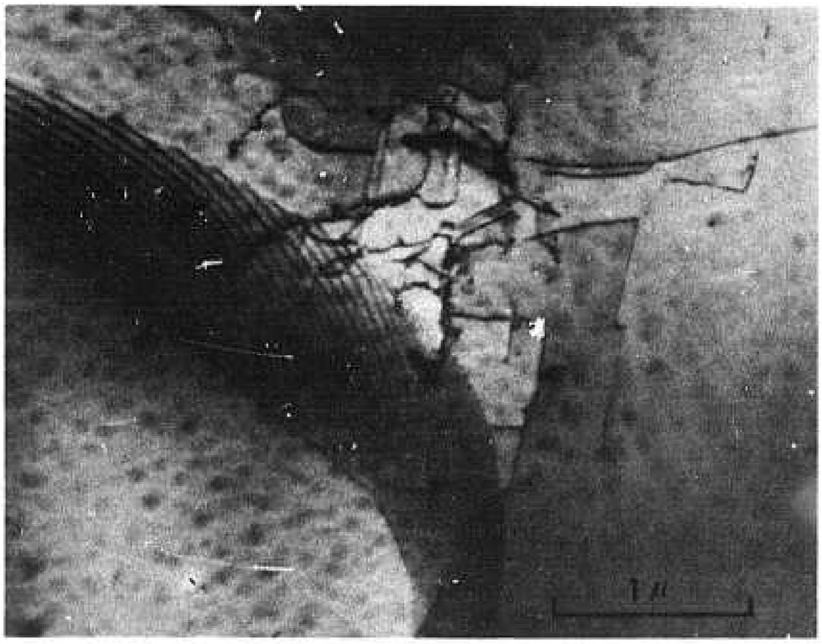

Figure 3(b) Low angle boundary formed by polygonization of dislocations in the same material as in Fig. 3(a).

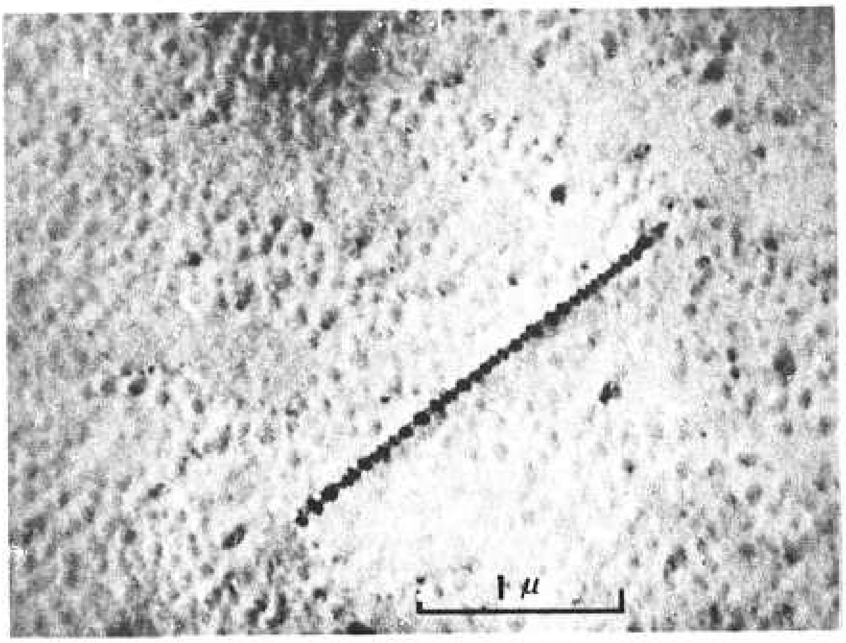

Figure 4 A brightfield micrograph showing the decoration of dislocations by precipitates in CVD-grown ZnSe which has been annealed at 885°C for 5 hours under a Zn-partial pressure of 0.5 atm. A small density of precipitates can also be seen distributed in the matrix.

Absorption Studies of CdTe and ZnSe

W. G. Spitzer and B. V. Dutt

This part of the report deals with the studies of impurity related absorption in CdTe and ZnSe. To avoid repeated reference to the previous progress reports, a background and summary section is provided to highlight the objectives of the investigation and to summarize some of the results given in the previous reports. This is followed by the results of work during the six month period ending August 31, 1975.

A. Background and Summary of Our Previous Work.

There are various factors which limit the transparency of the II-VI compounds, in particular CdTe and ZnSe, preventing them from attaining the theoretically predicted values. The emphasis here is primarily on the study of the impurity-induced localized vibrational modes (LVM) in CdTe and ZnSe and the influence of these modes on the infrared transparency. Attention will be paid to other factors such as multiphonon absorption, absorption due to precipitates or clusters of impurities or native defects, and free carrier absorption due to electrons and holes, as they are encountered.

In view of the emphasis on impurity related absorption, the studies are primarily on purposely heavily doped materials. The dopants chosen are usually light compared to the host atoms, since the lighter elements give rise to spatially localized vibrational modes (LVM) lying above the maximum phonon frequencies of the host lattice. Cubic CdTe and ZnSe have the zinc blende structure with all the lattice and primary interstitial sites having tetrahedral coordination. A substitutional or interstitial impurity at these T_d sites which satisfies the necessary conditions relating to mass and force constants is expected to cause a LVM which is triply degenerate. This would be the situation for light isoelectronic substitutional impurities, i.e. impurities of the second or sixth group of the periodic table, such as Mg or S.

For aliovalent impurities, the II-VI compounds are known to exhibit self-compensation to varying degrees depending on the thermodynamic history of the sample. Generally, for donor doped CdTe and ZnSe where the donor has a preference for the group II site, the material would be more compensated if the conditions during crystal growth or post growth annealing correspond to a low vapor pressure of the metal component (or equivalently a higher vapor pressure of the nonmetal component). The usual acceptors Cu, Ag, Au or P seem to exhibit amphoteric behavior, and no simple rules for the degree of compensation in these cases can be given.

1. In the case of lighter donor dopants such as Al on the group II site, the self-compensation appears to be due to native metal site vacancy acceptors V_M'' and their complexes with the $Al_M^{\cdot}$ donors.(1) The two species in a complex such as Al_M-V_M have C_s point group symmetry, and the triple degeneracy of the Al_M mode is totally lifted. As a result one observes four localized vibrational modes in all, one from Al_M and three from the pair defect. Indeed, our infrared measurements(1) on the system CdTe:Al support this model. The following assignments have been made: Al_{Cd}, T_d, 299 cm^{-1}; Al_{Cd}-V_{Cd}, C_s, 282, 287, and 326 cm^{-1}. To help identify and make these assignments we have carried out some studies on double-doped systems such as CdTe:Al, X, X being Sb, Cu, Ag or Au. A full account of the details is reported elsewhere.(1) A study of the annealing behavior of CdTe:Al under Cd-rich conditions indicated free electron absorption with α varying as ν^{-3} and ν^{-4}. These results were interpreted in terms of polar optical mode scattering and ionized impurity scattering,(1,2) with the former being the dominant mechanism.

2. In addition to CdTe:Al, another system chosen for study was CdTe:P. Initially, in heavily doped CdTe:P, i.e. $[P] = 5 \times 10^{19}/cc$, we observed LVM due to phosphorus at 269, 308

and 322 cm^{-1} at $80^{o}K$. These three modes were of nearly equal strength. As we lowered the [P] from 10^{19} cm^{-3} to 10^{16} cm^{-3} range we observed the following: In 10^{18}/cc range we again observed the three bands with nearly equal strengths. Although the data is not sufficient to be convincing, it appears that the strengths are not directly related to the total phosphorus concentration. At lower [P] the three bands were seen to vary considerably in strength relative to one another. Therefore, it is clear that the phosphorus is present in more than one species, although the identification of the various species is uncertain. A sample from the tail end section of the most heavily doped ingot, $[P] = 5 \times 10^{19}$/cc, showed an absorption coefficient of $4 \times 10^{-3} cm^{-1}$ at 10.6μm, suggesting that the various phosphorus species are self compensating. These species may involve complexes with native defects; however, we have not found any clear evidence for such complexes. Our attempts to identify the species with the aid of annealing treatments with controlled Cd and Te atmospheres have not provided information that would help identify the species.

3. A third system chosen for study was the ZnSe:Al system. It is somewhat different from CdTe:Al in that the number of bands observed is six, and this is not compatible with only Al_{Zn} and Al_{Zn}-V_{Zn} complexes while, as discussed, the four bands observed in CdTe:Al are satisfactorily accounted for in terms of these defects. Mitsuishi et al.[3] originally observed six localized vibrational modes in ZnSe:Al at 339, 342, 346, 359, 388 and 393 cm^{-1}. They assigned the 359 cm^{-1} band to the unassociated Al_{Zn} (T_d) species. The origin of the other five bands is not totally clear. Our measurements confirm these observations. We also carried out diffusion anneals of Cu, Ag and Au into ZnSe:Al. The behavior of Cu and Au indicated complexes Al_{Zn}-Cu_{Zn} and Al_{Zn}-Au_{Zn} with C_s symmetry, while for Ag either Al_{Zn}-Ag_i or Al_{Zn}-Ag_{Se} complexes with a C_{3v} symmetry were indicated. In all these double doped systems, we also

observed the unassociated Al_{Zn} (T_d) mode at 359 cm^{-1}, which supported the assignment made by Mitsuishi et al.$^{(3)}$ A full account of the local mode studies of the above mentioned systems may be found in reference (4).

Annealing of ZnSe:Al in Zn vapor leads to free electron absorption with $\alpha \sim \nu^{-3}$ behavior. Results of annealing of ZnSe:Al with different Al doping levels will be described in a later section.

B. Results Obtained During the Present Progress Report Period.

1. CdTe:Al

Since the studies on CdTe:Al were fairly conclusive, the results were submitted in a paper which has been accepted for publication in the Journal of Applied Physics.$^{(1)}$

2. CdTe:P

Fig. 1 gives the absorption spectrum of CdTe:P ($[P] \approx 5 \times 10^{19} cm^{-3}$) in the II harmonic region. The strongest features are seen at 535 cm^{-1} and 639.5 cm^{-1}, which are nearly twice the fundamental frequencies at 269 and 322 cm^{-1}. This is consistent with the assumption that the two sites are of tetrahedral symmetry (T_d). However, there is no indication of any features related to the 308 cm^{-1} in the second harmonic region. Fig. 2 gives the absorption spectrum in the III harmonic region. The number of peaks observed is not easily interpreted in terms of simple symmetry arguments. We have not completed our analysis of these spectra and can not arrive at plausible assignments at this time.

The absorption at the 10.6μ region as seen from Fig. 2 is about 0.1 cm^{-1}. However, calorimetric measurements with a CO_2 laser on a sample from an adjacent section of the ingot resulted in $\alpha \approx 4 \times 10^{-3} cm^{-1}$. This conflict is being investigated.

It is often helpful to introduce another compensating impurity in a material. Since P is an acceptor in CdTe, we chose In, Ga and Al as counterdopants. Cu was also chosen, as it is known to exhibit amphoteric behavior. Figs. 3, 4, 5 and 6 show the spectra of CdTe:P+In, CdTe:P+Ga, CdTe:P+Al and CdTe:P+Cu, respectively. The following is a list of bands observed in each of these systems (see Figs. 3-6).

(1) CdTe:P,In: 269, 305, 308, 322, 331.5 cm^{-1};
(2) CdTe:P,Ga: 269, 301.5, 308, 322, 352.5, 357.5 cm^{-1};
(3) CdTe:P,Al: 269, 302, 308, 322 cm^{-1};
(4) CdTe:P,Cu: 275.5, 297.5, 322, 329 cm^{-1}.

These bands are schematically represented with their peak positions in Fig. 7.

In these systems one would expect the following complexes: In_{Cd}-P_{Te}, Ga_{Cd}-P_{Te}, Al_{Cd}-P_{Te}, Cu_i-P_{Te}, all with C_{3v} symmetry. If one assumes that the 322 cm^{-1} is due to P_{Te}, then the C_{3v} pair splits the 3-fold degeneracy of P_{Te} (T_d) into a doubly degenerate mode and a nondegenerate mode. The new bands seen in CdTe:P+In at 305 and 331.5 cm^{-1} can be accounted for on this basis; thus $[(2 \times (331.5)^2 + 305^2)/3]^{1/2} \simeq 322.9$ cm^{-1}, which is close to the 322 cm^{-1} mode. However, no simple interpretation such as this can account for all the bands seen in the other three systems mentioned above. It may be noted that in CdTe:P+Cu the bands at 269 and 308 cm^{-1} completely disappeared while the 322 cm^{-1} band is present and is the weakest of all the bands seen. In this case all the phosphorus appears to be present in complexes with the copper, while in CdTe:P+Al there do not appear to be any complexes between Al and P. However, the $Al_{Cd}(T_d)$ mode originally seen at 299 cm^{-1} in CdTe:Al$^{(1)}$ appears to move up to 302 cm^{-1}. This may be due to lattice distortion with the heavy [P] doping levels.

In summary, with the experimental data collected so far, it is not yet clear what defects account for the bands 269, 308 and 322 cm^{-1} in the CdTe:P system. The 322 cm^{-1} band appears to be different from the rest in behavior in that we observe it in all concentration levels and also in all double doped systems. Of the other two bands, the 269 cm^{-1} appears to be present as we lower the doping level, while the 308 band almost disappears at 10^{16} cm^{-3}. In the CdTe:P+Cu system, the 269 and 308 bands both disappear, while only the 322 cm^{-1} band is present. From this information we tentatively assign the 322 cm^{-1} to P_{Te}, and no possible assignments can be made for the other bands, although phosphorus appears to be an amphoteric impurity in CdTe.

We are planning to extend these measurements with annealing treatments in Cd and Te rich atmospheres with a view to understanding the behavior of P in CdTe. This would also lead to a study of p-type CdTe and a determination of the free carrier absorption cross section for holes. We have completed growth of two ingots with 10^{19}/cc As and 10^{19}/cc Sb to study the behavior of p-type CdTe. These impurities are sufficiently heavy that we do not anticipate any localized vibrational modes, but annealing treatments with transport and optical measurements, to be done in cooperation with Prof. Kröger, may throw light on the nature of the defects involved and their influence on the optical absorption.

3. ZnSe:Al

In continuation of our previous work, we carried out further anneals of ZnSe:Al in varying zinc activities with the crystal temperature fixed at 885°C. A series of ZnSe:Al ingots with different Al doping levels are subjected to these anneals in a two zone furnace. The annealing time was 6 hours, and the crystals were then quenched to room temperature. Hall effect measurements revealed that all these samples are n-type. Optical absorption measurements indicated a behavior of $\alpha \sim \nu^{-3}$ as shown in Fig. 8. These results are being analyzed within the framework of the presently available theoretical models.$^{(2)}$ *Prima facie* it appears that the free carrier absorption is dominantly via a polar optical mode scattering mechanism rather than by ionized impurity scattering as we inferred in the previous final report for the period 1 June 1972 - 31 August 1974 (report no. AFCRL-TR-74-0557).

We are comparing the theory and our experimental results, and our findings will be reported in our next report.

References

1. B. V. Dutt, M. Al-Delaimi and W. G. Spitzer, accepted for publication in Jour. Appl. Phys.
2. B. Jensen, J. Phys. and Chem. of Solids 34, 2235 (1973).
3. A. Mitsuishi, A. Manabe, H. Yoshinaga, S. Ibuki and H. Komiya, Prog. Theor. Phys. 45 (Supplement), 21 (1970).
4. B. V. Dutt and W. G. Spitzer, accepted for publication in Jour. Appl. Phys.

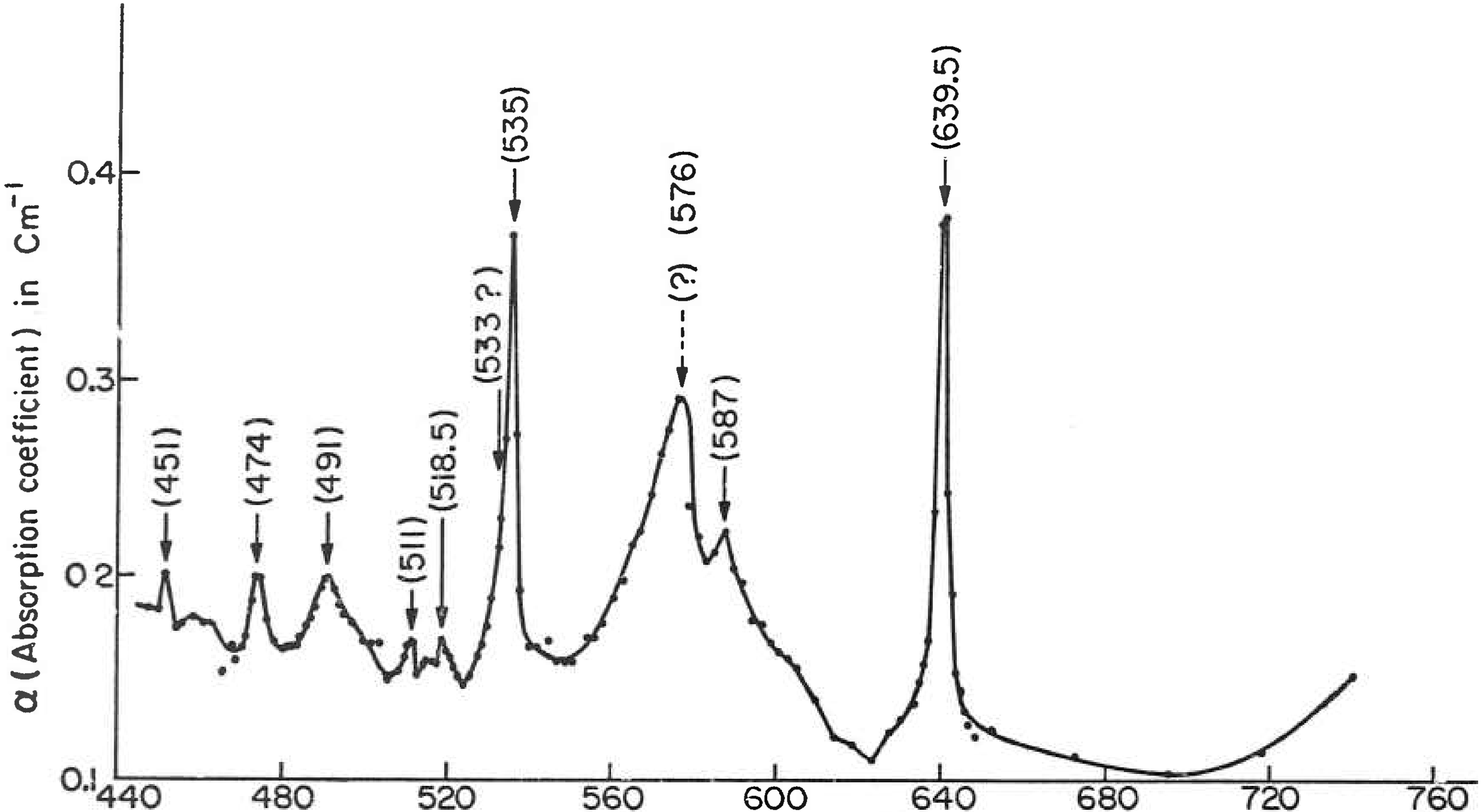

FIG. 1 - 80°K Absorption spectrum of CdTe: P in the second harmonic region. [P] ≃ 5×10^{19} cm^{-3}

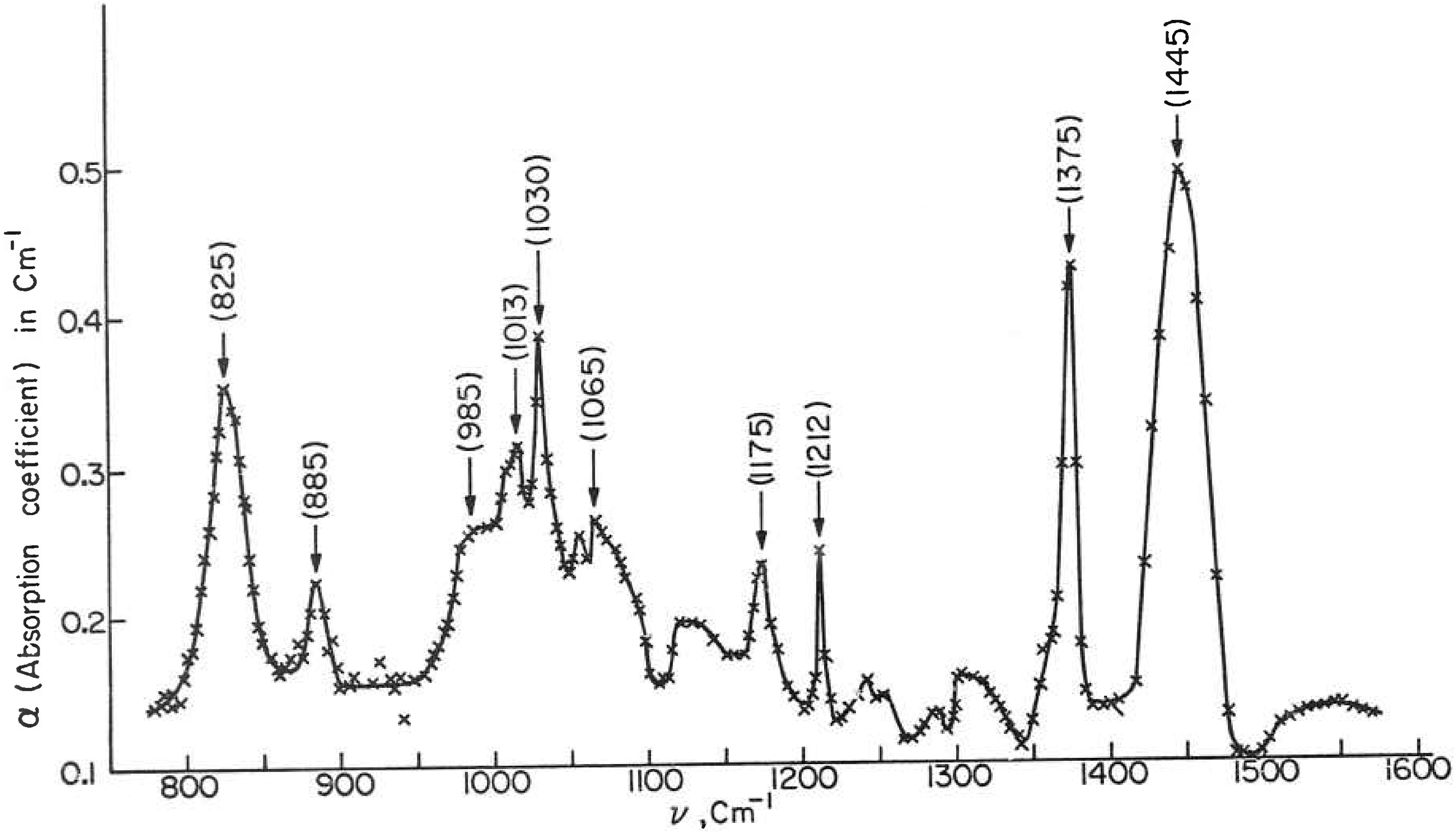

FIG. 2 – 80°K Absorption spectrum of CdTe: P in the third harmonic region.

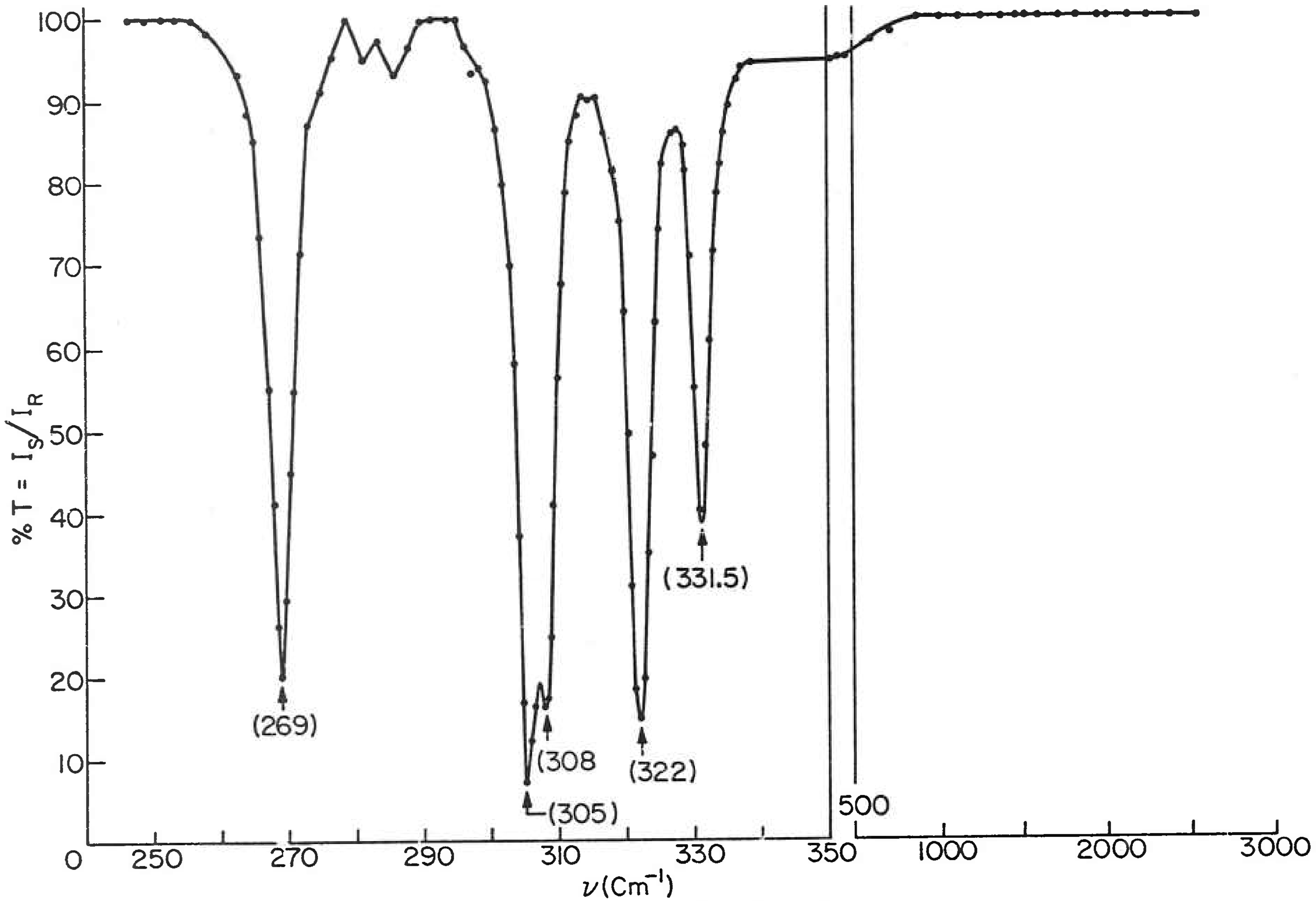

FIG. 3 – 80°K Transmission of CdTe: In + P, t = 0.029 cm

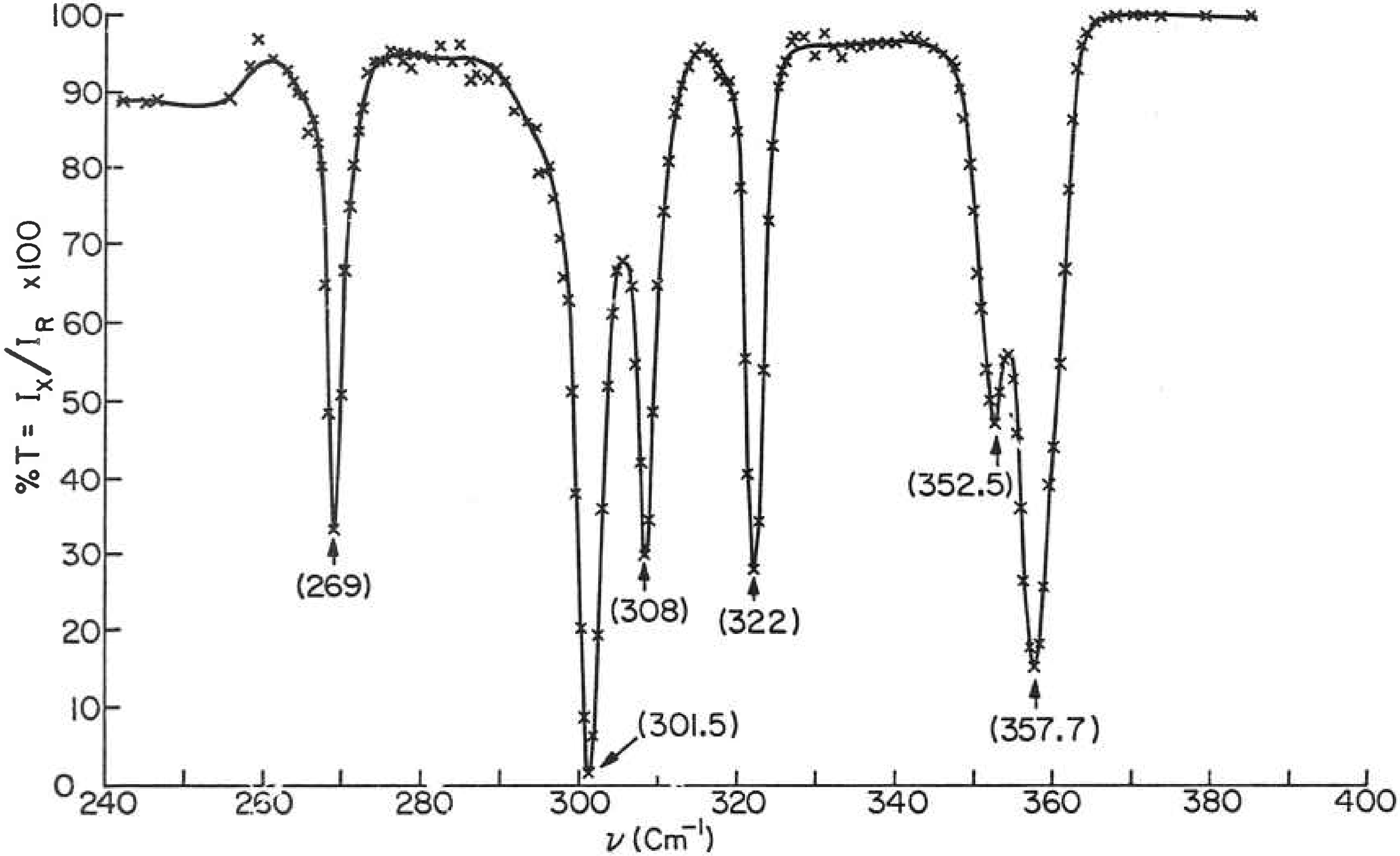

FIG. 4 - 80°K Transmission of CdTe:
Ga + P, t = 0.055 cm

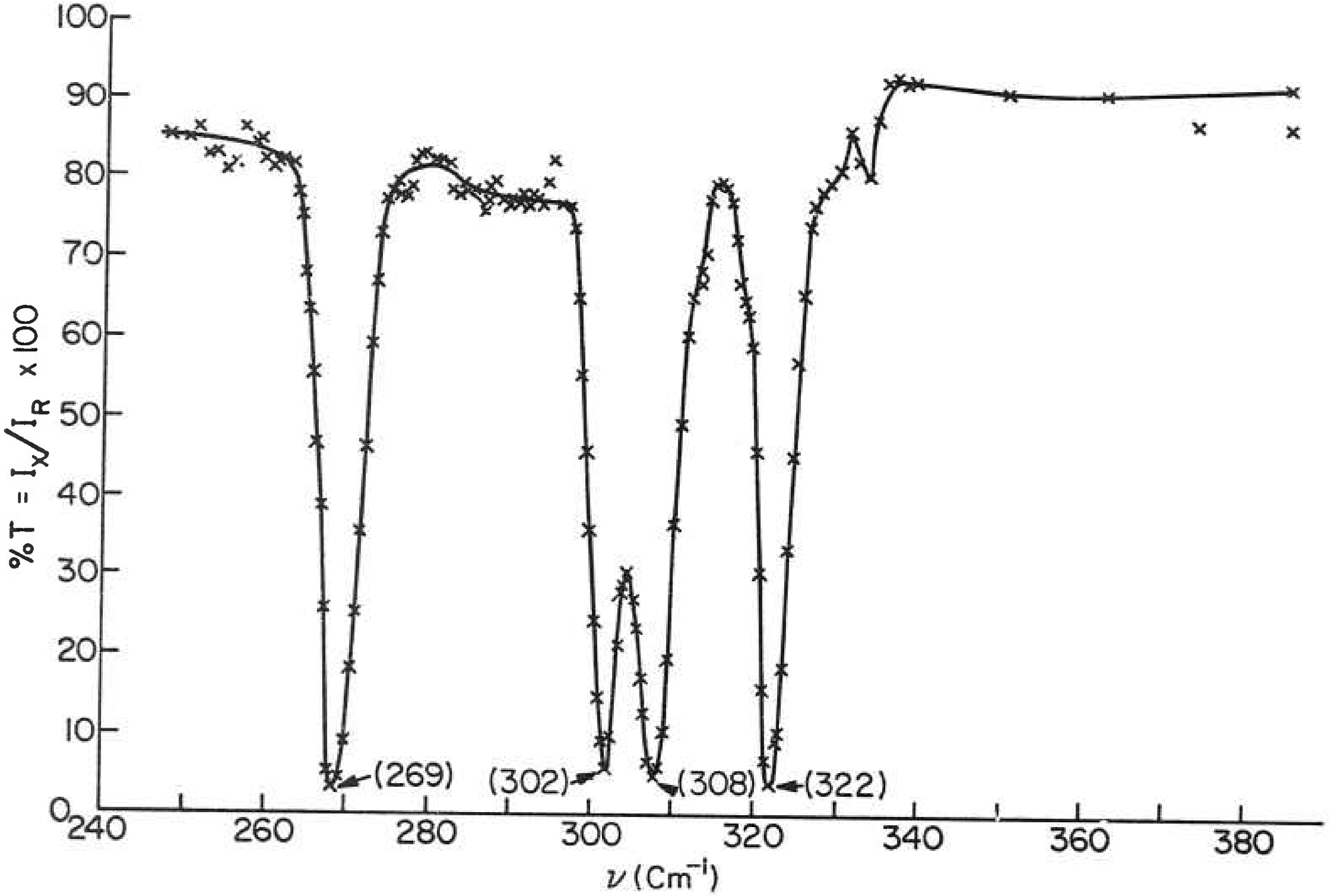

FIG. 5 - 80°K Transmission of CdTe:
Al + P, t = 0.055 cm

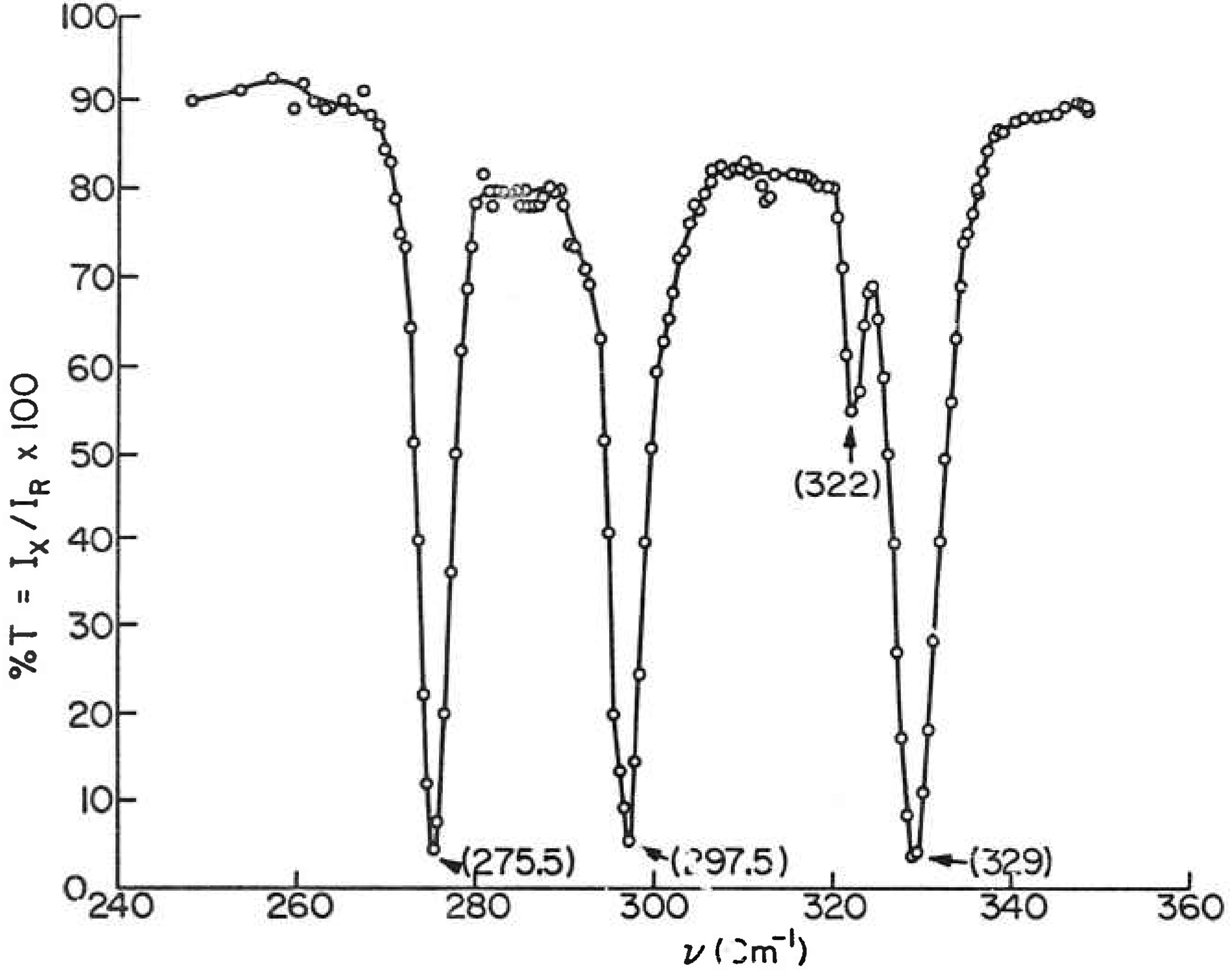

FIG.6 - 80°K Transmission of CdTe:
Cu + P, t = 0.055 cm

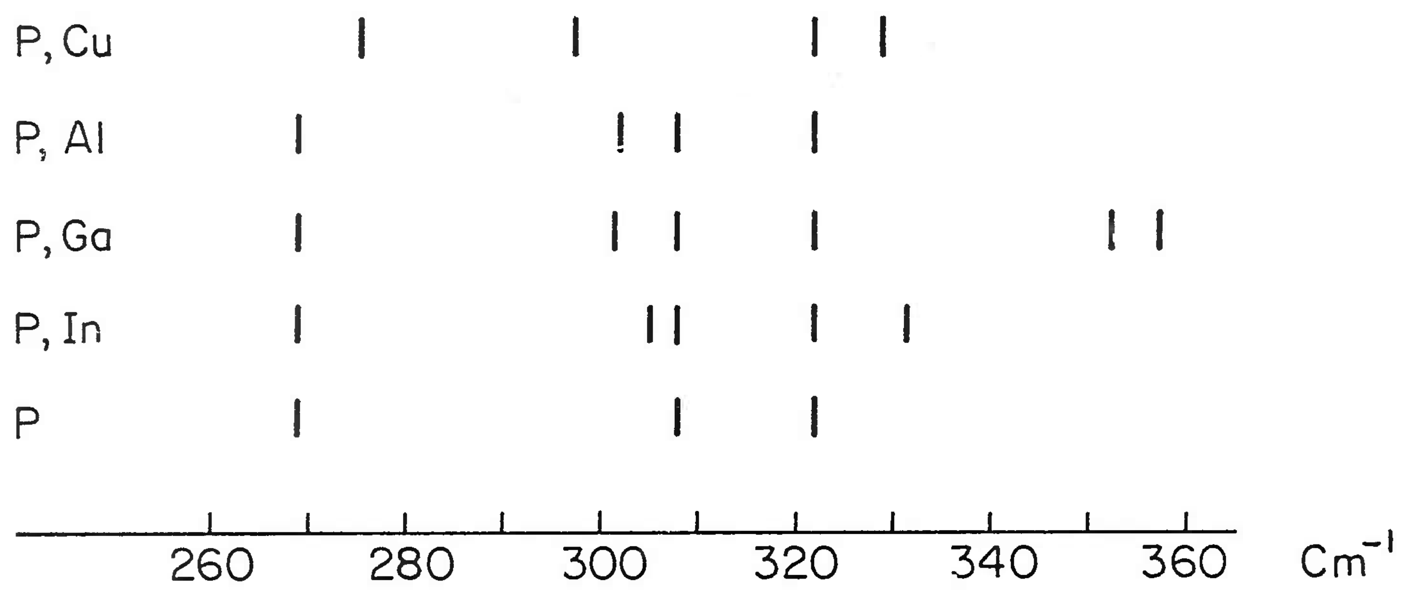

FIG. 7 – SCHEMATIC REPRESENTATION OF P-RELATED LVM IN CdTe at 80°K

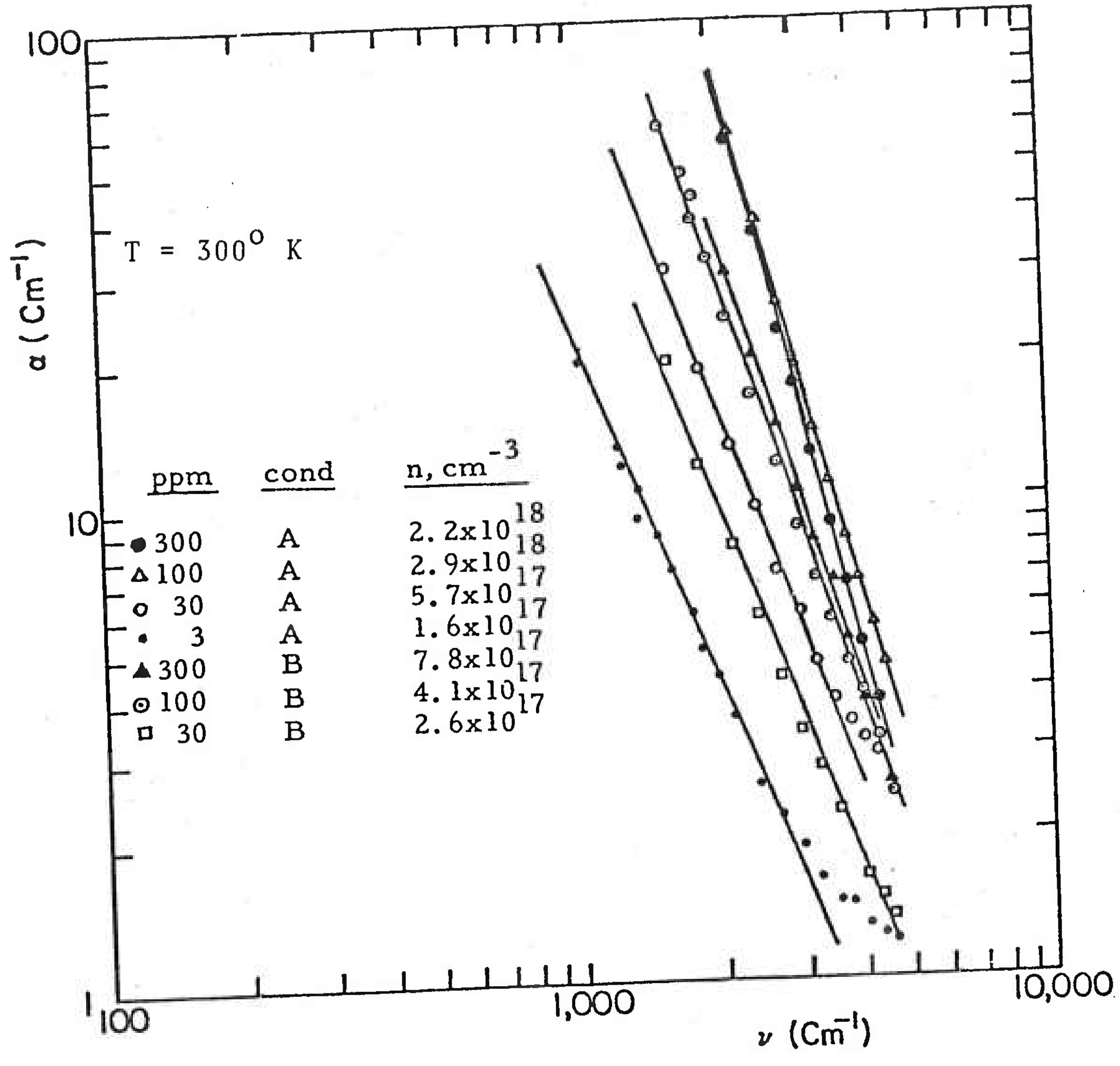

FIG.8 – Absorption of annealed ZnSe: Al with different Al concentrations. The anneals are described in the text.

Study of Defects in II-VI Compounds

F.A. Kröger, F.A. Selim, and A. Ray

CdTe + P

As mentioned in our previous report, CdTe doped with phosphorus shows p-type conductivity under all circumstances, but the number of holes per atom is largest at low P contents and for annealing under medium cadmium pressures. The lowest hole concentrations (i.e. highest resistance values) are found after annealing at high or low p_{Cd}. At the highest resistances, the absorption at 10.6 μm is still in the range 10^{-1}-$10 cm^{-1}$. The properties can be accounted for on the basis of a detailed defect model, in which P appears as the species P_i', $(P_{Cd}P_i)^x$ and $(P_{Cd}2P_i)^x$. Fig. 2 shows for T = 700°C at which P concentration and p_{Cd} the various species are dominant and which species dominate the neutrality condition. It is possible that a second acceptor species P_{Te} occurs at high p_{Cd}, but our data can be accounted for without this species (but not without P_i).

Temperature dependence of the Hall effect gives for the position of P_i' acceptor level at $[P] \approx [h] = 6.\ 10^{16} cm^{-3}$, $E_{P_i'} - E_v = 0.034$ eV.

CdTe + Cr or Ge

In our previous report it was stated that crystals of CdTe heavily doped with Cr or Ge had a high resistance but nevertheless showed a high absorption for 10.6 μm. In the present period, B.V. Dutt grew crystals doped respectively with 4×10^{17}Cr cm^{-} and 1×10^{17}Ge cm^{-3}. Both are p-type. Figures 3 and 4 show the hole concentrations and the absorption coefficients for 10.6 μm radiation for the two types of crystals after annealing at 700°C under various cadmium pressures. For the Cr doped crystal the absorption is proportional to the hole concentration; it is lowest, with $\alpha_{10.6} = 2\mathrm{cm}^{-1}$ at $c_h = 2.5 \times 10^{12}\mathrm{cm}^{-3}$. This absorption is much higher than found for indium doped CdTe, where $\alpha_{10.6} = 3 \times 10^{-2}\mathrm{cm}^{-1}$ at $c_h = 10^{14}\mathrm{cm}^{-3}$. The absorption is probably due to a species the concentration of which is proportional to the concentration of free holes.

The Ge doped crystal (Fig. 4) the absorption coefficient at 10.6 µm is proportional to the hole concentration only for samples annealed at $p_{Cd} > 10^{-2}$atm. For annealing at lower p_{Cd} the absorption becomes independent of p_{Cd} with $\alpha = 5 \times 10^{-3}\mathrm{cm}^{-1}$ while the hole concentration keeps decreasing with decreasing p_{Cd}. The reason for this leveling off of α is still unknown. A survey of the absorption coefficients observed with thin samples of CdTe, doped with the various dopants is given in Fig. 5. It is seen that the lowest absorption obtained so far is for CdTe doped with In ($\approx 1.2 \times 10^{17}$In cm^{-3}). It appears, however, that if the levelling off in the Ge-doped crystal could be avoided, an absorption lower than that found in the In-doped crystal could be reached.

ZnSe + Al

High-temperature Hall effect measurements of ZnSe single crystals doped with 300 ppm have been started. At 900°C the electron concentration $c_e \propto p_{Zn}^{\frac{1}{2}}$ with absolute concentrations that are ≈100 higher than those observed by Smith for undoped ZnSe. This indicates that the native atomic disorder at 900°C is $\approx 10^4$x smaller than the Al content of the present crystal.

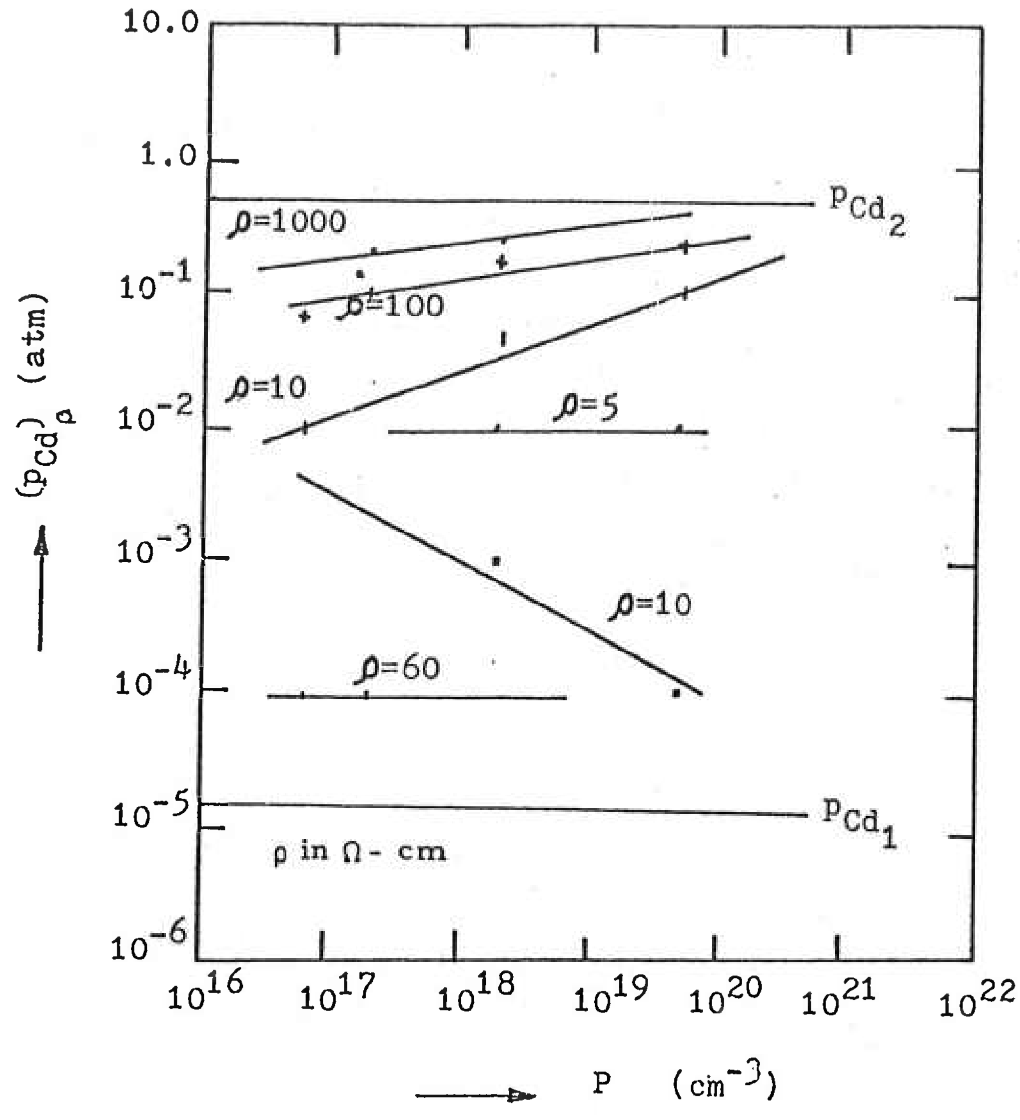

Fig. 1. Isotherms of high and low resistivity P-doped crystals quenched from 700 °C. p_{Cd_1} and p_{Cd_2} are the lower and upper cadmium pressure phase boundaries of CdTe at 700 °C.

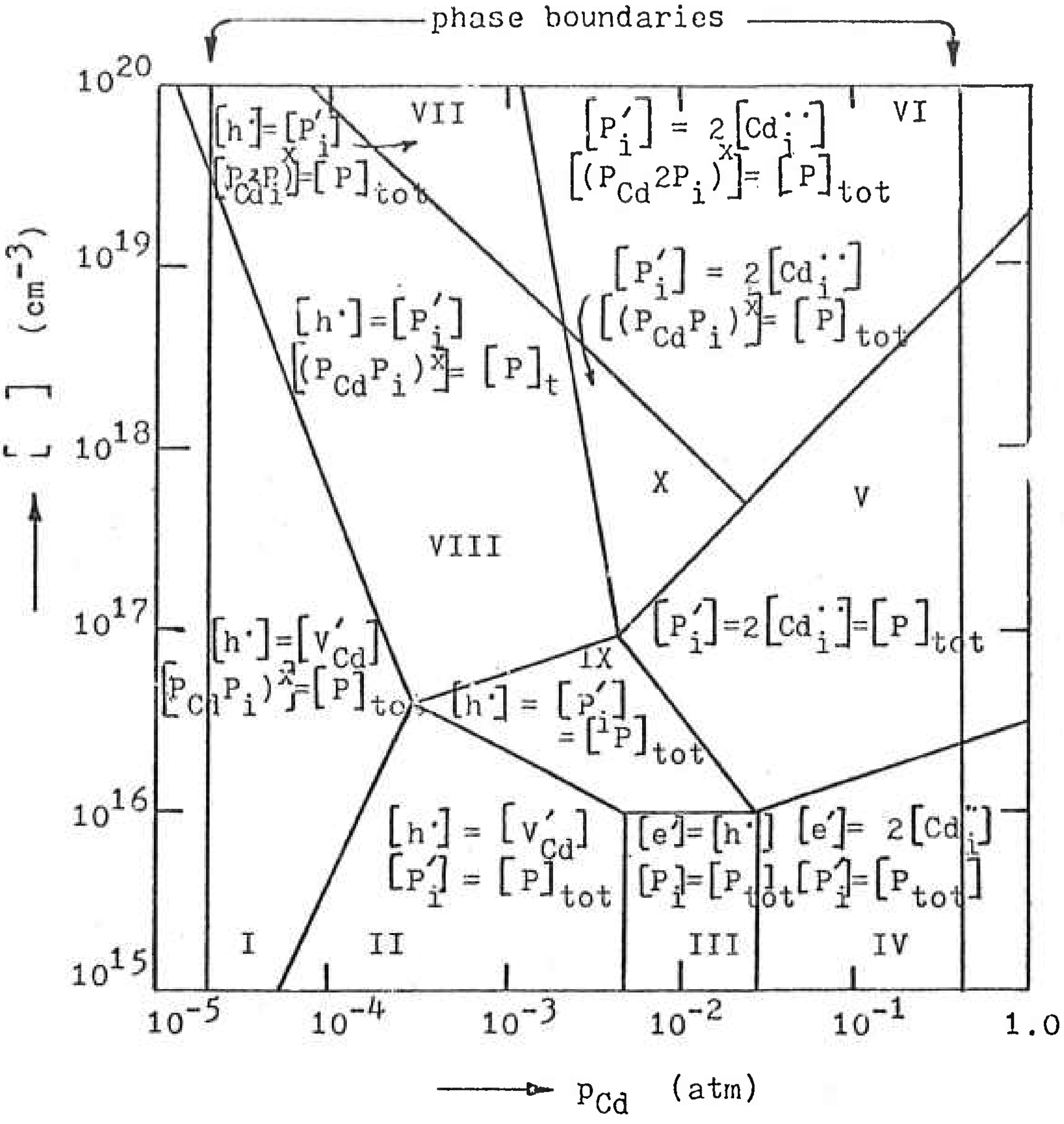

Fig. 2. Range boundary diagram showing the defect structure of P doped CdTe at 700 °C.

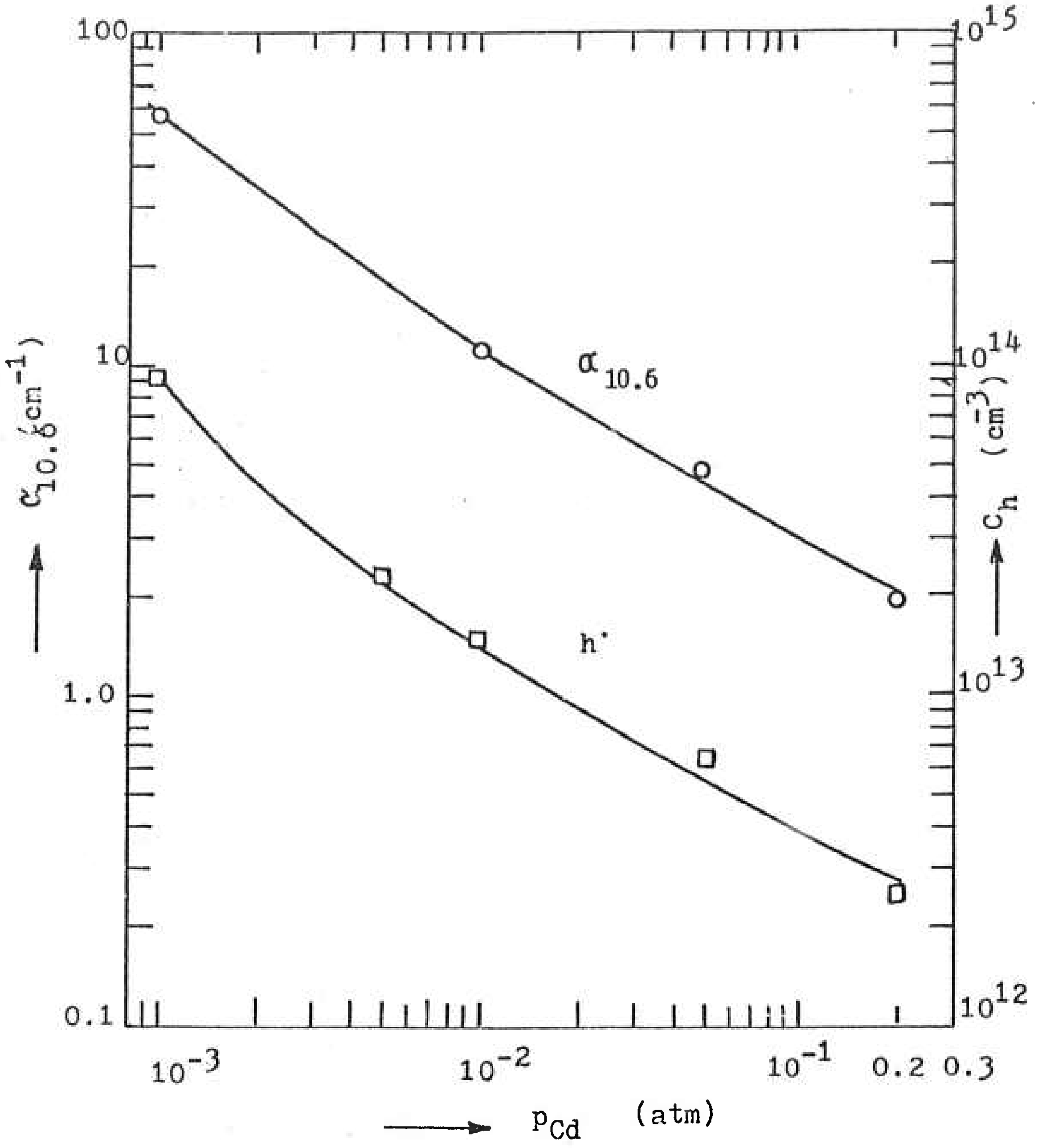

Fig. 5. Absorption coefficient and hole concentrations for CdTe + $4x10^{17}$Cr cm^{-3}, cooled after annealing at various p_{Cd} at 700°C.

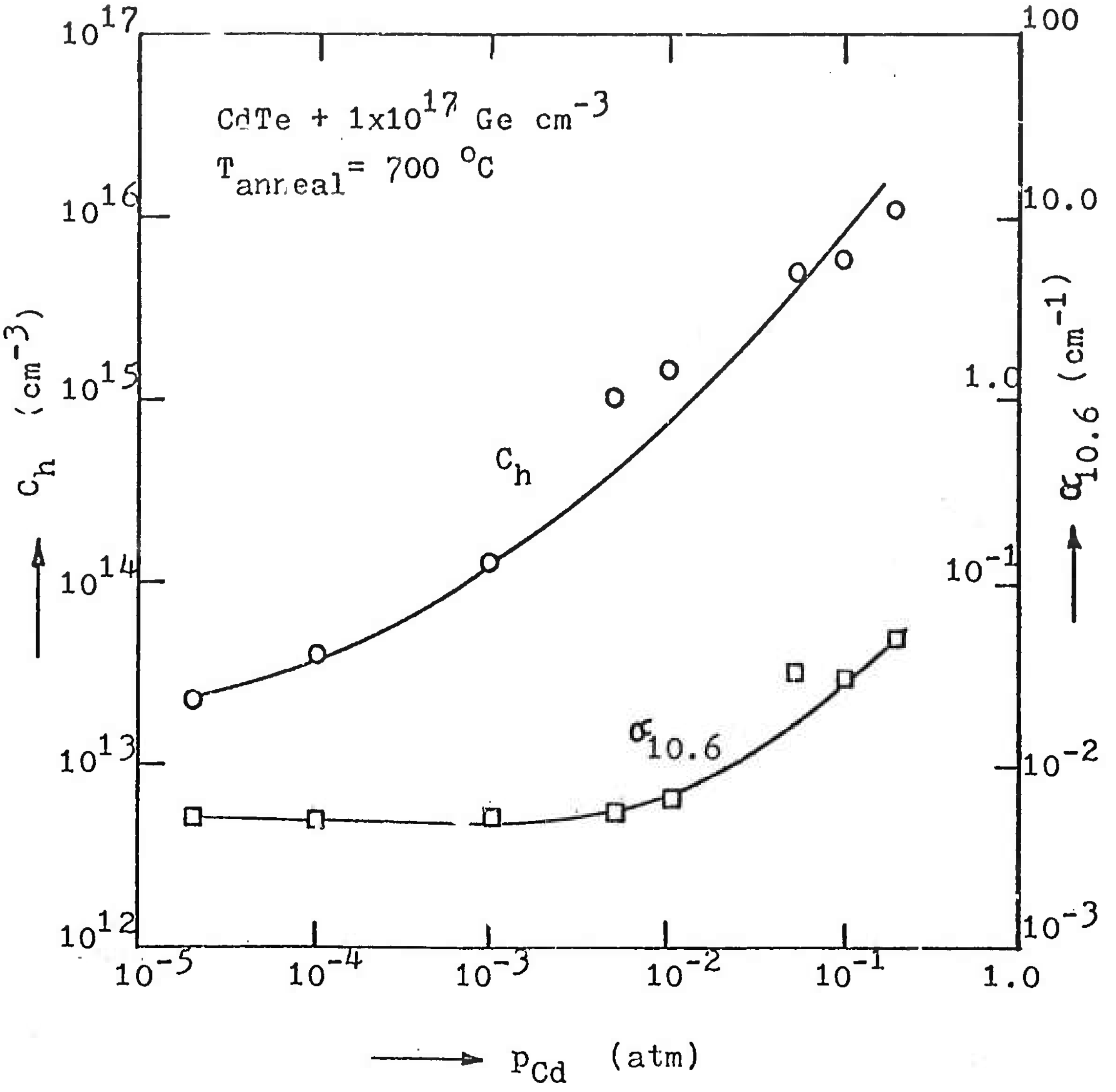

Fig. 4. Hole concentrations and absorption coefficient at 10.6 μm for CdTe + $1x10^{17}$ Ge cm^{-3} for crystals cooled after annealing at 700 °C.

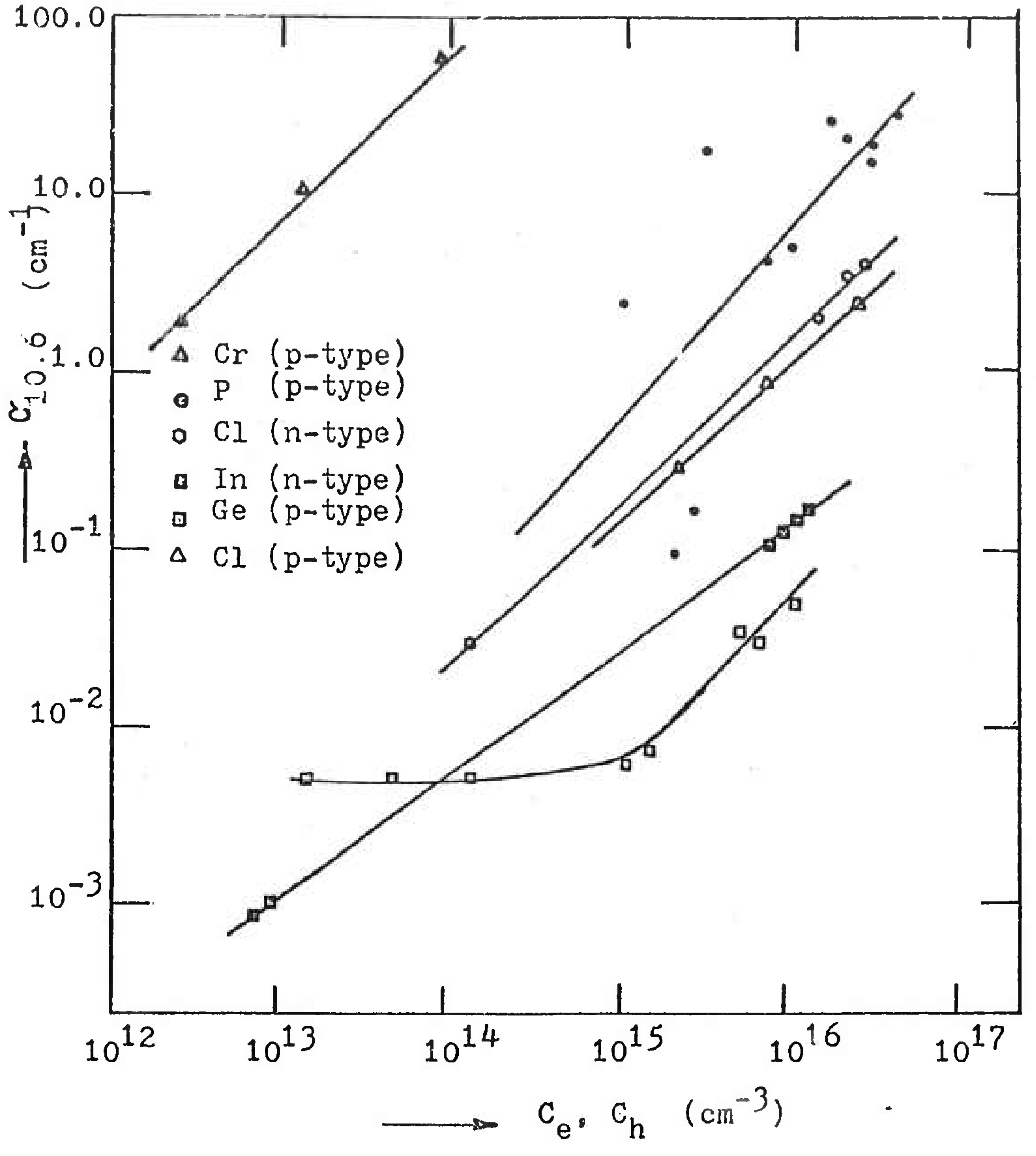

Fig. 5. Absorption coefficient at 10.6 μm for CdTe doped with various dopants as a function of carrier concentrations (electrons or holes).

Optimization of Alkali Halide Window Materials

P. J. Shlichta, J. F. Yee and E. A. Miller

Objectives and Status: Under the present program, we have endeavored to resolve the discrepancy between the theoretically predicted (10^{-7} cm^{-1}) and experimentally observed (10^{-3} cm^{-1}) 10.6 micron absorptivity of potassium bromide. During previous report periods, it was tentatively concluded that the excess absorptivity was due to traces of an oxidized anion impurity, such as bromate, which was not entirely removed by HBr treatment. Treatments with organic bromides, such as CBr_4, C_2H_5Br, and CF_3Br, were unsuccessful since these reagents decomposed at temperatures well below the melting point of KBr. Treatments with strong reducing agents such as C_2F_4 or $C_2C\ell_4$ were unsuccessful because of carbon formation and/or reaction with the KBr to form $KC\ell$. Treatment with potassium vapor caused excess absorptivity, due to color centers, and tended to destroy the crucibles used.

We therefore decided to reassess the feasibility of purification by reactive vapor treatment and to try other purification techniques such as zone melting or crystallization from solution. However, due to contract changes, this portion of the program was terminated in August 1975, i.e. six months ahead of the originally scheduled date. Therefore, our evaluation of thes purification techniques is incomplete as of the present final report. It is hoped, however, that the samples prepared during this contract period will be evaluated by other investigators and that some of the most promising techniques, such as zone melting, will be given further study.

Preliminary Purification: The starting material for all of our investigations was moist crystals of KBr purified by ion exchange and fractional crystallization. The output-limiting step in this pre-purification procedure was the evaporation of the ion-exchange-purified solution. Aspirators provided an inadequate vacuum and mechanical pumps, aside from providing a potential source of contamination, were incapable of withstanding the passage of large quantities of water vapor. This problem was solved by the purchase of a Kinney liquid-ring vacuum pump (Model KLRC-25) which uses tap water as its pump fluid. By using this pump in conjunction with a vacuum oven (on loan from the Jet Propulsion Laboratory), we were able to process five gallons of purified KBr solution per day. At present, we have over ten kg of purified KBr on hand.

Vacuum drying of the moist crystals was also an output-limiting step since the crystals often contained numerous fluid inclusions. An apparatus for removing these inclusions, by migration in a thermal gradient, was designed but early termination of the program prevented its construction or testing.

Vapor Treatment: Before discarding treatment with halide vapor as ineffective, we decided to check against any possible shortcomings in our experimental procedure. These are summarized in Table 1.

Our regular procedure was to (a) melt KBr in a carbon or silica crucible contained in a silica crystal pulling chamber, (b) introduce a silica tube into the melt and bubble reactive gas through it, and (c) exchange the silica tube for a pull rod and pull a crystal in a static helium atmosphere under reduced pressure. It was considered possible that step (b) might provide insufficient contact between the reactive gas and the melt. Moveover, step (c) might permit recontamination of the melt, e.g. by leaks in the system. Accordingly, an entirely different procedure was tried. The KBr was placed in a vertical silica tube containing a porous silica frit (Figure 1a) and heated to the melting point of KBr while reactive gas was passed upward through the tube. When the KBr melted, the reactive gas was allowed to bubble through the melt for an additional 24 to 72 hours, after which it could either be crystallized *in situ* or passed through the frit (by reversing the gas pressure) into a lower receiving chamber (e.g. Figure 1b). This procedure has been used for many years by the Anderson Physical Laboratory for the successful removal of hydroxide from NaCℓ and KCℓ.

Experiments using HBr, CF_3Br, and $CC\ell_4$ gave the same results, with regard to bromine and/or carbon formation, which had been observed earlier in our crystal pulling apparatus (Table 2). As a check against possible contamination by our apparatus or reagents, a similar experiment, using HBr for vapor treatment, was undertaken by the Anderson Physical Laboratories, using our fractionally crystallized KBr as starting material. This experiment provided us with four sealed silica tubes each containing approximately 100 g of HBr-treated KBr.

Crystal Growth: Attempts to grow crystals from our HBr- and CF_3Br- purified KBr by *in situ* unidirectional solidification resulted in highly cracked or polycrystalline masses. A modified apparatus, permitting sequential vapor treatment, zone melting, and Bridgeman crystal growth without changing containers, was designed (Figures 1b, c and d) but time did not permit construction or testing.

Because of its contamination by carbon deposition, no attempt was made to grow a crystal from the $CC\ell_4$-treated KBr.*

---

* This was a mistake. P. Klein of NRL recently treated KBr with $CC\ell_4$- saturated argon in a similar manner and also observed carbon formation and bromine evolution at 600°C. He, however, continued to heat the KBr, under flowing argon, up to the melting point and then grew a crystal by the Bridgeman technique. Apparently, the carbon particles either floated to the surface or were rejected by the growing crystal interface. The resultant crystal had a 10.6 micron bulk absorptivity of 6×10^{-6} cm^{-1} -- by far the lowest value reported to date.

One of the sealed tubes of HBr-treated KBr was used to grow a crystal by the Bridgeman method. A faint brown discoloration was observed in the upper part of the crystal (Figure 2a) and small brown stains were found on the top of the crystal. Another tube, after being subjected to four horizontal zone-melting passes, showed a strong brown coloration at the terminal end (Figure 1b). Pending analysis, this colored impurity is presumed to be free bromine or a bromine-bromide complex analogous to the triodide ion. These results are consistent with observations, during several recent attempts at crystal pulling, of a slight darkening of KBr melts after prolonged HBr treatment. If analyses confirm that this impurity is indeed free bromine, then its presence can be interpreted in any of several ways, as indicated in column 1 of Table 2. It could mean that, as per equation (1b), the HBr is actually removing bromate ion. It could also mean, as per equation (1d), that the HBr is reacting with atmospheric oxygen trapped in or leaking into the system. Alternatively, as per equation (1e), the thermal decomposition of HBr into hydrogen and bromine, although less than 0.1% at these temperatures, could be sufficient to leave some bromine dissolved in the molten KBr. It is hoped that absorption spectra and laser calorimetry will be undertaken in the near future so as to determine whether this impurity is really a cause of excess 10.6 micron absorptivity.

Crystal Growth from Vapor: During the Bridgeman-method crystallization, it was noted that transparent KBr mesas up to 4 mm in diameter grew on the walls of the silica tube (Figure 3a). These mesas appear under microscopic examination (Figure 3b) to be single crystals with well defined growth steps and are therefore presumed to have grown by sublimation. Westphal and Rosenberger (Ref. 1) have recently reported the growth of large (1 cm) $KC\ell$ and KBr crystals by sublimation. The present observation confirms the hypothesis that sublimation may be an excellent approach to the growth of ultrapure

KBr crystals for research.

Crystal Growth from Solution: Attempts were also made to grow KBr crystals from solution by the slow cooling of purified KBr solution either in the presence of cleaved plated of melt-grown material or by spontaneous nucleation. This method has in the past yielded NaCℓ and KCℓ crystals of extremely high purity and perfection (Ref. 2). For the present experiments, temperature control was achieved by irradiating the solution with two SCR-controlled thermistor-regulated infrared heat lamps; no stirring was used. The spontaneously nucleated crystals were in all cases quasi-dendritic and filled with fluid inclusions (Figure 4a). In only one case, using extremely slow temperature reduction so that the rate of crystallization was less than about 0.2 mm per day, was a clear overgrowth (~ 1 mm) on a cleaved seed effected. This approach does not appear to be competitive with growth from melt or vapor.

Controlled Contour Solution Polishing*: It has been shown (Ref. 3) that the mechanical polishing of KCℓ crystals increases the 10.6 micron surface absorptivity and that subsequent chemical polishing in diluted hydrochloric acid or ethanol tends to remove this excess surface absorption, albeit with some rounding of the edges and/or surface. It therefore seemed desirable to develop a technique for chemically polishing KBr crystal surfaces while maintaining the flatness (or curvature) of the cleaved or mechanically polished surface. This might be done, for example, by slowly feeding the crystal onto a moving film of solution, formed by dripping solution onto a rotating wheel.

The apparatus, as ultimately developed, is shown in Figure 5. The solution flows from a reservoir (A) onto a glass plate (B) mounted

---

* This portion of the program was undertaken by E. A. Miller.

on a rotating wheel (C). A metering valve (D) regulates the flow of solution while a selector stopcock (E) permits change of solution without interruption of flow. (This can be used either to change to an inert liquid (F), so as to wipe off the polishing solution from a finished surface, or, at the beginning of the process, to change to pure water, so as to rapidly "rough down" the crystal to the desired size and shape.)

In order to maintain a smooth and vibration-free crystal feed, a hydraulic system was used. The crystal (G) is mounted onto the plunger of a 50 cc hypodermic syringe (H) which acts as a hydraulic piston, whose motion is controlled by a 2 cc hypodermic syringe (I) acting as a drive piston. The motion of the drive piston is in turn controlled by a micrometer (J) driven by a variable speed motor. By means of a selector stopcock (L), the feed piston can be connected either to the drive piston (1) or to a fluid reservoir (M). The latter is used either for positioning the crystal or for operating the system with the crystal pressed against the wheel at constant pressure. An auxiliary motor and pully (N) permit the crystal to be rotated during polishing.

All investigations were carried out on 20 x 20 x 7 mm cleaved plates from Optovac Corp. Before polishing, the plates were mechanically polished with linde B abrasive in an isopropyl alcohol slurry and then annealed for 16 hours at 600°C in argon. (The mechanical polishing is not necessary for this process; it was used here to produce a high density of scratches and dislocations on the surface of the samples.) Potential polishing solutions were evaluated by immersing crystals in them, with continuous agitation, for periods ranging from 1 to 32 minutes. The results, as shown in Table 3, indicate that concentrated hydrobromic acid is by far the best polishing agent with 85% ethanol a poor second. Because it was feared that the acid fumes might damage the polishing apparatus, 85% ethanol was used in all the experiments reported herein. The advantages of annealing the specimens before polishing, as reported in reference 3 for $KC\ell$, was confirmed in the case of KBr as shown in Figure 6.

The first series of polishing experiments was carried out with a Politex poromeric velvet polishing pad on top of the glass plate. It was believed that this would produce a smoother and more uniform liquid layer. In these experiments, the crystal was placed in light contact with the dry felt before the beginning of polishing. As shown in Table 4, however, the rate of surface removal was considerably higher than could be accounted for by the crystal feed rate. It was therefore assumed that the solution between the velvet hairs is essentially stagnant and that solution flows on top of this layer.

Therefore, polishing was attempted using a bare glass plate. It was first necessary to determine the ranges of wheel rotation and solution flow in which a continuous flat film of centrifugally flowing solution could be maintained. As might be expected, it was found that, for a given rotation rate, there existed a threshold solution flow below which the film was discontinuous or rippled and above which it was smooth. In the expectation that a thin film would provide the best control of surface flatness, the solution flow rate was set just above the threshold value. As shown in Table 4 and Figure 7, these conditions produced the smoothest and flattest surfaces thus far obtained. These surfaces are more than adequate for our laser calorimetry and acoustic surface absorption. With further optimization, as for example the substitution of concentrated hydrobromic acid for 85% ethanol, surfaces of window or lens quality might well be achieved.

Final Recommendations: This project is now terminated, but in the expectation that KBr will eventually merit further study by other investigators the following tentative conclusions and recommendations are made:

(1) It appears likely that 10.6 micron absorptivities of less than 10^{-6} cm^{-1} can be achieved with KBr.

(2) The best approach appears to be sequential reactive vapor treatment, zone melting, and Bridgeman crystal growth in a sealed tube without transfer between operations, as per Figure 1b, c, and d.

(3) The most promising reactive halides are HBr and $C_2C\ell_4$, perhaps used sequentially.

(4) Zone melting is particularly important, since it appears to remove dissolved bromine and would presumably remove carbon particles and impurity anions such as bromate.

(5) The controlled-contour chemical polishing technique, used first with water to rough-shape as-grown crystals and then with concentrated hydrobromic acid to produce flat surfaces, should produce samples having the lowest bulk and surface absorptivities.

References

1. G. H. Westphal and F. Rosenberger, "Vapor Growth of Alkali Halides," American Association for Crystal Growth; Third American Conference on Crystal Growth, Stanford University, July 13-17, 1975, p. 46 of abstract book.
2. P. Gruzensky, "Growth of Large Sodium Chloride Crystals from Solution for Color Center Studies," J. Chem. Phys. 43 (1965) pp. 3807-3810.
3. J. W. Davisson, "Chemical Polishing of NaCℓ and KCℓ Laser Windows," in Conference on High Power Infrared Laser Window Materials, October 30, 31, and November 1, 1972, Vol. II, C. Pitha, ed. (AFCRLTR-73-0372 (11), 19 June 1973) pp. 525-534.

Table 1. Analysis of Possible Shortcomings of Halide-Vapor Treatment of KBr

Possible Source of Impurities	Attempted Remedy	Status at End of Project
Insufficient exposure of molten KBr to reactants	Use of vertical fritted reaction tubes (Figure 1a)	Performed with HBr, CF_3Br and $CC\ell_4$; effect on KBr absorptivity not tested
Leak in system causing reexposure to H_2O or O_2 after treatment	HBr treatment by outside vendor with in situ sealing in silica tubes for subsequent Bridgeman growth	Performed, but colored impurity [Br_2?] observed after crystallization (Figure 2a)
	Use of vertical fritted tubes for halide treatment with subsequent in situ zone melting and crystal growth (Figure 1 b-d)	Not tried
Reactants or reaction products remaining in KBr after treatment	Vacuum distillation after treatment	Not tried
	Zone melting after treatment (Figure 1c)	Performed; colored impurity [Br_2?] observed (Figure 2b)
Reactants not strong enough to remove impurities	Reconsideration of $CC\ell_4$	Carbon deposited in KBr at 600°C (see Table 2)
	Reconsideration of K vapor with with subsequent HBr treatment	Not tried because of unavailability of non-reactive container
	Zone melting in lieu of treatment	Performed; see above
	Growth of crystals from solution	Unsuccessful; opaque crystals (Figure 4)
	Growth of crystals from vapor	Accidental results (Figure 3) suggest feasibility

Table 2. Effect of Treatment of KBr with Volatile Halides

Reagent	Supposed Reaction with: (a) Hydroxide, (b) Bromate	Observation	Possible Explanation
(1) HBr	(a) $HBr + OH^- = H_2O + Br^-$	Darkening of molten KBr	(c) Validity of reaction (1b) and/or formation of complex or color centers
	(b) $6HBr + BrO_3^- = 3H_2O + 3Br_2 + Br^-$	Brown volatile deposit after zone melting (q. v.)	(d) $4HBr + O_2 = 2H_2O + 2Br_2$ (e) $2HBr = H_2 + Br_2$ (< 0.1% at 800°C)
(2) C_2H_5Br	(a) $C_2H_5Br + OH^- = C_2H_5OH + Br^-$ (b) $3C_2H_5Br + 4(BrO_3)^- = 6H_2O + 6CO + 3HBr + 4Br^-$	Carbon deposit (> 700°C)	(c) $C_2H_5Br = HBr + CH_4 + \underline{\underline{C}}$
(3) CBr_4	(a) $CBr_4 + 2OH^- = CO_2 + 2HBr + 2Br^-$ (b) $3CBr_4 + BrO_3^- = 3COBr_2 + 3Br_2 + Br^-$ (?)	Carbon deposit and bromine evolution (> 600°C)	(c) $CBr_4 = \underline{\underline{C}} + 2Br_2$
(4) CF_3Br	(a) $CF_3Br + OH^- = CF_2O + HF + Br^-$ (b) $CF_3Br + BrO_3^- =$ N. R. (?)	Bromine evolution (> 700°C)	(c) $2CF_3Br = C_2F_6 + Br_2$
(5) $C\ell_4$	(a) $CC\ell_4 + 2OH^- = CO_2 + HC\ell + 2C\ell^-$ (b) $6CC\ell_4 + 2(BrO_3)^- = 6COC\ell_2 + 5C\ell_2 + Br_2 + 2C\ell^-$	Bromine evolution (> 600°C) Carbon deposit (> 600°C)	(c) $CC\ell_4 + KBr = CC\ell_3Br + KC\ell$ (d) $CC\ell_4 + 4KBr = 4KC\ell + 2Br_2 + \underline{\underline{C}}$
(6) $C_2C\ell_4$	(a) $C_2C\ell_4 + 2OH^- = 2CO + 2HC\ell + 2C\ell^-$ (b) $3C_2C\ell_4 + 2(BrO_3)^- = 6COC\ell_2 + 2Br^-$	Voids in KBr crystals (> 700°C) Carbon deposit (> 750°C)	(c) $C_2C\ell_4 + KBr = C_2C\ell_3Br + KC\ell$ (d) $C_2C\ell_4 = CC\ell_4 + \underline{\underline{C}}$
(7) C_2F_4	(a) $C_2F_4 + 2OH^- = 2CO + 2HF + 2F^-$ (b) $3C_2F_4 + 2(BrO_3)^- = 6COF_2 + 2Br^-$	Carbon deposit (>680°C) White waxy deposit (>680°C)	(c) $C_2F_4 = CF_4 + \underline{\underline{C}}$ (d) $nC_2F_4 = (C_2F_4)_n$

Table 3. Effect of Polishing Solutions on Cleaved and Annealed $\{100\}$ Faces of KBr Crystals

Chemical Polishing Solution	Polishing Time (min)	Average Rate of Surface Removal (microns/min)	Appearance of Surface
95% Ethanol	1	1.07	No change; scratches and plateaus remain sharp
	2	1.12	No significant change
	4	1.14	No significant change; scratches still remain
90% Ethanol	1	2.35	Brighter surface, but scratches and plateaus remain
	2	2.60	No significant change
	4	2.75	Brighter surface, edges of steps rounded
85% Ethanol	1	7.10	Brighter surface, most scratches removed, steps and hillocks remain
	2	7.20	More pronounced rounding of plateaus
	4	7.24	Bright surface, but pits and hillocks are now sharper
Conc. Hydrobromic Acid	1	8.43	Very bright surface, scratches removed, rounded plateaus, some sharp steps remain
	2	9.30	Fewer edges but some well-defined hillocks (Figure 6 b)
	4	9.19	Very bright and smooth specular surface, only a few small hillocks remain

Table 4. Preliminary Results of Controlled-Contour Chemical Polishing of Cleaved KBr Surfaces with 85% Ethanol

Wheel Surface	Wheel Speed	Solution Feed Rate	Crystal Feed Rate	Polishing Time	Rate of Surface Removal	Surface Appearance
velvet pad	35 RPM	1 drop/SPC	0	5 min	15 micron/min	bright; slight ripple and orange peel effect
"	"	"	3.4 microns/min	10 min	16.8 "	bright, slight ripple and orange peel; very slight scratches (Figure 6b)
"	"	"	6.9 "	"	18.5 "	slightly dull; slight ripple and orange peel with very fine scratches
"	"	"	constant hydrostatic	"	32.3 "	dull with light scratches; slight ripple and orange peel effect
glass plate	22.5 RPM	0.5 mℓ/sec	21.6 microns/min	5 min	not measured	very bright, very few hillocks, slight ripple (Figure 7)

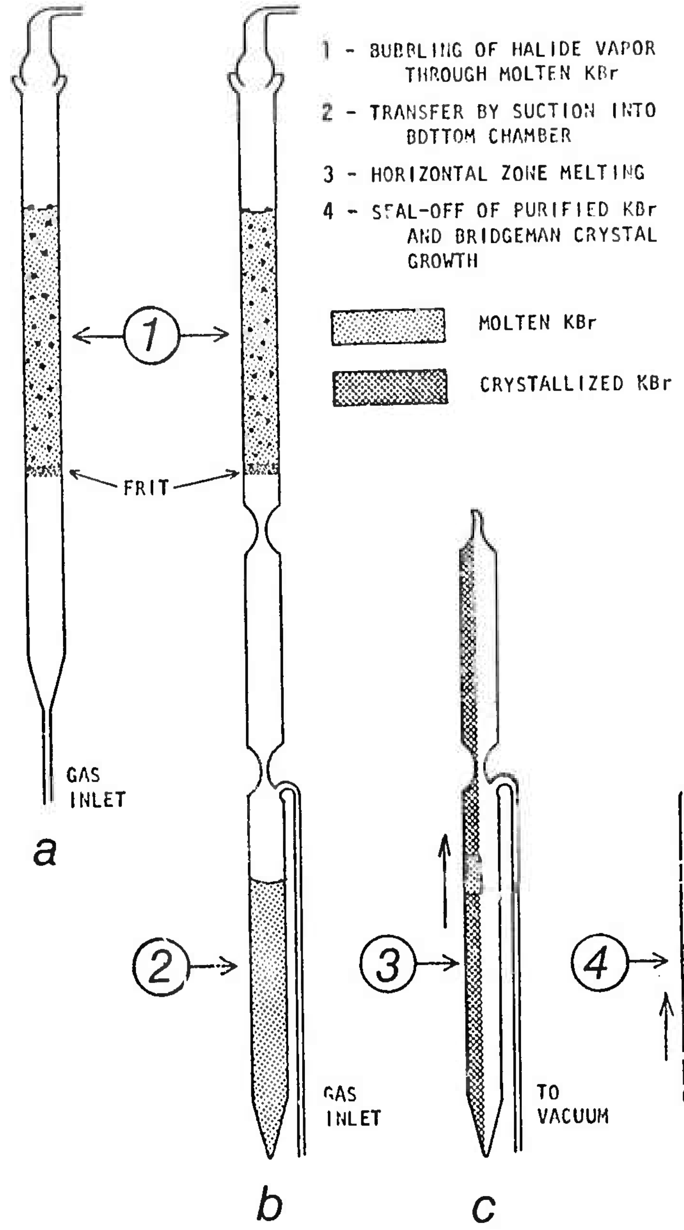

Figure 1. Apparatus for (a) bubbling reactive gases through molten KBr and for sequential (b) vapor treatment, (c) zone melting, and (d) crystal growth.

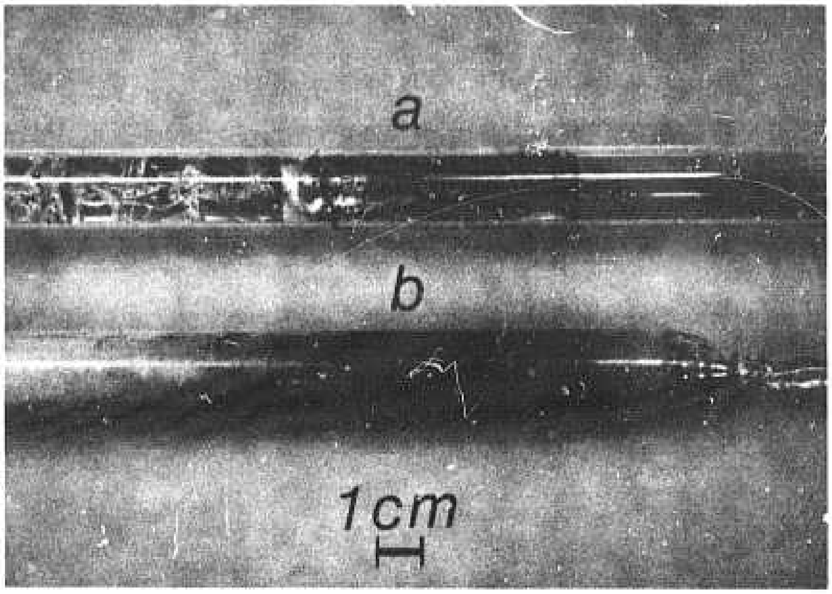

Figure 2. Concentration of brown impurity at terminal end of KBr crystallization during (a) unidirectional solidification and (b) four zone melting passes.

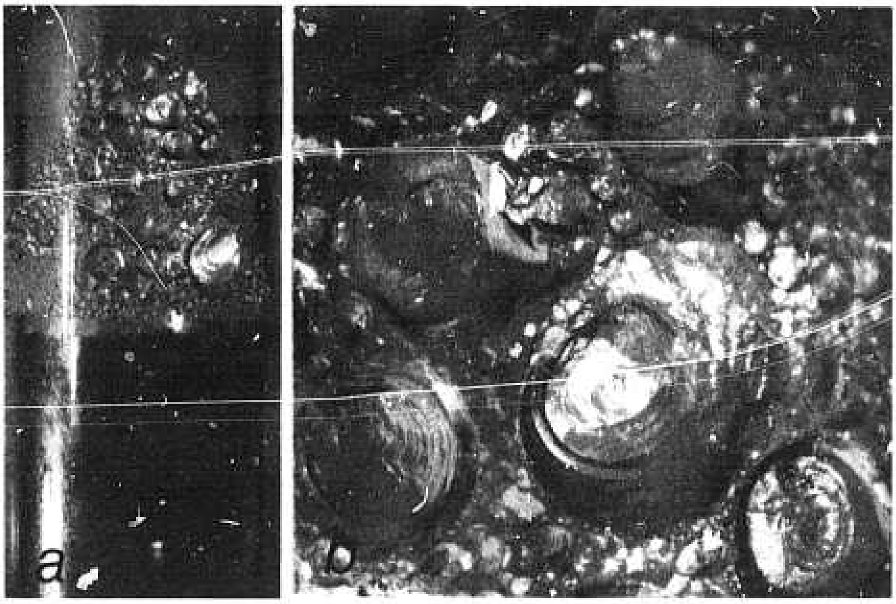

Figure 3. Close-up of vapor grown KBr crystals in Fig. 2(a): (a) 2.1x, (b) 11.5x.

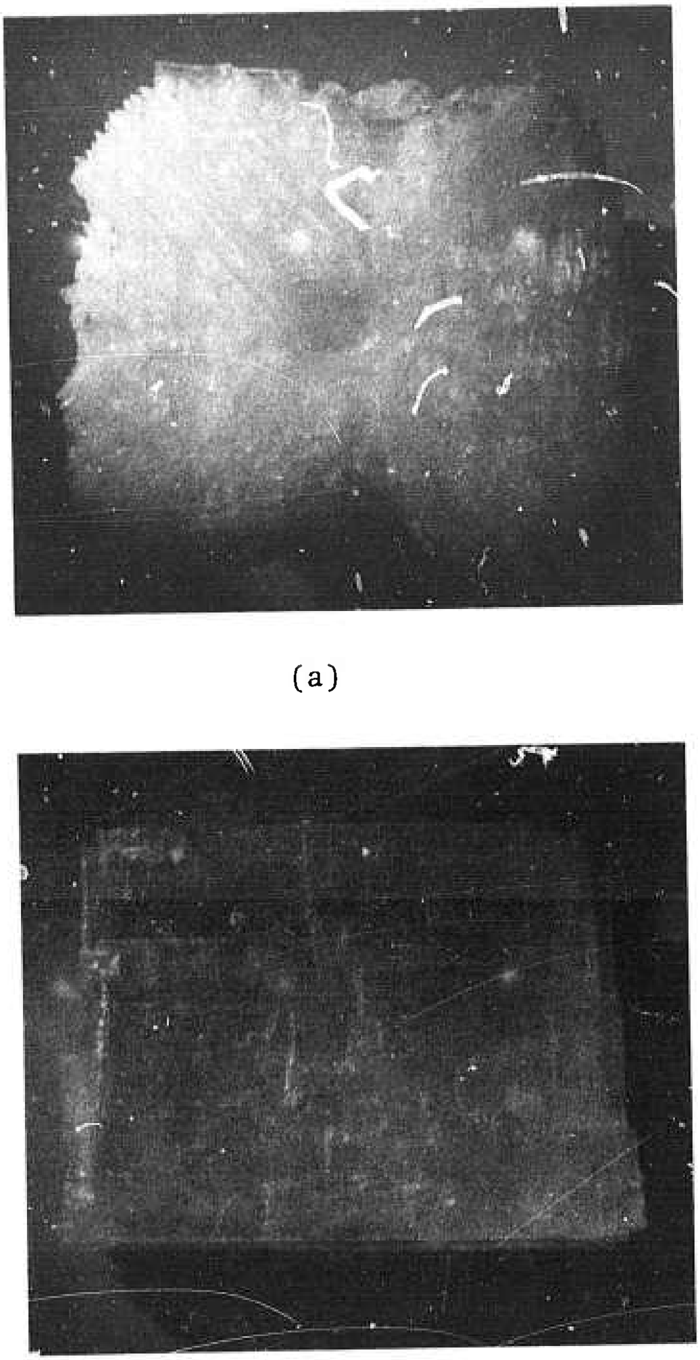

(a)

(b)

Figure 4. KBr crystals grown from aqueous solution: (a) spontaneous nucleation, (b) overgrowth on seed crystal (5x).

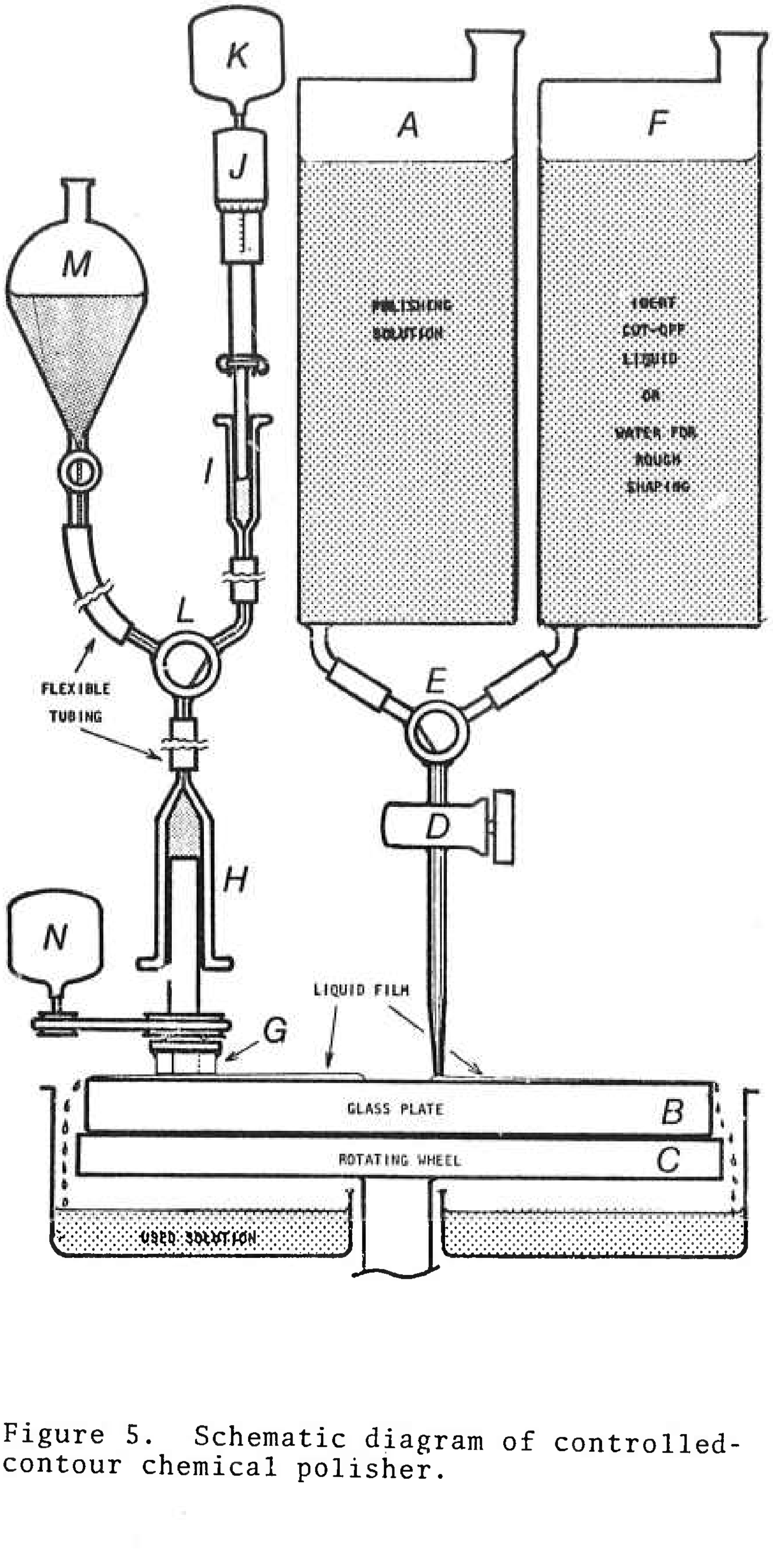

Figure 5. Schematic diagram of controlled-contour chemical polisher.

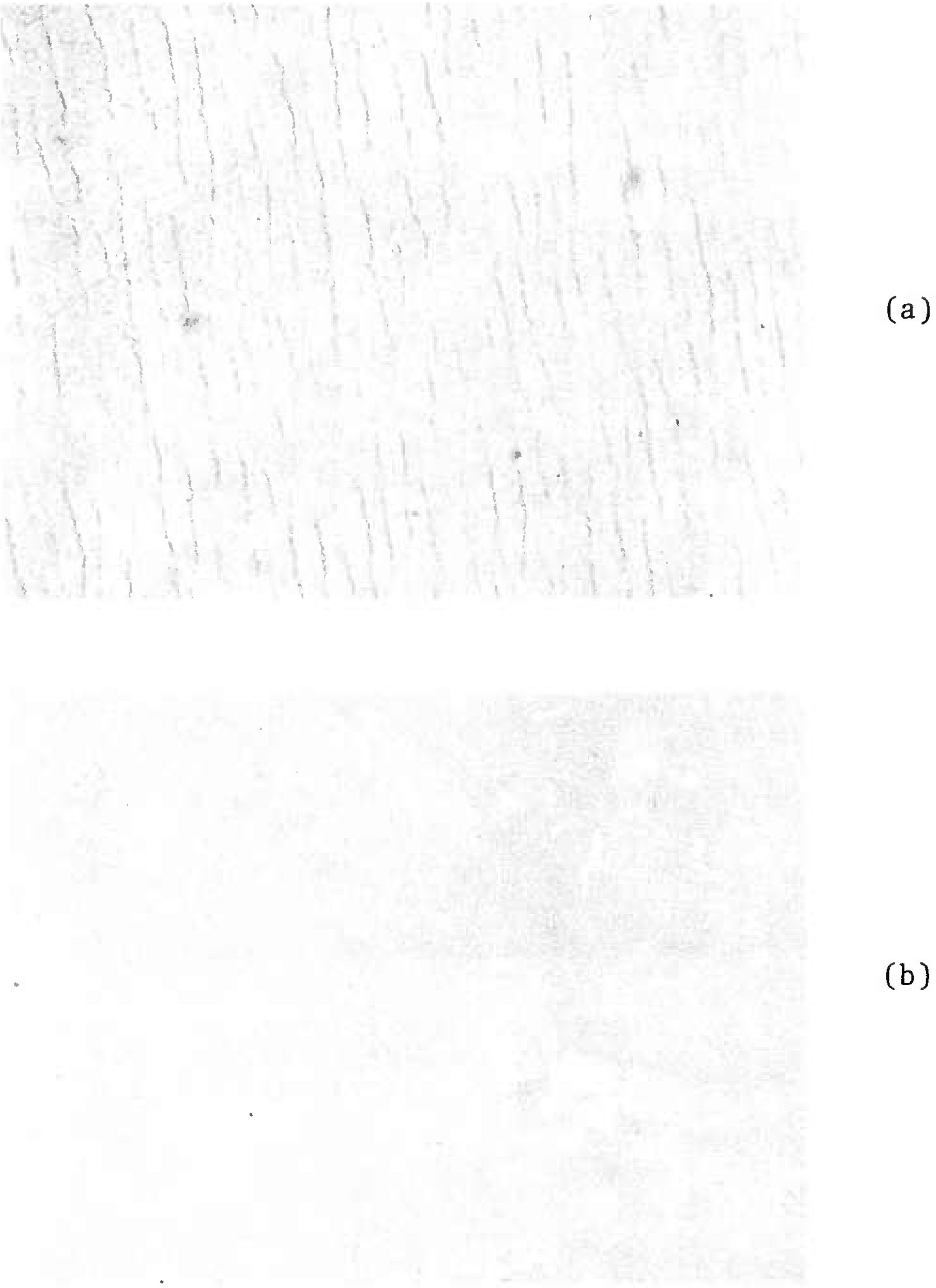

Figure 6. Effect of pre-annealing on surface of KBr crystal polished with concentrated hydrobromic acid: (a) unannealed (70x), (b) annealed (50x).

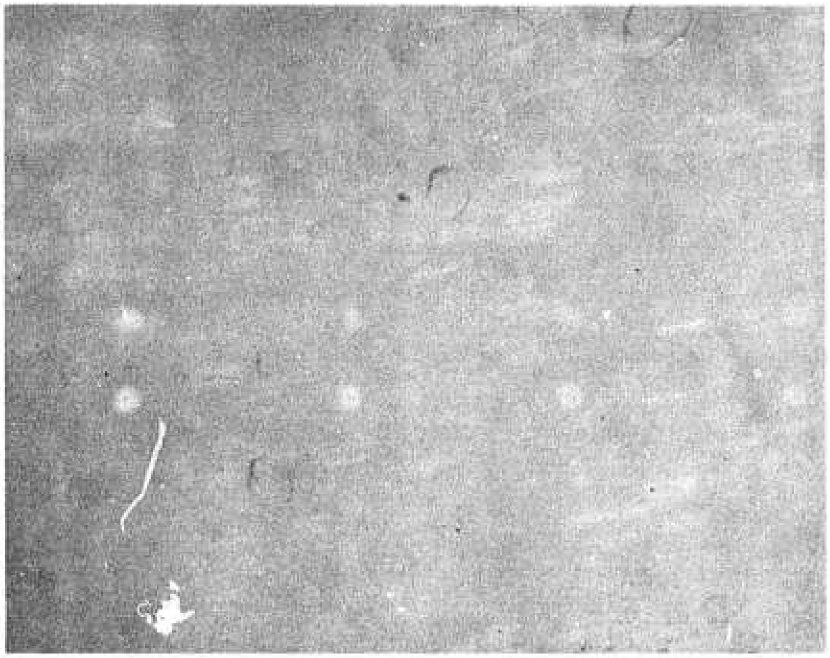

Figure 7. Controlled-contour chemically polished surface of KBr crystal, using 85% Ethanol on rotating glass plate (100x).

Strain-Optic Coefficients

W. Steier, R. Joiner, C. P. Christensen

In the previous progress report we described the experimental method and gave some preliminary results of measurements on ⟨111⟩ oriented CdTe. Since then, we have carefully analyzed the experiment and found that several of the assumed conditions were not met and that because of this the earlier measurements on CdTe were probably in error. This analysis led to several changes in the experimental set-up:

(1) The acoustic frequency was increased from 50 MHz to 150 MHz to assure that scattering of the IR beam took place in the Bragg regime.

(2) The IR power was reduced to avoid variations in detection sensitivity due to heating of the Ge:Au detector element.

(3) We began measuring the energy of the scattered optical pulses rather than peak power. This was necessary because the red and IR beams had different diameters and Bragg angles which caused the scattered pulses to have different time dependence. The time dependence is determined by the integrated sound intensity each beam sees as it crosses the sound column at the Bragg angle. A boxcar integrator is being used to provide time integration of the scattered optical pulses.

(4) The IR beam diameter was increased since according to Gordon[3] the diffracted intensity is difficult to calculate unless the acoustic divergence angle is greater than the light divergence angle. If the condition is not met, not all of the light will phase match with the sound.

(5) The CO_2 laser was stabilized to reduce the noise and increase the measurement accuracy.

Measurements on GaAs provide a check of our experimental technique since Dixon[1] has earlier measured GaAs at 1.15μ and the theory of Bendow, et al.[2], extends these results to 10.6μ . Two samples of high quality GaAs, one oriented with sound propagating along a ⟨111⟩ and one with the sound along ⟨100⟩ were measured. The following results were obtained:

⟨100⟩	⟨111⟩	
$p_{11} = -0.147$	$p'_{11} = -0.182$	$p'_{11} = \frac{1}{3}(p_{11} + 2p_{12} + 4p_{44})$
$p_{12} = -0.092$	$p'_{12} = -0.07$	$p'_{12} = \frac{1}{3}(p_{11} + 2p_{12} - 2p_{44})$

The consistency of the measurements can be checked by calculating p_{44} by these equations:

$$p_{44} = \frac{3p'_{11} - p_{11} - 2p_{12}}{4} = -0.054;$$

$$p_{44} = \frac{p'_{11} - p'_{12}}{2} = -0.056;$$

$$p_{44} = \frac{-(3p'_{12} - p_{11} - 2p_{12})}{2} = -0.061 .$$

We then compared our results with theory, and 1μ experimental values.

Our measurements at 10.6μ	Dixon measurements extended to 10.6μ by B-G theory	Dixon measurements at 1.15μ
$p_{11} = -0.147$	-0.148	-0.165
$p_{12} = -0.092$	-0.158	-0.140
$p_{44} = -0.055$	-0.055	-0.074

The numbers are in good agreement with the exception of p_{12}, which we observed to be definitely smaller than p_{11}. The discrepancy is much larger than our expected experimental error. Samples of CdTe are also being prepared for remeasurement of these coefficients.

References

1. R. W. Dixon and A. N. Chester, Appl. Phys. Lett. 9, 190 (1966).
2. B. Bendow, P. D. Gianino, S. S. Mitra, Y. Tsay, Third Conf. on High Power I.R. Laser Window Materials, 367 (1973).
3. E. I. Gordon, Proc. IEEE 54, 1391 (1966).

Theoretical Studies of Absorption Mechanisms in IR Window Materials

R. W. Hellwarth and M. Mangir

In this period we have continued with our efforts to determine the multiphonon absorption mechanisms using a method that we have developed and explained in previous reports. In particular we are working on the application of this method to ZnSe. This method requires the measurement of refractive index as a function of temperature and frequency in the IR. We have proceeded with our experiment and we are now obtaining and numerically analyzing our refractive index data on ZnSe.

In detail, we have finished cutting, polishing and coating two CVD grown polycrystalline ZnSe prisms, to be used in a Littrow configuration for refractive index measurements, as shown in Figure 1. We have made the necessary conversions on the Perkin-Elmer model 13 spectrophotometer, also shown in Figure 1, including converting it to a diffraction grating instrument from a prism instrument, to obtain more precise data. We have calibrated this instrument in terms of known absorption lines of gases in the IR. We have built a special oven to house the prism at constant and uniform temperature from 20 to 330°C, while allowing it to be rotated accurately.

We have now measured the change in refractive index with temperature from 22 to 335°C at 6 different temperatures and at 5 discrete frequencies from 4 to 15μ.

During the following months we will: a) obtain more data at different frequencies in the above range, and b) analyze our data using the formulae (given in previous reports and publications) that relate this data to the nonlinear dipole moment parameters. With this, the importance of the nonlinear moment to n-phonon absorption in ZnSe will be established, at least for lower values of n.

Figure 1. Schematic of infrared prism refractometer

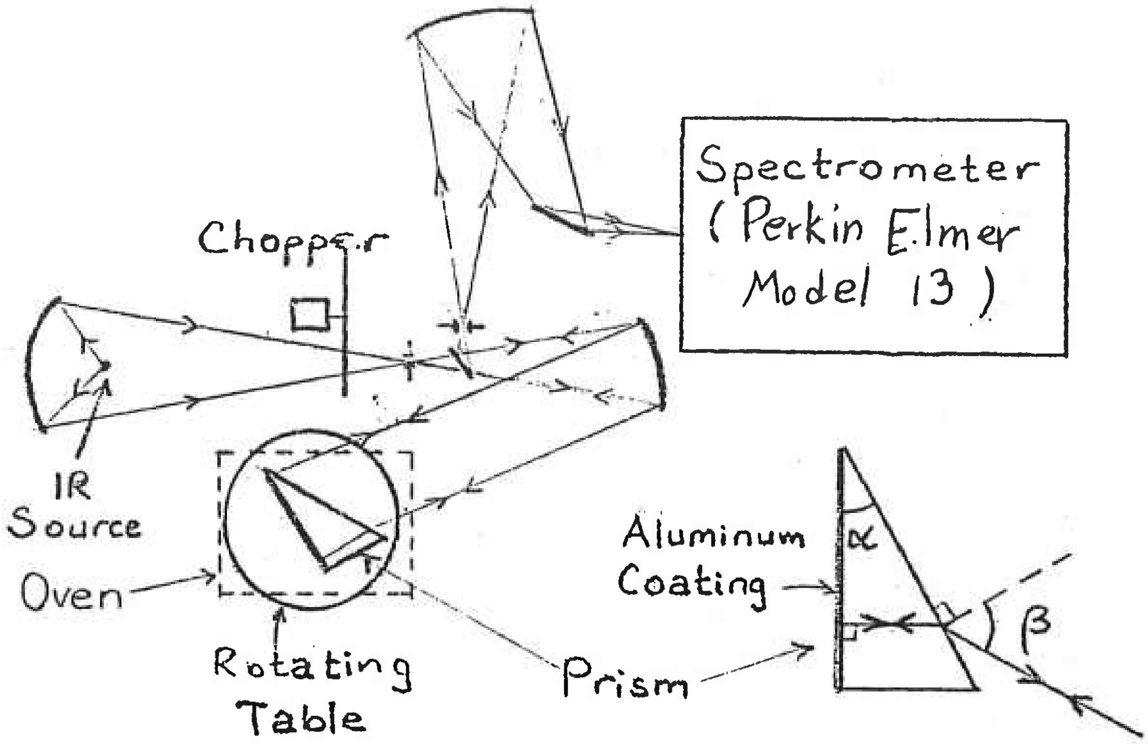

Surface Studies with Acoustic Probe Techniques

J. H. Parks and D. A. Rockwell

During this contract period, surface wave phase variations induced by the absorption of 10.6μ radiation have been measured on KCl surfaces. The surface absorption σ of these samples were measured by calorimetry to be $\sigma \sim 2 \times 10^{-4}$, and acoustic probe measurements on the same samples yielded $\sigma \sim 1 \times 10^{-4}$. Initial results of recent studies on both polished and etched alkali halide surfaces are discussed in the following paper presented at the 1975 Symposium on Damage in Laser Materials, Boulder, Colorado.

1. Introduction

Infrared absorption measurement techniques have been developed [1] which avoid the effects of the surface contribution. However, the surface absorption represents a practical limitation of high power laser optical materials and an understanding of the details is needed. The principle effort of our research program has been to develop a new measurement process [2,3] which utilizes acoustic surface waves to detect the surface depth dependence of radiative absorption. In addition a detailed theoretical analysis of this detection process was derived to relate these measurements to a quantitative model of surface absorption phenomena.

These new experimental techniques and the related theoretical analysis involved advances beyond the current state of acoustic surface wave technology. In particular, it was necessary to develop techniques to propagate surface waves on non-piezoelectric solids which did not alter the surface characteristics under study nor require any special surface treatment.

Initial results of recent studies are presented which measure radiative absorption on KCl surfaces. Surface absorption of 10.6μm radiation was measured for both mechanically polished and chemically etched surfaces.

2. Surface Wave Detection of Radiative Absorption

A fundamental understanding of the physics involved in the surface wave detection of radiation was obtained in quantitative studies [2,4] on well known acoustic materials (α-quartz, lithium niobate). It was shown that surface wave propagation in a region heated by radiative absorption could be accurately described by a laser induced transient phase change given by

$$\Delta\phi(t) = \frac{4\pi\nu}{v_{so}} f_B \int_o^L [\epsilon_r(t) - \alpha_v \Delta T(t)] dr. \qquad (1)$$

Equation (1) is valid when the temperature distribution is essentially uniform over the surface wave penetration depth, or $\partial T/\partial z \ll T/\lambda_s$. Here λ_s is the acoustic wavelength and z is a distance normal to the surface. The phase change arises from a change in propagation path length via thermoelastic strains, $\epsilon_r(t)$, and also a change in wave velocity through the temperature variation of the elastic coefficients represented by $\alpha_v \Delta T(t)$. In eq. (1), ν is the frequency and v_{so} is the velocity of the surface wave, 2L is the acoustic path length, and r is the distance along the propagation path. The laser induced temperature change $\Delta T(t)$ is found by solving the heat equation, and has the spatial dependence of the gaussian laser profile. The factor f_B accounts for the incomplete overlap of the acoustic beamwidth and the temperature profile.

Experimental measurements of $\Delta\phi$ on α-quartz and lithium niobate were compared with theoretical calculations of eq. (1) using no adjustable parameters. The quantitative agreement between theory and experiment was within 15%. In these experiments, the radiative pulse widths were long enough for heat diffusion to produce a uniform temperature within the surface wave penetration depth. In this way, the need to account for propagation in the presence of an axial temperature gradient was avoided, and the resulting analysis provided a clear picture of the fundamental surface wave thermal interaction leading to the induced phase changes.

2.1. The Effect of a Temperature Gradient

Depending on the surface wave frequency and the extent of thermal diffusion, it may not be valid to assume that the temperature is uniform over the surface wave penetration depth. In the presence of such a spatial inhomogeneity, surface wave propagation becomes dispersive. In this case, measurement of the frequency dependence of the induced phase change yields information about the temperature distribution and consequently the surface absorption properties.

The contribution of the velocity variation to the phase change in eq. (1) cannot be represented by $\alpha_v \Delta T$ for propagation in the presence of an arbitrary temperature gradient. In this case the phase change is given by

$$\Delta\phi = -\frac{4\pi\nu}{v_{so}} f_B \int_0^L \left[\frac{\Delta v_s}{v_{so}}\right]_{\lambda_s} dr, \qquad (2)$$

when the strain contribution is negligible. The wavelength dependent velocity variation $[\Delta v_s/v_{so}]_{\lambda_s}$ follows from a perturbative treatment [5] of the wave equation in which the elastic coefficients exhibit spatial variation through their known temperature dependence. The perturbation approach allows a precise model of radiative absorption to be easily incorporated into the analysis.

Experimental measurements of the dispersive phase change have been made on Y-cut α-quartz [4]. In this case the exceptionally high bulk absorption coefficient of 241 cm^{-1} at 10.6 μm in quartz is responsible for a significant temperature gradient over the acoustic penetration depth. In the following section it will be shown that a surface absorption layer extending only several microns into a relatively transparent solid will also induce a temperature gradient and dispersive wave propagation.

3. Infrared Surface Absorption

In weakly absorbing materials the radiative absorption coefficient within 1-10μm of the surface can be significantly different than values for bulk absorption. The extent of this surface absorption depends on surface preparation including mechanical polishing and chemical etching procedures, immediate environmental impurity adsorption, and perhaps on the effects of surface dislocations induced during sample preparation. The resulting effect of these surface perturbations can be described by taking the radiative absorption coefficient to be a function of depth below the surface $\beta(z)$. A simple absorption model for weakly absorbing materials is shown in figure 1. The highly absorbing surface region, $\beta_s cm^{-1}$, extends a characteristic distance d into the material at which a transition to the bulk value $\beta_B cm^{-1}$ occurrs. This model adequately represents the material absorption properties in the region probed by the surface wave, Although the sharp transition region from β_s to β_B may be somewhat unphysical, thermal diffusion during the laser puslewidth causes the acoustic probe measurement to be relatively insensitive to the finer details of the model.

Applying this model to express the intensity absorbed, we solve a one dimensional heat equation to find the resulting temperature increase in terms of the parameters $\Delta T(\beta_s, d, \beta_B)$. The peak dispersive velocity variation is then derived using this temperature evaluated at the time $t = \tau_p$ which yields

$$\left[\frac{\Delta v_s}{v_{so}}\right]_{\lambda_s,\tau_p} \propto \sum_n \Delta T_n(\beta_s, d, \beta_B) \cdot A_n(\lambda_s/Z_T) \qquad (3)$$

Here the sum is extended over the fourier temperature coefficients ΔT_n which characterize the absorption depth distribution. The factor A_n contains the dispersive behavior as a function of the variable λ_s/Z_T, where $Z_T(\tau_n)$ is the characteristic depth of the temperature distribution at $t = \tau_p$. This depth is determined primarily by thermal diffusion and thus dependent on the pulsewidth τ_p. The variable becomes $\lambda_s/Z_T \ll 1$ for long times during which the temperature becomes uniform over the surface wave penetration depth, or for high frequency surface waves. In this case A_n approaches a constant independent of wavelength indicating the ordinary regime of dispersionless surface wave propagation.

When the pulsewidth τ_p is short enough so that $d \leq Z_T \ll \lambda_s$, the measured phase changes will be sensitive to each of the parameters β_s, d and β_B independently and the complete distribution of the absorption coefficient may be determined. However, if the pulsewidth is long enough so that $d \ll Z_T \leq \lambda_s$, dispersive propagation may be observed but the phase change will essentially be sensitive only to the product $\sigma=\beta_s d$. This parameter σ, usually referred to as the surface absorption, is included in calorimetric measurements of the percentage power absorbed by a sample of length L in the form

$$\frac{\Delta P}{P} = 2\sigma + \beta_B L. \tag{4}$$

When the surface absorption 2σ, from both surfaces, is comparable to the bulk absorption $\beta_B L$, the surface contribution is not separable by calorimetric techniques. However, the acoustic probe technique will yield σ independently even in this case, since $\beta_B d << \beta_s d$ is usually satisfied in weakly absorbing materials.

3.1. Application of the Absorption Model to KCl

In KCl the bulk absorption of good samples is known [6] to be as low as $7x10^{-5}cm^{-1}$. However, radiative absorption occurring in a thin surface layer is significantly greater, and leads to appreciable temperature gradients within the acoustic penetration depth. As an example the absorption model shown in figure 1 is applied to radiative absorption at 10.6μm in KCl using the parameters $\beta_s=10cm^{-1}$, $d=2\mu m$, and $\beta_B=2x10^{-3}cm^{-1}$. The resulting temperature depth profiles are shown in figure 2 for radiative pulsewidths of 10 msec and 100 msec. In the absence of a highly absorbing surface layer. The presence of such temperature gradients at 10 msec would require a bulk absorption coefficient of ~200 cm^{-1}. The measurement of dispersive surface wave propagation, resulting from these temperature gradients, is then a direct indication of the existence of highly absorbing surface layers on weakly absorbing materials. The depth profiles of the acoustic energy are also shown in figure 2 for surface waves of frequency 28 MHz and 124 MHz. For $\tau_p=10$ msec we note that $d<<Z_T\simeq\lambda_s$ resulting in the conditions for dispersive propagation. However, for $\tau_p=100$ msec, dispersion would not be observed for these frequencies since $Z_T>>\lambda_s$. In both these cases $Z_T>>d$, which implies the acoustic probe phase changes would measure the magnitude of σ and not the complete set of distribution parameters.

The phase changes $\Delta\phi$ induced by the temperature gradient are shown in figure 3. The phase change per input laser power is plotted versus radiative pulsewidth. The curviture in these graphs is a measure of the effect of thermal diffusion. The acoustic probe at 28 MHz, with a penetration depth of ∿150μm, is much less sensitive to the redistribution of thermal energy that the 124 MHz probe having a penetration depth of ∿35μm.

In the limit of long pulsewidths, we note that $(\Delta\phi 28MHz/\Delta\phi 124MHz)\simeq 0.23$ which is simply the frequency ratio as predicted by eq. (2) for the phase change in this non-dispersive limit. However, for $\tau_p=10$ msec, we find $(\Delta\phi 28MHz/\Delta\phi 124MHz)\simeq 0.19$ which indicates the dispersion effects the order of 20%. To emphasize the effect of dispersion, figure 4 shows a log-log plot of the reduced phase change ($\Delta\phi$ per unit input power and per unit frequency) which eliminates the explicit frequency dependence given in eq.(2). These curves should coincide as dispersion vanishes for long τ_p. The increasing effect of dispersion for short τ_p reaches ∿43% at $\tau_p=0.1$ msec.

4. KCl Surface Studies

4.1. Coupling Surface Waves to KCl

The application of the surface wave measurement technique to KCl requires the ability to propagate waves on the surface of a non-piezoelectric material. This wave propagation must be generated by a technique which does not affect the surface properties under analysis. The technique should also be easily applicable to samples without additional preparation. A fluid coupling technique has been developed which satisfies both these requirements. As shown in figure 5, the surface wave is initially excited on a piezoelectric material (α-quartz) and subsequently coupled through a fluid layer onto the KCl surface. The inverse coupling returns the wave to the detection transducer. Although this method has previously received relatively little development, it is of a particular advantage for our purpose.

Our research has included an experimental study [7] of a fluid coupling technique which has resulted in successfully coupling surface waves to KCl. Phase changes on piezoelectric samples using the fluid coupling technique were compared with the results using direct surface wave excitation by interdigital transducers. This comparison verified that the laser induced phase change was reliably and reproducibly coupled through the fluid regions. Ortho-dichlorobenzene was used as the coupling fluid in these experiments. An experimental transducer configuration has been designed which accepts arbitrary samples sized and provides ample access to the sample surface for the infrared laser sources.

4.2. KCl Experimental Results

Experimental measurements of induced phase changes on KCl were obtained as shown in figure 6. The fluid layer used to couple waves to the KCl surface has been deleted for clarity. The RF reference signal and the transmitted RF signal are combined in a double balanced mixer which provides an output proprotional to the sine of the phase change. The amplitude V_0 was typically ~200 mV. The peak phase change signal was detected by a digital peak voltmeter and averaged by a PAR Boxcar. Surface wave frequencies of 124 MHz, 62MHz, and 29MHz were used in these studies.

A CO_2 laser pulse of ~65 watts was incident on the KCl samples with pulsewidths ranging from 2 msec to 100 msec. The pulse repetition rate was varied to maintain a constant duty cycle, D=.05, and the average power for each pulsewidth value was $<P>\simeq 3$ watts. The signal/noise improvement ratio provided by the Boxcar (during 80 sec exposures and a time constant of 1 sec) was 15-30 for the shortest pulsewidths. Typical KCl phase change signals detected after amplification by the peak detector are shown in figure 7. Note that the signal detected for a pulsewidth of τ_p=0.5 msec required a CO_2 laser pulse energy of only ~35 mJ. The RMS phase noise at 124 MHz observed in the absence of incident radiation was $\delta(\Delta\phi)_N \simeq 0.2$ mrad.

Induced phase change data on KCl are shown in figure 8. Polished and etched samples of Harshaw KCl were measure and are referred to as Chemical Polish. These samples were then repolished mechanically at USC using standard techniques and measurements taken are referred to as Mechanical Polish. Although 3-frequency data were obtained for the Chemical Polish sample, mechanical repolishing introduced enough surface roughness to cause excessive scattering at 124 MHz. Previous measurements on expertly polished Hughes samples have been obtained routinely at 124 MHz. The absolute experimental uncertainty in the phase change measurements was typically 15%.

The data indicate that chemically etched surfaces provide a reduction of the surface absorption σ by at least a factor of 3-4. Similar results have been observed [8] in calorimetric measurements of KCl absorption. Figure 9 shows evidence of dispersive phase changes measured on the chemically etched sample. This is interesting since it indicates the presence of a surface absorption layer even after several microns of material have been removed during a 60 sec etch in concentrated HCl. An initial analysis of this data yields a surface absorption value $\sigma \simeq 1x.0^{-4}$ for the chemically polished Harshaw sample. Calorimetric measurements on the same sample yield consistent results $\sigma \simeq 2x10^{-4}$ assuming a value of $\beta_B = 10^{-3}$ cm^{-1} used in eq. (4).

5. Acoustic Probe Sensitivity

The present results indicate the sensitivity of these surface wave techniques. If it is only required to obtain a <u>relative</u> measurement of surface absorption for different samples, the measurement can be taken at a single frequency and a single pulsewidth. We have found a phase change $\Delta\phi$=60 mrad at 124 MHz for a 100 msec, 70 watt pulse on a surface with $\sigma \sim 1x10^{-4}$. A surface absorption of $\sigma \sim 2x10^{-6}$ could be detected, $\Delta\phi \sim 1$ mrad., with the same laser pulse. This limit could be reduced further by operating at higher laser power. It is also important to point out that a laser pulse energy of only ≤25 mJ at τ_p=1 msec would be required to measure $\sigma \sim 1x10^{-4}$ with a phase change $\Delta\phi \sim 1$ mrad.

However, <u>dispersive</u> phase change measurements require data at lower frequencies and shorter pulsewidths. Since the phase change is directly proportional to the frequency, the sensitivity will be reduced if depth dependence of the absorptive properties is of interest. For example, the smallest phase change at 28 MHz was measured for a 2 msec, 70 watt pulse on a surface with $\sigma \sim 1x10^{-4}$. Since this was a factor of 2-3 above the noise a surface absorption of $\sigma \sim 5x10^{-5}$ represents a lower limit at this power for measuring an accurate, absolute value for σ from dispersive phase changes. This limit is comparable to the lowest surface absorption obtained on etched samples [6]. If it is desirable to determine the surface absorption parameters β_s and d independently, it is necessary to use radiative pulsewidths on the order of $\tau_p \lesssim 10$ μsec. Present TEA lasers (CO_2, HF, and DF) can provide sufficiently short pulses of high enough energy for such measurements.

6. Concluding Remarks and Planned Applications

The principle accomplishment of this research program has been the successful development of the surface wave measurement process and its associated theoretical description as a reliable research tool to detect and measure the details of weak surface absorption. This technique has been applied to studies of KCl after a method was developed to couple surface waves to non-piezoelectric samples. Results on KCl indicate a high sensitivity to the details of low level surface absorption. Current research plans include:

- measurement of β(z) distribution on KCl surfaces
- measurement of σ on ZnSe
- absorption in thin films
- impurity diffusion into alkali-halide surfaces.

7. Acknowledgements

The authors wish to thank S. Allen, and A. Timber, Hughes Research Laboratories, for the KCl samples and their preparation. They also thank D.White and R.King, China Lake,NWC,for trensducer fabrication.

8. References

1. M. Haas, J. W. Davisson, H. B. Rosenstock, and J. Babiskin, Proc. Int. Conf. Opt. Prop. Highly Transparent Sol., paper VI-B (Waterville, N.H. 1975).

2. J. H. Parks, D. A. Rockwell, T. S. Colbert, K. M. Lakin, and D. Mih, Appl. Phys. Lett. 25, 537 (1974).

3. D. A. Rockwell, T. S. Colbert, and J. H. Parks, in Proceedings of the International Conference on Optical Properties of Highly Transparent Solids, edited by S. S. Mitra and B. Bendow (Plenum, New York, 1975).

4. D. A. Rockwell and J. H. Perks, "Theory of Acoustic Surface Wave Detection of Radiative Absorption" (submitted for publication in J. Appl. Phys.).

5. B. A. Auld, Acoustic Fields and Waves in Solids, (Wiley, New York, 1973) Vol.II,p.294.

6. T. F. Deutsch, Appl. Phys. Lett. 25,109(1974).

7. D. A. Rockwell, and J. H. Parks, "A Technique for Acoustic Surface Studies of Non-Piezoelectric Materials" (to be published in J. Appl. Phys.).

8. H. G. Lipson, private communication.

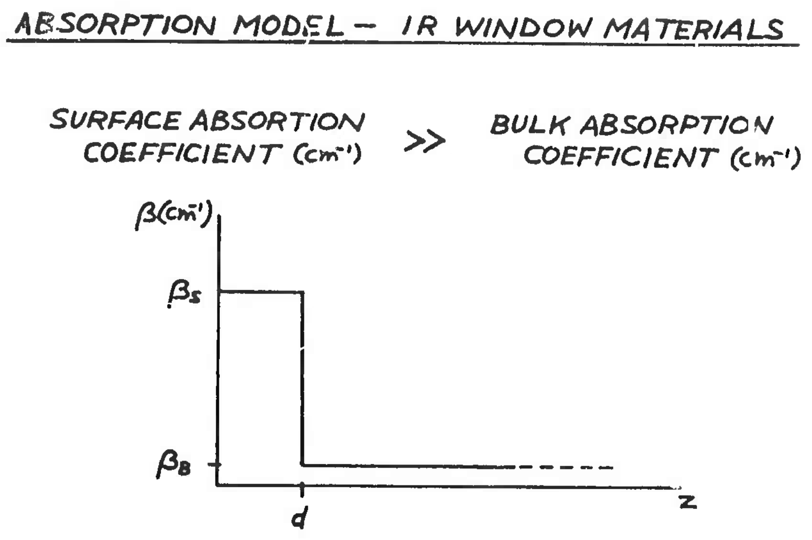

Figure 1. Absorption model for infrared window materials. The distribution $\beta(z)$ is used to calculate the temperature distribution and the induced phase changes measured on KCl surfaces.

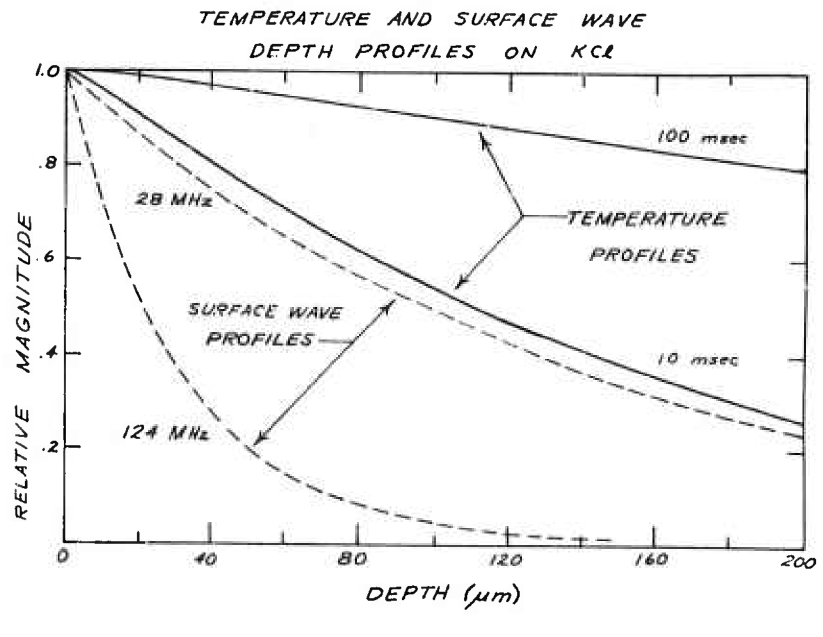

Figure 2. Temperature depth profiles for 10 and 100 msec laser pulsewidths calculated using the absorption model parameters $\beta_S=10cm^{-1}$, $d=2\mu m$ and $\beta_B=2x10^{-3}cm^{-1}$. The surface wave energy profiles at frequencies of 28 MHz and 124 MHz are shown for comparison.

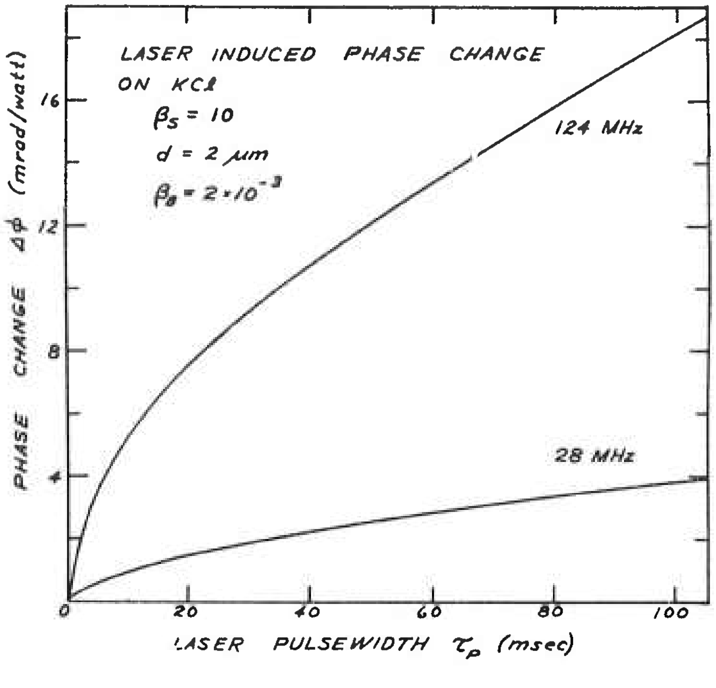

Figure 3. Laser induced peak phase change Δϕ (mrad per incident laser power) versus laser pulsewidth is shown for surface wave frequencies of 28 MHz and 124 MHz.

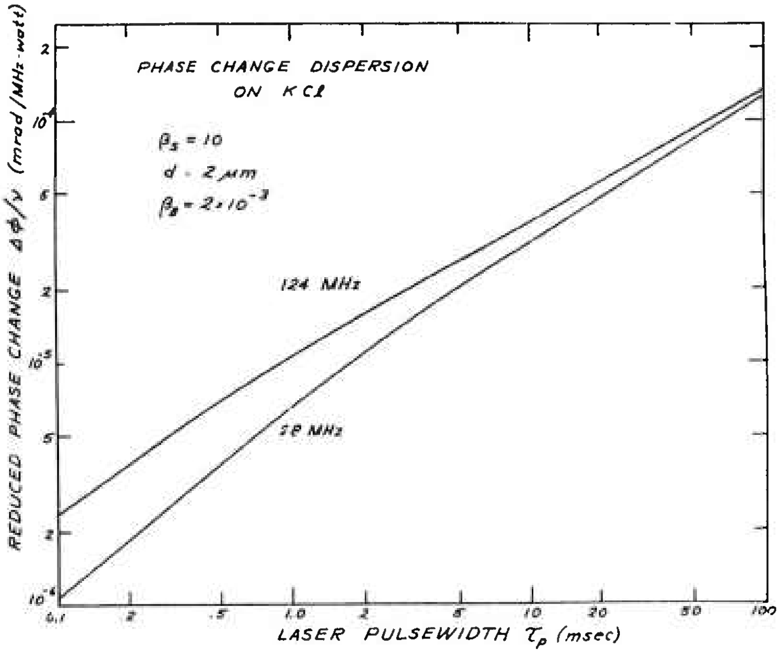

Figure 4. Log-log plot of peak reduced phase change (Δϕ per frequency and per incident laser power) versus laser pulsewidth. Dispersive propagation is indicated by divergence of graphs for different surface wave frequencies.

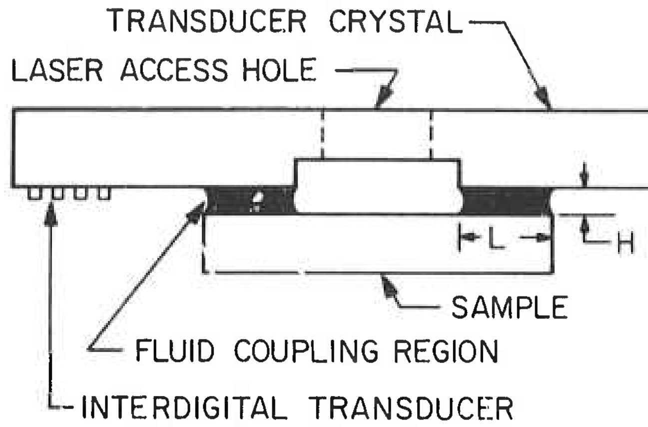

Figure 5. Schematic of the fluid coupling technique. Fluid interfaces couple the surface wave from (to) the piezoelectric transducer crystal to (from) the KCl sample.

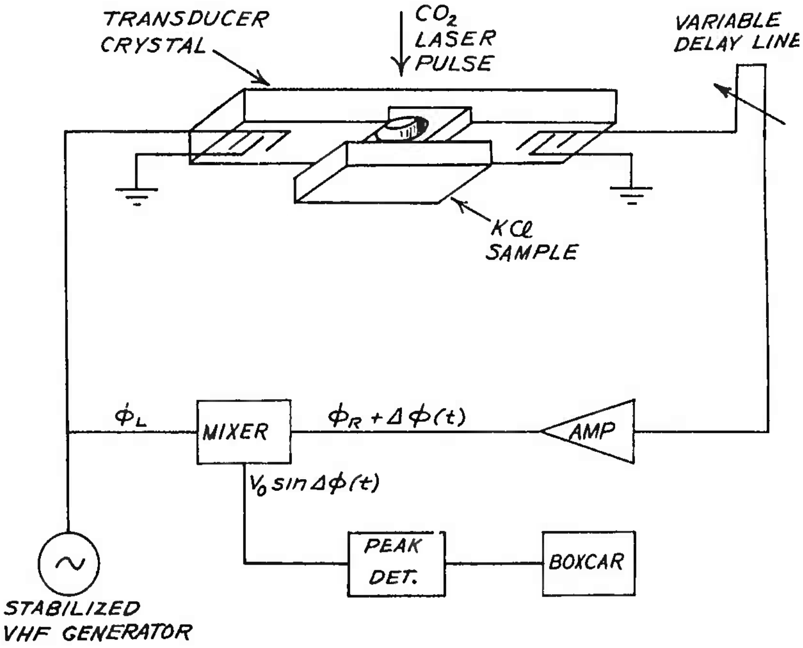

Figure 6. Experimental apparatus for measuring laser induced phase changes on KCl surfaces.

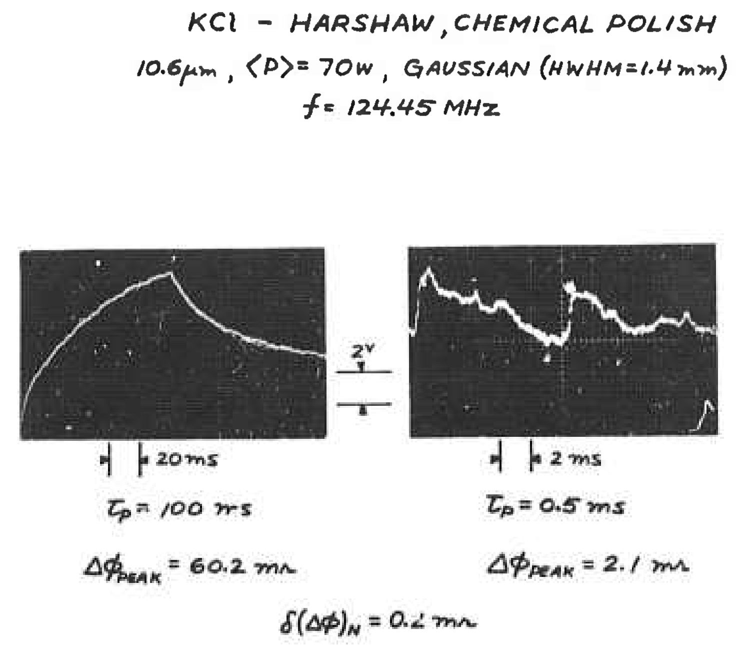

Figure 7. Typical oscilloscope data traces of the transient phase change induced on KCl by laser pulses of 0.5 and 100 msec pulsewidths. Scales are indicated for each trace as well as other pertinent data. $\delta(\Delta\phi)_N$ is the RMS noise value of the phase change measured in the absence of radiation.

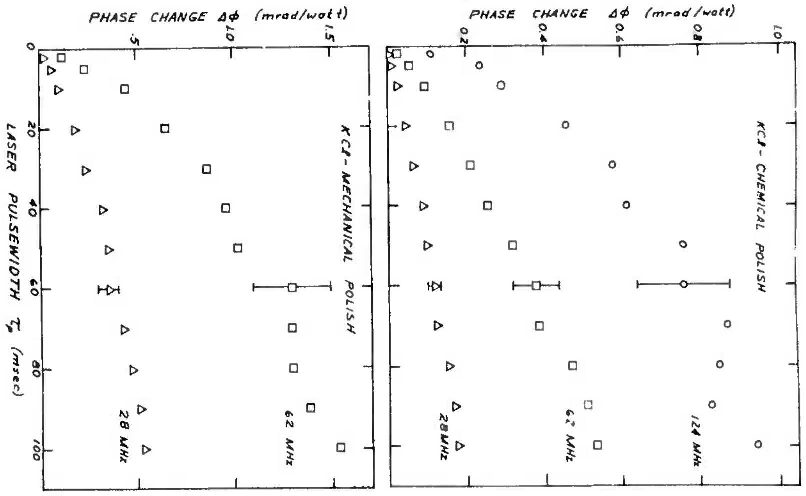

Figure 8. Phase change data versus pulsewidth at various frequencies for chemically polished and mechanically polished KCl surfaces. Bars indicate ±15% experimental uncertainty.

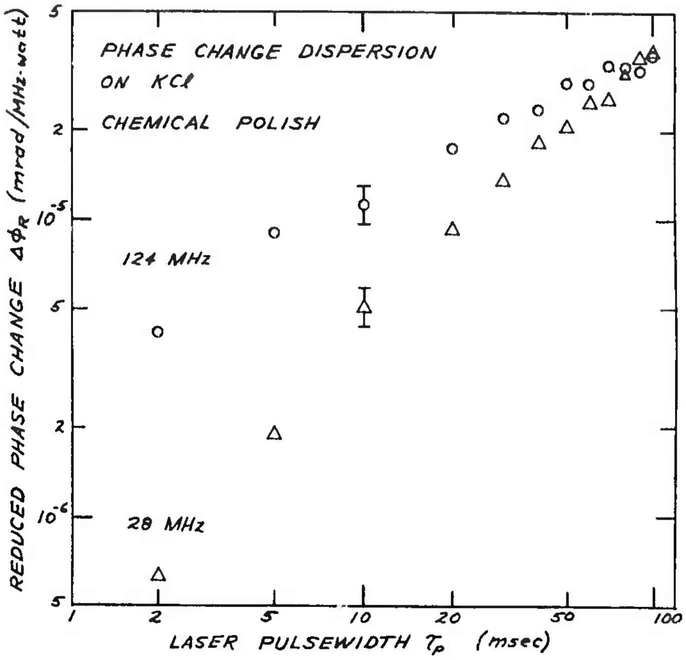

Figure 9. Phase change dispersion versus laser pulsewidth is indicated by the increasing divergence of $\Delta\phi$ as τ_p decreases. This data was taken on a chemically polished surface and experimental uncertainty is ±15%.

The Interaction Between Alkali Halides and Chemically Active Transient Species

C. Wittig

The interaction between various crystals and the active species that one is likely to encounter in a laser device is a matter of importance when trying to evaluate these materials with respect to their usefulness as components in high power IR lasers. With this in mind, we consider the interaction of atomic oxygen with alkali halide crystals. Atomic oxygen is present in many devices such as CO_2 and CO lasers and the interaction of O with alkali halides provides a convenient beginning point for this study. The principles involved are general and apply to many other situations.

Experimental:

The experimental apparatus is shown schematically in Fig. 1. Ultra high purity oxygen, at several mm Hg pressure, is passed through a 77^{o} K trap in a greaseless flow system and then discharged with a low power (40W) DC discharge. The discharge products are swept downstream and impinge on the sample some 12 cm from the discharge. The discharge products that are capable of surviving the 12 cm flow length are $O_2(^1\Delta)$, $O(^3P)$, O_3, and $O_2(v)$, where v denotes vibrational excitation of O_2 in the ground electronic state. Flow conditions are adjusted so that the dominant active species reaching the sample is atomic oxygen in its ground electronic state, $O(^3P)$. At the low pressures employed in these experiments, $O_2(v)$ will be deactivated at the wall and the formation rate of O_3 via a 3-body collision will be low. In all fairness, no estimate of $O_2(^1\Delta)$ is available at this time and this will be the subject of further investigation. Previous experience[1] with atomic oxygen leads us to conclude that $[O] \gg [O_2(^1\Delta)]$. Under the conditions of our measurements, atom concentrations of 10^{14}-10^{15} are typical.

After exposing the sample to discharged oxygen for several hours, the sample is removed and its transmission characteristics are measured with an IR spectrophotometer. All surfaces are either cleaved before use in order to ensure that only atmospheric contaminants are present on the surface, or polished with an ethanol-distilled water solution and treated with concentrated HCl solution. Ironically, no experimental differences were observed between crystals treated with either of these two techniques and surfaces that were untreated. All crystals were supplied by Harshaw.

Typical results for the case of NaCl are shown in Fig. 2. The prominent absorption characteristics are repeatable under many conditions (cleaved and uncleaved surfaces, many different crystals, exposure times, etc.) and are attributable to ClO_3.[2,3] It is noteworthy that the absorptions show no apparent saturation with respect to time as would be expected if simple surface layers of $NaClO_3$ were being formed. The strong absorptions shown in Fig. 2 are characteristic of an effective depth of pure $NaClO_3$ of 10-100nm. After long exposures (24 hrs), the surface develops a slight haze. Short exposures corresponding to several percent absorption do not result in noticeable surface deterioration. The variation of the absorption strengths with time are shown in Fig. 3. The data indicate that the buildup of absorbing species is diffusion limited. Since the surface is damaged by the formation of ClO_3, the diffusion of species through the surface is not a straight forward process. The diffusion rate is much too large to be due to ClO_3 diffusing through the bulk[4] and is due either to oxygen atoms diffusing through the bulk, or surface deterioration. Thus, it is not possible to distinguish between surface and bulk phenomena on the basis of the data in Fig. 3. When species such as N_2 or He are discharged in place of O_2 there is no measureable effect even though long lived active species are present in the afterglows of both N_2 and He.

When KCl or KBr samples are used, only a much weaker effect is seen. These data are shown in Fig. 4. This result was not anticipated and we were quite surprised by the resiliency of KCl and KBr compared to NaCl.

The differences between NaCl and KCl/KBr are not easily explained. In fact, if accommodation of the ClO_3 or BrO_3 species were important, then we would expect KCl or KBr to be <u>more</u> receptive to the inclusion of ClO_3 or BrO_3 than the NaCl, as shown in Fig. 5. The absorption features in KCl and KBr do grow steadily with time, indicating that a passivating layer is not being formed on the surface. The data shown in Fig. 3 do not indicate that <u>surface</u> reaction is less than for the case of NaCl, but merely that the buildup of oxidized material proceeds at a slower rate than for the case of NaCl. This is an important point when considering reaction induced surface absorptions that lead ultimately to laser induced damage.

As in previous studies, we observe that the IR absorption features become weaker if the samples are stored in dry air after exposure to atomic oxygen. Typically, the absorptions fade to 0.25 of their original strength after a period of 2 weeks.

Kinetics:

The kinetics are very complex. The lack of any precursor to ClO_3 such as ClO_2 or ClO indicates that the oxidation occurs in one step. This is possible via two processes:

$$O + O_2 \rightarrow O_3 \quad \text{----- (either on the wall, on the crystal, or with a 3rd body)} \quad (1)$$

$$O_3 + NaCl \rightarrow NaClO_3$$

or

$$O + O_2 + NaCl \rightarrow NaClO_3 \quad (2)$$

These two possibilities are not significantly different in (1). O_3 is formed (presumably on the surface) and then undergoes subsequent reaction with the crystal. In (2), O_3 is formed either on or beneath the surface by the recombination of atomic oxygen with O_2. Reaction then occurs quickly or even in the same step as the recombination. If (1) contributes significantly to the formation of ClO_3, then a stream of O_3 incident on the NaCl surface should result in chemical reaction. We have exposed NaCl surfaces to 1-2 % O_3 (in O_2) for periods up to 24 hours and observe no detectable IR absorptions. Thus, it is evident that atomic oxygen is required for reaction to take place.

Implications and Discussion:

Previous studies concerned with the reaction of oxygen with alkali halides have relied upon molecular oxygen at elevated temperatures [6]. This study is the first in which atomic oxygen is used as the reactive species. The obvious strong effect of atomic oxygen with NaCl is of technological as well as scientific interest and has a number of interesting implications. The relatively inert nature of KBr and KCl may only be an indication that XO_3 formation is restricted to the surface of the sample. This is a moot point when considering the damage characteristics of such a material since the surface will be readily damaged by laser radiation when XO_3 formation occurs. It will be useful to study in more detail the surface reaction in KBr and KCl using multiple internal reflection spectroscopy [5].

Finally, it cannot be overstated that this problem is a general one and will have to be reckoned with in many situations. For example, when air is used in place of O_2 in the discharge apparatus, large amounts of NO_3 formation are observed via the IR absorptions of NO_3.

References

1. C. F. Wittig, J. C. Hassler, P. D. Coleman, J. Chem. Phys. 55, 5523 (1971).
2. J. L. Hollenberg and D. A. Dows, Spectrochimica Acta 16, 1155 (1960).
3. G. N. Krynauw and C. J. H. Schutte, Spectrochimica Acta 21, 1947 (1965).
4. M. Beniere, F. Beniere, M. Chemla, Solid State Comm. 13, 1339 (1973).
5. H. G. Tompkins, Appl. Spectroscopy 28, 335 (1974).
6. L. W. Barr and A. B. Lidiard, Physical Chemistry, Vol. 10, p. 151, Academic Press, New York (1970).

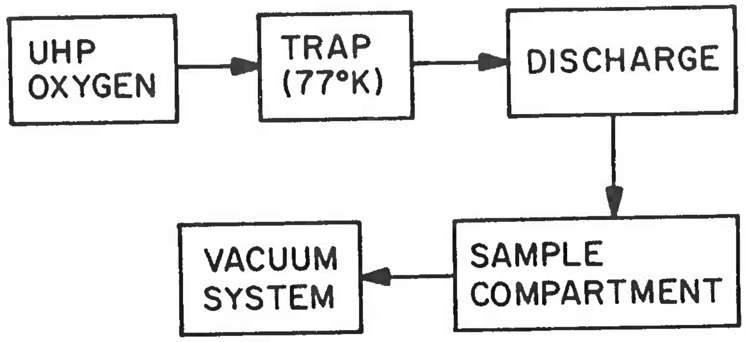

Figure 1. Schematic representation of experiment.

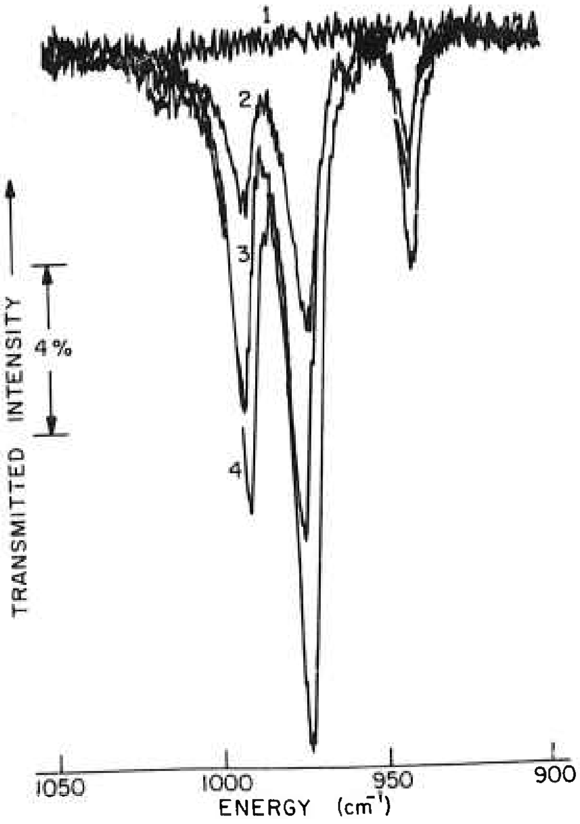

Figure 2. Spectrophotometer trace of NaCl after exposure to discharged oxygen. Curves 1, 2, 3, 4 represent 0, 3, 6 and 9 hour exposures respectively. The only other absorption features are near 600 cm^{-1} and therefore obscured by the intrinsic absorption.

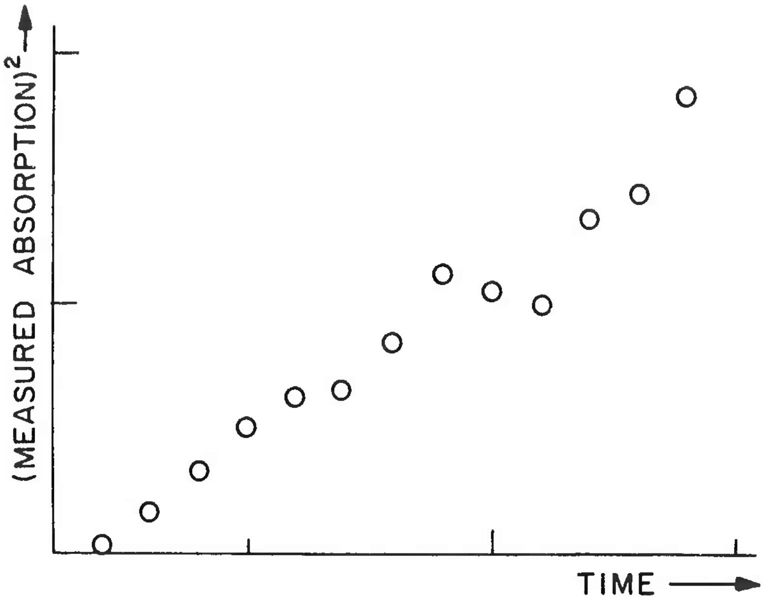

Figure 3. Data showing the $\sqrt{t}$ dependence of the measured absorption. The scales are in arbitrary units since meaningful diffusion coefficients cannot be obtained from the data.

Figure 4. Transmission of KBr and KCl after exposure to atomic oxygen. The curves are offset for convenience. There are no significant features at energies greater than 1200 cm^{-1}. Curve (A) is for KBr (13 hour exposure); curve (B) is for KCl (20 hour exposure).

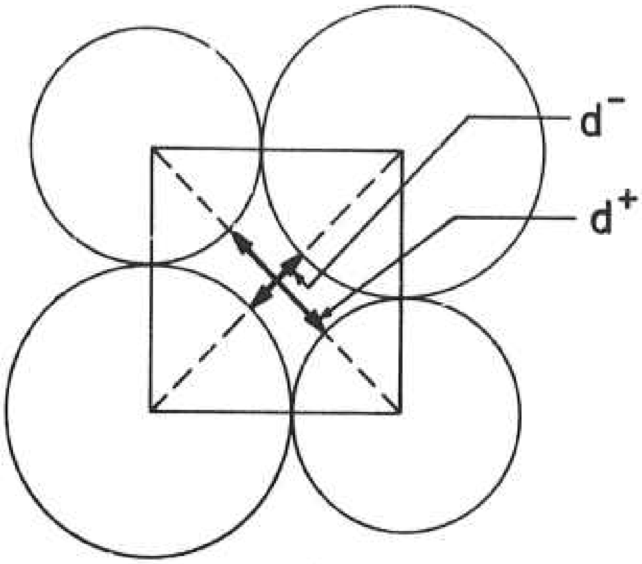

	d^+	d^-
NaCl	2.02 Å	0.36 Å
KCl	1.79	0.83
KBr	1.99	0.75

Figure 5. Two-dimensional representation of an alkali-halide crystal, showing dimensions of the interstitial region for the three cases of interest.

Pulsed 10.6μ Laser Damage Studies

M. Bass and K. M. Leung

The results of our laser damage study are summarized in the two attached papers. One was presented at the 1975 Laser Damage Symposium at Boulder, Colorado, and the other has been submitted to the *IEEE Journal of Quantum Electronics*.

The CdTe modulator necessary for the survival curve studies was delivered and tested. Due to timing circuitry problems, no results have been obtained. The manufacturer is attempting to correct the problem for us.

Damage to 10.6 μm Window Materials Due to CO_2 TEA Laser Pulses* ‡

K. M. Leung, M. Bass, and A. G. J. Balbin-Villaverde†

Center for Laser Studies
University of Southern California
Los Angeles, California 90007

Laser irradiation induced damage to several materials of interest for use as 10.6 μm laser system windows was studied. A pulsed CO_2 TEA laser, operating in the TEM_{00} mode was the irradiation source in these experiments. The light was focused onto the surfaces or into the bulk of the samples and the waveform of the transmitted pulse was monitored. Comparison of the incident and transmitted laser pulse waveforms shows the onset of laser induced damage as a distortion of the latter. Damage threshold data and a discussion of possible damage mechanisms for improved ZnSe, commercial and RAP grown KCl and commercial NaCl are presented.

Key words: KCl; NaCl, pulsed CO_2 TEA laser damage; transmitted pulse; waveform distortion; ZnSe.

1. Introduction

One of the commonly used diagnostic techniques for monitoring laser-induced damage is to examine the temporal shapes of laser pulses that are transmitted through transparent dielectrics. When damage occurs on sample surfaces or in bulk materials, the transmitted pulse is attenuated in amplitude as well as distorted in waveform. In recent years, Bass and Fradin [1][1] have demonstrated that when damage occurs, the transmitted ruby laser pulse is attenuated in a manner that is characteristic of the source of damage. They further showed that pulses which are attenuated very rapidly form damage regions in the bulk which are characteristic of the intrinsic mechanism such as an electron-avalanche breakdown. Other damaging pulses are attenuated in a very different manner and produce damage regions that appear to result from inclusion absorption. Last year at this symposium, Milam et al. [2] described a new experimental technique for determining the cause of laser-induced damage. The new procedure was based upon this statistical nature of the times required to produce damage at many sites which were irradiated by equally-intense, square-waveform pulses. This permits identification of the damage mechanisms without requiring a threshold measurement. In the ir region, Yablonovitch [3] observed similar statistical properties for damage due to CO_2 TEA laser pulses passing through alkali-halide crystals. However, the experimental observation was complicated by several longitudinal modes which contributed a time structure to the laser pulse.

At USC, a setup based on Milam's technique [2] to extract square-waveform pulses from the most intense portion of a CO_2 TEA laser pulse is under construction. This will make possible measurement of 10.6 μm survival curves in different ir materials. To date, however, we have employed the recent development of fast detection electronics to examine simultaneously both the transmitted and incident pulses of a CO_2 TEA laser. In this paper we describe the technique and discuss possible damage mechanisms for 10.6 μm window materials. The experimental results will be divided into

---

* This work was supported by Defense Advanced Research Projects Agency and was monitored by Air Force Cambridge Research Laboratories.

† Present address: Instituto de Fisica, Universidade Estadual de Campinas, Campinas, S. P., Brazil

[1] Figures in brackets indicate the literature references at the end of this paper.

‡ Presented at the 1975 Laser Damage Symposium, Boulder, Colorado, July 1975. To be published in the Proceedings of that conference.

two sections, one based on the transmitted pulse waveform analysis and the other on threshold measurements for surface and bulk damage on ten samples of three different ir window materials. Some damage morphology on typical samples will be discussed.

2. Experimental

The experimental setup for conducting pulsed CO_2 damage experiments is shown in figure 1. The basic apparatus consists of a pulsed CO_2 TEA laser, a beam attenuator, a test vacuum chamber, and an energy/waveform monitoring system. Three measurements are provided by using this setup: the incident energy at the sample, the spatial profile of the laser beam, and the waveforms of the incident and transmitted pulses. Details of individual components as well as test procedure are discussed below.

2.1 CO_2 TEA Laser Pulses

The performance and characteristics of the CO_2 TEA laser used in this work are described in table 1.

Table 1. CO_2 TEA laser parameters and performance data

Discharge length (double Rogowski electrodes)	41 cm
Energy storage capacitance	0.08 μf
Flow rate ratio ($He:N_2:CO_2$)	8.7:2.4:2.6 ℓ/min
Mirrors:	100%R - Flat/Si
	80%R - 10 meter/Ge
Brewster windows	KCl
Intracavity aperture diameter for TEM_{00} mode	6 to 9 mm
Cavity length	120 cm
Typical input energy	21 J
Typical output energy (9 mm aperture) for TEM_{00} mode	100 mJ
Typical width for gain-switched pulse (FWHM)	92 ns

The spatial profile of the laser beam was measured by a pinhole scan detector. Figure 2 shows that the beam profile was a Gaussian distribution. When a 9 mm intracavity aperture was placed 15 cm from the flat 100% reflecting mirror, the spot-size ($1/e^2$ radius of the intensity profile) at the focusing lens was measured to be 2.9 mm and 2.4 mm for a 6 mm intracavity aperture. The output pulse of the laser consisted of a 92 nsec gain-switched pulse followed by a long tail of ~1.6 μsec duration. Several longitudinal modes were able to oscillate and so the pulse waveform showed structure similar to that observed by Yablonovitch [3]. The self-locked output waveform was caused by the fact that the absorption of CO_2 molecules in the lasing medium can saturate [4]. The mode-locked waveform was composed of pulses having < 2.5 nsec duration and separated by 8 nsec, the cavity round-trip time. The fraction of the total energy in the gain-switched pulse was determined by measuring the areas under the gain-switched pulse and the long tail. These areas were equal, showing that half the total energy was in the gain-switched pulse. The total incident energy was measured with a thermopile (Hadron Model 100) calorimeter having an accuracy of ± 5%.

2.2 Experimental Procedures

The energy of the laser beam incident on the sample was selected by a beam attenuator consisting of Brewster angle ZnSe polarizers which provide extinction ratio of 1:16. A discussion of this device is given in Appendix A. Each laser shot was either focused onto the surface or into the bulk of a test specimen using a 3.8 cm focal length AR coated Ge lens. The focal position was determined by varying the lens to sample separation and observing burn spots on a piece of black photographic film (unexposed Poloroid Type 410) attached to the surface of the sample. The focal spot-size of the Gaussian mode beam w_0 was calculated by the following equation

$$2w_0 = \frac{4\lambda}{\pi} \times \frac{f.l.}{2w}$$

where w is the measured laser spot size on the focusing lens. The calculated w_0 was in excellent agreement with the measured radius of many surface damage sites on ZnSe. All samples were studied in a plexiglas chamber evacuated by a mechanical pump to eliminate spurious breakdown due to dust or gas molecules near the surface of a sample. Onset of damage was monitored by (1) observing the visible plasma and changing appearance of the sample from the focal region, (2) examining the damaged region under the microscope, and (3) comparison of the incident and transmitted laser pulse waveforms. In this work, the waveform diagnostic technique was emphasized and found to be useful in understanding the damage process. A ZnSe beamsplitter located in front of the beam attenuator was used to direct a portion of the incident beam onto a photon drag detector (PD 1). The transmitted beam was re-collimated by a ZnSe lens and monitored by another photon drag detector (PD 2). Both detectors have similar response and rise time of 500 ps. Signals corresponding to incident and transmitted pulses were simultaneously displayed on upper and lower traces of a high-speed (400 MHz) dual-beam oscilloscope (Tektronix Model 7844), respectively. Typical traces are shown in upper corner of figure 3. For convenience, the transmitted pulse waveform was inverted and when no damage was produced the waveforms were registered with respect to each other in time. For this work, only single shot on single site testing is reported.[2]

3. Waveforms Analysis and Possible Damage Mechanisms

3.1 Comparison of Incident and Transmitted Pulses

Since the high-speed detector dual-beam scope combination can provide a time resolution of 2.5 nsec, it is possible to examine waveform distortion on this time scale and to measure the survival time of each damage site. For this reason, the analysis is based upon the comparison of incident and transmitted mode-locked pulses in the gain-switched pulse when no damage occurs during the experiment. There are typically 23 mode-locked pulses in a recorded signal. The transmission of individual mode-locked pulses is normalized to that at t = 0. The normalized transmission of the i^{th} pulse is defined as

$$T_i \equiv \frac{\mathcal{I}_i(t = t_i)}{\mathcal{I}_0} \quad \text{for } i = 0, 1, 2, \ldots$$

and

$$\mathcal{I}_i \equiv \frac{I_{out}\ (t_i)}{I_{in}\ (t_i)}$$

where I_{in} and I_{out} are the amplitudes of individual mode-locked pulses at time $t = t_i$. For illustration, the normalized transmission of a pulse which did not cause damage is plotted against time in figure 3. The solid line gives a good indication that no distortion of the transmitted waveform occurred (all T_i are very close to unity). The dashed curve shown on the same plot gives the normalized waveform of the gain-switched pulse. In general, waveform distortion was studied over a range of incident laser power from below threshold to 4 times threshold.

Since laser induced gas breakdown is thought to be caused by electron avalanche breakdown, we have examined the waveform distortion due to air breakdown pulses at 22 cm Hg pressure. The transmitted waveform distortion is depicted in figure 4. It is easy to see that air is completely broken down within one pulse at t_d = 72 nsec. We shall refer to the time when damage occurs, t_d, as the survival time.

3.2 Surface Damage on IR Window Materials

---

[2] For pulsed laser damage experiments, three types of threshold measurement have been practiced by different workers. They are single shot on single site (one to one), multiple shots with variable incident intensity on single site (n to 1) and multiple shots with constant incident intensity on single site ($\bar{n}$ on 1).

Seven surfaces of three ir window materials (ZnSe, KCl, and NaCl) were studied in these laser damage experiments. The waveform distortions for surface damage on NaCl, KCl, and ZnSe as well as air breakdown are shown in figure 5. To show the distortion more clearly three transmission curves are plotted in figure 6 for surface damage on three ir window materials at threshold. All samples survived until ~ 50 nsec and the complete attenuation took place within one to two pulses except for KCl. If the incident power was raised above threshold, the survival time was reduced and transmission cut-off occurred in the second or third mode-locked pulse. A blue-white plasma was observed at or above threshold in all cases. The waveform distortion analysis for surface damage suggests that the damage mechanism is very similar to air breakdown.

3.3 Bulk Damage in IR Window Materials

Typical traces for bulk damage in NaCl, KCl, and ZnSe both at threshold and above threshold are shown in figure 7. For commercially fabricated NaCl, sharp cutoff at threshold as well as above threshold were characteristics of the transmitted pulse waveform distortion. In general, both ZnSe and KCl show very slow attenuation. For ZnSe, this slow cutoff was expected since inclusion absorption is the dominant cause of material failure. However, in the case of RAP grown KCl and commercial KCl, the observed slow cutoff suggests that very small inclusions in the bulk still play a dominant role in the damage process. In all cases, if no spark was observed for a particular site, waveform distortion could not be detected either. The spark in NaCl was yellow as expected for a sodium spark. Bulk damage in ZnSe was always accompanied by a yellow spark inside the medium. The observed color of this spark is due to the fact that it is surrounded by a medium which absorbs the blue and green parts of the spectrum.

For a more detailed view of damaging waveform distortion figures 8, 9, and 10 display transmission curves for NaCl, KCl, and ZnSe respectively. The results of waveform distortion analysis for bulk damage in these materials is summarized in table 2. In addition, figure 11 gives the transmission versus gain-switched pulse energy for the case of bulk damage in commercial NaCl, RAP grown KCl, and old ZnSe as well as air breakdown. It implies that damage in these ir materials occurs when nearly half the energy contained in the gain-switched pulse has passed or just after the peak of the pulse.

Table 2. Bulk damage characteristics in ir window materials due to CO_2 TEA laser pulses

IR Materials	Color of Spark Formation	Condition of Site Fracture	Survival Time t_d at threshold	Time for Attenuation to Reach its Maximum	Possible Damage Mechanism
NaCl (commercial)	yellow	severe and large	56 nsec	50 nsec	intrinsic breakdown
KCl (commercial)	blue-pink	small	24 nsec	136 nsec	inclusion absorption
KCl (RAP)	"	"	80 nsec	>100 nsec	" "
ZnSe (Raytheon 1974)	yellow	small and in the bulk	56 nsec	30 nsec	inclusion absorption
ZnSe (Raytheon 1975)	"	"	40 nsec	>100 nsec	" "

4. Measured Damage Threshold in IR Window Materials

Table 3 summarizes our measurements of surface and bulk damage thresholds in three ir window materials - ZnSe, KCl, and NaCl. In this paper, we report the axial peak power density P_0 (MW/cm^2) which is defined

$$P_0 = 2\times P_{Ave} = 2\left(\frac{4\ln 2}{\pi}\right)^{\frac{1}{2}} \frac{E_{total}}{\Delta\tau} .$$

Here $\Delta\tau$ is the FWHM for the gain-switched pulse of the CO_2 TEA laser. E_{total} is the net energy density in J/cm^2 deposited at the focal region of the sample during the gain-switched pulse. We emphasize again that the test results are reported for a single shot on a single site in contrast to other reports [5]. The damage threshold is defined as the lowest power density which damages 50% of the sites studied. The numbers in parenthesis in table 3 are the power densities which cause damage to 10% of the sites.

Table 3. Measured damage threshold on ir window materials due to CO_2 TEA laser pulses

Sample Material	Absorption[a] $\alpha_{total}(cm^{-1})$	Surface Finishing Method	Axial Peak Power Density P_0 (MW/cm^2)	
			On Surface	In Bulk
ZnSe (Raytheon 1974)	0.005	conventional	270	230
ZnSe (Raytheon 1975)	0.0005	diamond-polished	350 (270)	460 (350)
ZnSe (Raytheon 1975)	0.0005	super-polished	350 (270)	460 (350)
KCl (HRL-RAP)	0.00014	conventional	460 (350)	4600
KCl (HRL-RAP)	0.00026	- -	- -	1500 (760)
KCl (Harshaw Econoflat)	0.001	conventional	560 (165)	650 (150)
KCl (Harshaw)	0.0008	- -	- -	< 190
KCl (Harshaw Comm.)	0.0023	- -	- -	< 190
NaCl (Harshaw Econoflat)	0.004	conventional	1600 (1200)	6100 (5600)
NaCl (Harshaw Spectro.)	0.004	conventional	840	3900

[a] Values are provided by respective suppliers to be considered for reference only.

4.1 Damage in ZnSe

We have performed 10.6 μm damage experiments on three different surfaces of ZnSe crystals and in two different bulk materials. Raytheon Company furnished samples of its 1974 ZnSe material and its improved 1975 ZnSe. It should be noted that the improved ZnSe has much lower absorption than the 1974 material.

As seen in table 3, no significant difference was found in damage threshold for different surface finishing methods. Figure 12 shows the super-polished and diamond-polished surfaces obtained on improved ZnSe crystals for these experiments. The conventional surface on an old ZnSe crystal appeared to be very similar to the diamond-polished surface.

We have also investigated both visible and 10.6 μm scattering using the Optical Functional Tester at NWC described last year [6]. Bulk scattering was dominant in both old and improved ZnSe suggesting that inclusions in ZnSe may still be the major determinant of the 10.6 μm damage threshold. However, the improved ZnSe was the first sample of this material which could be damaged on the surface and not in the bulk. The morphology of the damage sites in ZnSe (see figure 13) further supports the fact that inclusions near the surface or inside the bulk play an important role in the damage mechanism.

4.2 Damage in KCl and NaCl

Since conventionally polished KCl surfaces are easily contaminated even under normal laboratory environments, only two surfaces were used for the experiment. Our interests in alkali halides are in understanding the damage mechanism but not in the threshold comparison. Therefore, one should not be too serious about the comparison between KCl and NaCl listed in table 3. In general, conventionally grown NaCl crystals still have higher threshold values. The RAP grown KCl crystals are superior to conventionally grown KCl by an order of magnitude in damage threshold. Damage morphology on these crystal surfaces is quite similar and in general the damage site is larger than the laser beam cross section. Figures 14 and 15 show such morphology for KCl and NaCl surfaces. In bulk damage, NaCl shows larger fracture along cleavage planes than KCl.

5. Summary and Conclusions

With a high-speed detector/dual-beam oscilloscope detection system we have begun to observe the dynamics of 10.6 μm laser induced damage in ir window materials. Comparison of the incident and transmitted laser pulse waveforms shows the onset of laser induced damage as a distortion of the latter. Survival time of surface and bulk damage for different materials can be accurately determined using this technique.

With the samples confined in an evacuated chamber, surface damage of NaCl, KCl, and ZnSe was similar to air breakdown, showing a sharp cutoff in the transmitted pulse waveform. Surface contaminants may cause early breakdown and generate a plasma similar to that in a gas breakdown. For bulk damage in old and improved ZnSe, the distortion of the transmitted pulse waveform.suggests that two different kinds of inclusions are involved in the damage process. Measured threshold values of these ZnSe samples suggested that the improved material is indeed out-performing the old one. Damaging pulse waveform distortion for HRL RAP grown KCl is very slow and suggests that inclusions still play an important role in limiting the damage resistance of this material. The waveform distortion observed for Harshaw NaCl is fast and resembles that due to intrinsic breakdown. Measured threshold values of these alkali halides suggest that the breakdown field of NaCl may be greater than that of KCl in contrast to the result of "n on 1" experiments reported last year [7]. This conclusion, however, depends upon which samples are compared and so reports of relative breakdown fields must be cautiously evaluated.

In conclusion, we feel that the current results still do not provide a quantitative understanding of damage to 10.6 μm window materials due to CO_2 TEA laser pulses. A better statistical technique [2] will be applied at this wavelength in the coming year.

We further conclude that since different damage threshold values for a given material can be easily found in the literature, it is essential to exchange test specimens or work jointly on a particular experiment using different diagnostic techniques and equipment. To this end, USC and HRL have initiated a joint experiment to perform damage measurements on RAP grown KCl crystals and other samples.

6. Acknowledgements

The authors are grateful to Raytheon Company for providing the ZnSe samples, Hughes Research Lab. at Malibu, CA, for the RAP grown KCl samples, Mr. Walter Spawr for his effort in polishing ZnSe for this work. The authors also thank many individuals at NWC, China Lake, CA, for their technical assistance in scattering experiments and Nomarski microscopy.

At the University of Southern California, we thank C. C. Tang and M. Chang for their assistance in data acquisition. Professor J. Ward who has provided many fruitful discussions is especially acknowledged.

7. Appendix A. 10.6 μm Attenuator

For laser-induced damage experiments, it is desirable to have a variable attenuator which will control the incident laser energy continuously without affecting the duration, the polarization and the spatial distribution of the laser pulse. In the visible and near ir region, the combination of one rotatable and one fixed Glan polarizer was used as a variable attenuator [8]. For 10.6 μm radiation, a pair of wire-grid polarizers on ZnSe substrates can provide two orders of magnitude attenuation [7]. However, these polarizers are very costly and are limited by low resistance to laser damage. In this work, we have prepared two relatively inexpensive ZnSe reflection polarizers as a beam attenuator. A detailed discussion of how this attenuator works is presented below.

It is well known that when a plane wave is incident upon a dielectric surface, the reflection coefficients can be described by Fresnel's equations. Let φ be the angle of incidence, r the angle of refraction, and n the refractive index. Then the reflection coefficient for linearly polarized incident light with electric vibration perpendicular and parallel to the plane of incidence can be expressed as,

$$R_{\perp} = \frac{\sin^2(\varphi - r)}{\sin^2(\varphi + r)} \quad \text{and } R_{\parallel} = \frac{\tan^2(\varphi - r)}{\tan^2(\varphi + r)}$$

respectively. If the angle of incidence is Brewster's angle, $\varphi = \arctan(n)$ and $R_{\parallel}$ is zero. For ZnSe, $\varphi_B = \arctan(2.40)$ at 10.6 μm and $R_{\perp} = \frac{1}{2}$.

A typical arrangement of reflection polarizers employs two oppositely sloping sets of plates mounted at Brewster's angle. Let the fixed polarizer be oriented to transmit the laser polarization and $\theta = 0^{\circ}$ be the angle of the rotating polarizer giving the maximum transmission through the combination attenuator. Then the transmitted laser intensity, I_{out}, at any rotation angle θ about the beam axis can be determined by means of Jones calculas as follows:

$$\begin{pmatrix} E_H \\ E_V \end{pmatrix} = \begin{pmatrix} 1 & 0 \\ 0 & p \end{pmatrix}^{\beta} \begin{pmatrix} \cos\theta & -\sin\theta \\ \sin\theta & \cos\theta \end{pmatrix} \begin{pmatrix} 1 & 0 \\ 0 & p \end{pmatrix}^{\alpha} \begin{pmatrix} \cos\theta & \sin\theta \\ -\sin\theta & \cos\theta \end{pmatrix} \begin{pmatrix} 1 \\ 0 \end{pmatrix} = \begin{pmatrix} \cos^2\theta + \sin^2\theta p^{\alpha} \\ \cos\theta \sin\theta (1 - p^{\alpha}) p^{\beta} \end{pmatrix}$$

and

$$I_{out} = I_{in} \left\{ (\cos^2\theta + \sin^2\theta p^{\alpha})^2 + [\cos\theta \sin\theta (1 - p^{\alpha}) p^{\beta}]^2 \right\}.$$

Here, p is related to the principal transmittance: $T_{\perp} = 1 - R_{\perp} = p^2$. α is the number of ZnSe surfaces in the rotatable polarizer and β the number in the fixed polarizer. For our case, $p^2 = \frac{1}{2}$, $\alpha = 4$, $\beta = 2$ and the normalized transmitted laser intensity is

$$\frac{I_{out}(\theta)}{I_{in}} = \left\{ \cos^4\theta + \frac{1}{16} \sin^4\theta + \frac{41}{64} \cos^2\theta \sin^2\theta \right\}.$$

This expression agrees with the measured calibration intensity as a function of rotation angle about the beam axis. The extinction ratio of our attenuator is 1:16.

One final remark on the design of this attenuator is to avoid the use of plates with parallel faces. A scheme proposed by Bird and Schurcliff [9] can be considered by readers for obtaining better performance polarizers. They employed two oppositely sloping groups of plates that were each slightly wedged by angle about 1°. In addition, each group of plates was also "fanned" slightly. As a result, no reflected rays would follow the optical path of the main transmitted beam and produce unwanted interferences.

8. References

[1] Bass, M. and Fradin, D. W., IEEE J. Quantum Electron. QE-9, 890 (1973).

[2] Milam, D., Bradbury, R. A., Picard, R. H., and Bass, M., in Proc. 6th ONR/ASTM/NBS Symposium on Laser Induced Damage in Optical Materials: 1974, NBS Special Pub. 414, 169 (1974).

[3] Yablonovitch, E., Appl. Phys. Lett. 19, 495 (1971).

[4] Gilbert, J. and Lachambre, J. L., Appl. Phys. Lett. 17, 187 (1971).

[5] For example, see Wang, V. and Giuliano, C. R., "Measurements of Damage at 10.6 μm in Three Alkali Halides over a Range of Pulse Durations," this Proceedings.

[6] Soileau, M. J. and Bennett, H. E., in Proc. 6th ONR/ASTM/NBS Symposium on Laser Induced Damage in Optical Materials: 1974, NBS Special Pub. 414, 149 (1974).

[7] Allen, S. D., Braunstein, M., Giuliano, C., and Wang, V., in Proc. 6th ONR/ASTM/NBS Symposium on Laser Induced Damage in Optical Materials: 1974, NBS Special Pub. 414, 66 (1974).

[8] Bass, M. and Barrett, H. H., IEEE J. Quantum Electron. QE-8, 338 (1971).

[9] Bird, G. R. and Shurcliff, W. A., J. Opt. Soc. Am. 49, 235 (1959).

9. Figures

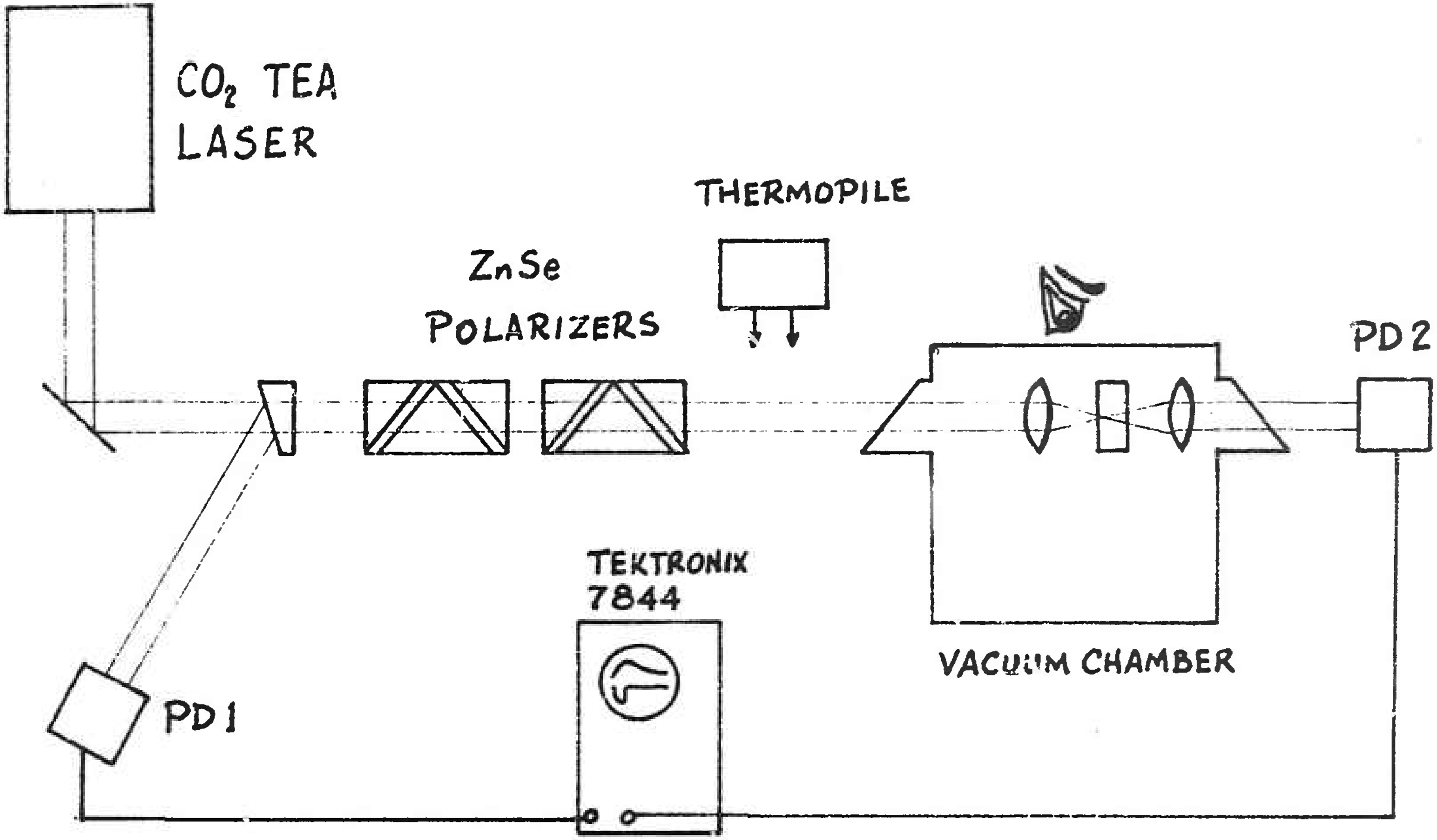

Figure 1. Schematic of the damage experiment. Both PD 1 and PD 2 are Ge photon drag detectors for monitoring the incident and transmitted pulses.

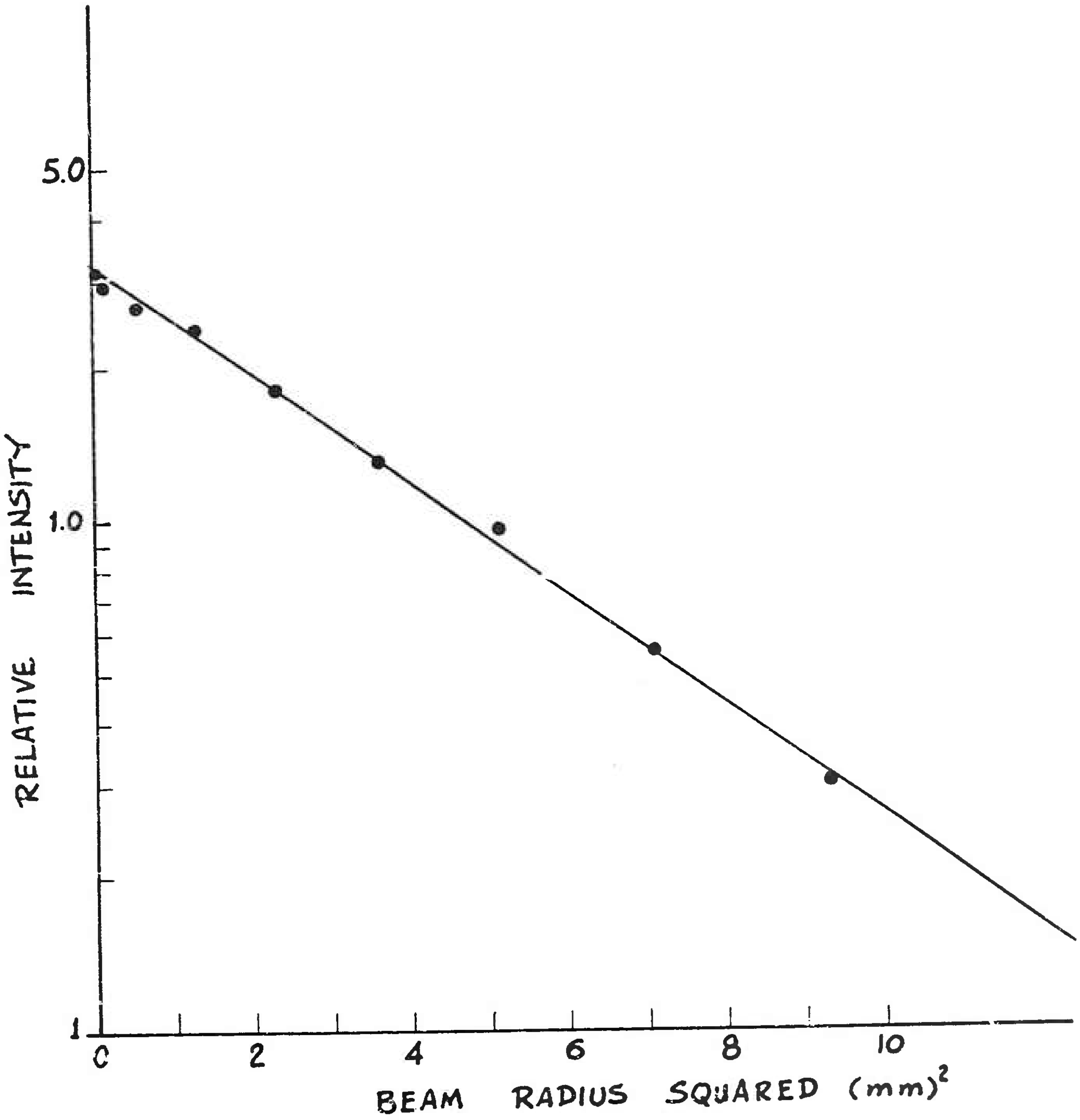

Figure 2. Pinhole scan of the CO_2 TEA laser beam.

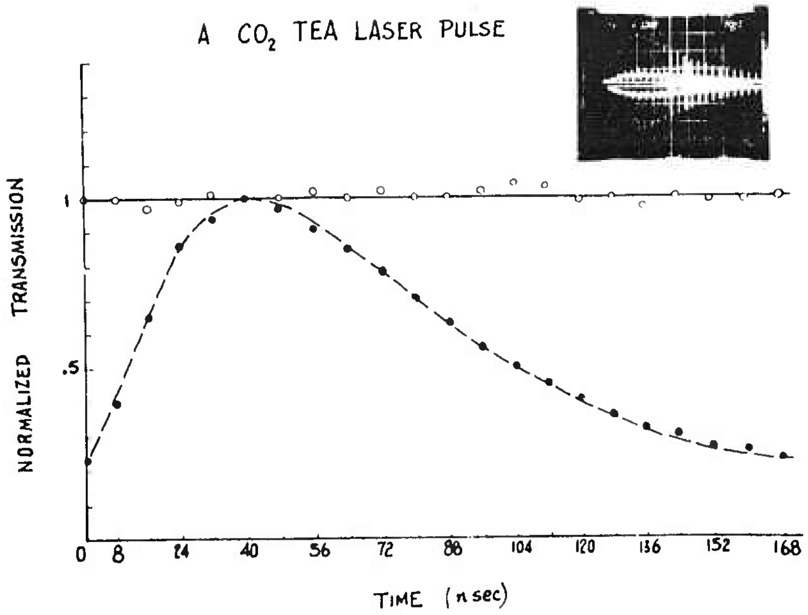

Figure 3. Transmission curve for a CO_2 TEA laser pulse. Dashed curve represents the laser pulse. $\Delta\tau$ is 92 nsec.

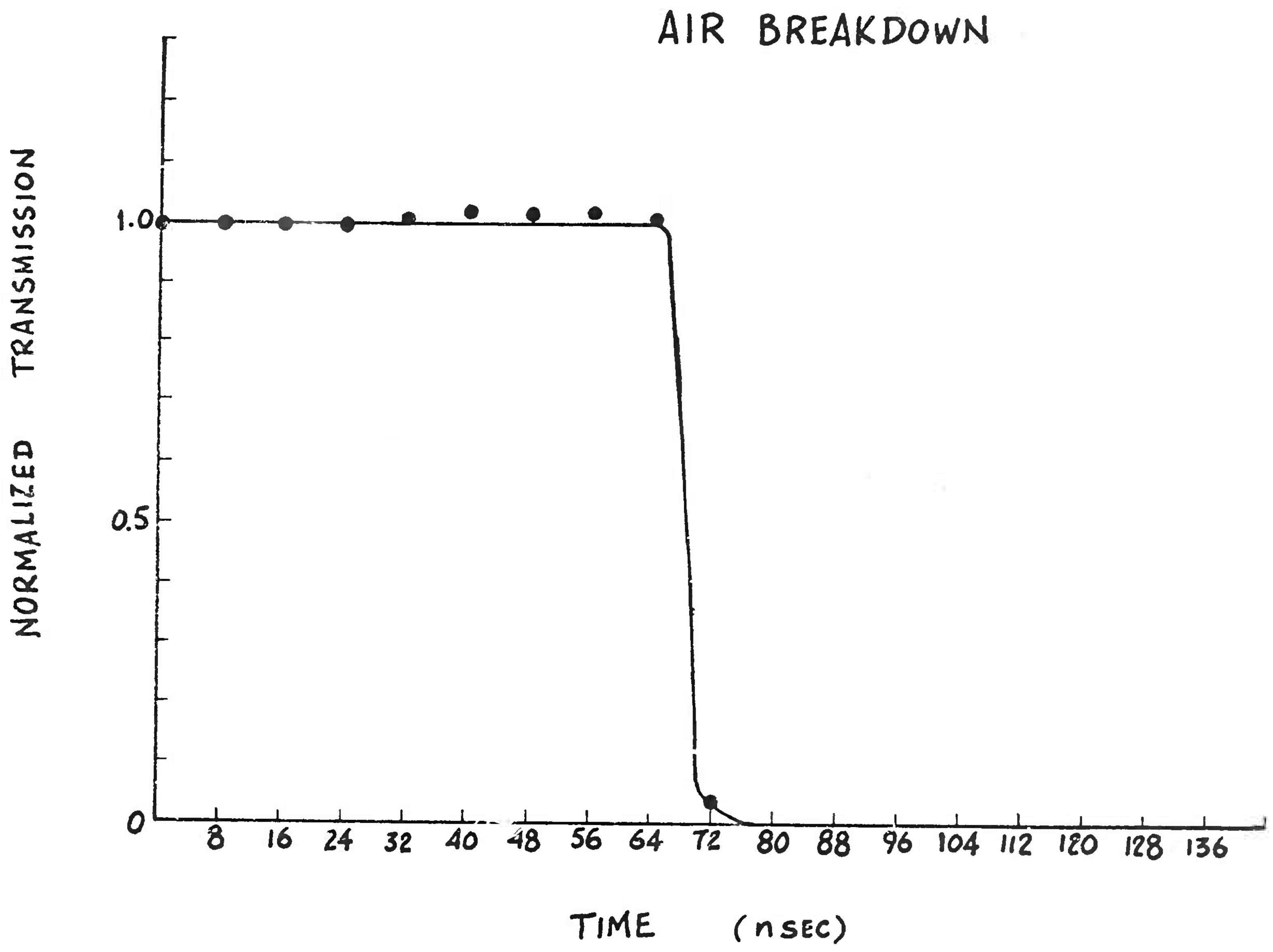

Figure 4. Transmission as a function of time for air breakdown.

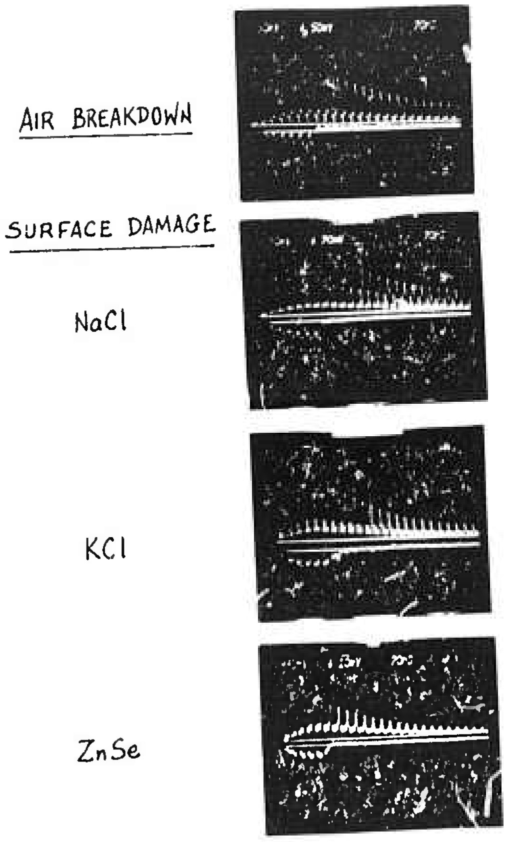

Figure 5. Typical oscilloscope traces for air breakdown and surface damage on NaCl, KCl and ZnSe. The upper beam is the incident pulse and the lower beam is the transmitted pulse.

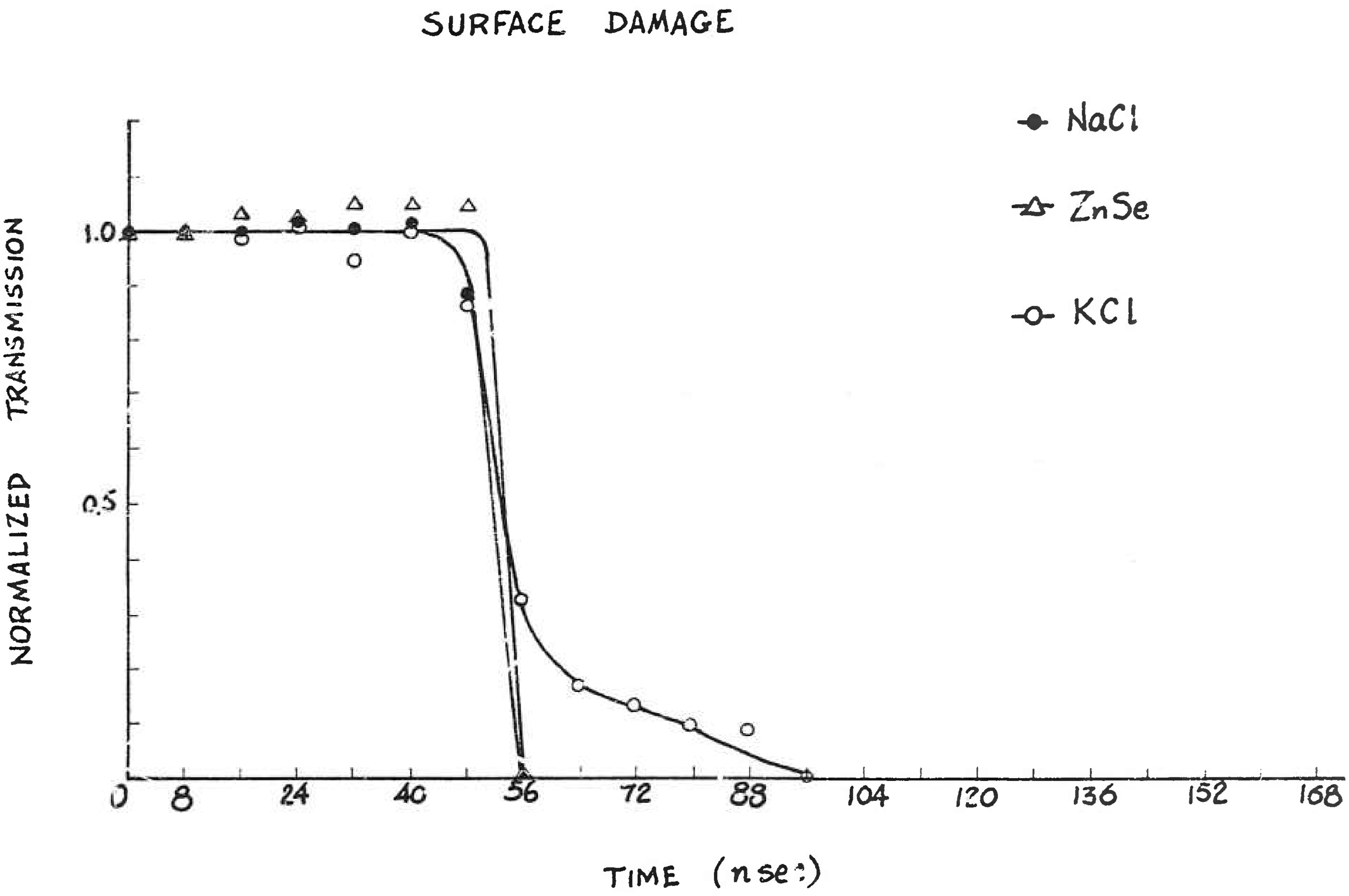

Figure 6. Transmission of mode-locked pulses as a function of time for surface damage on NaCl, KCl and ZnSe.

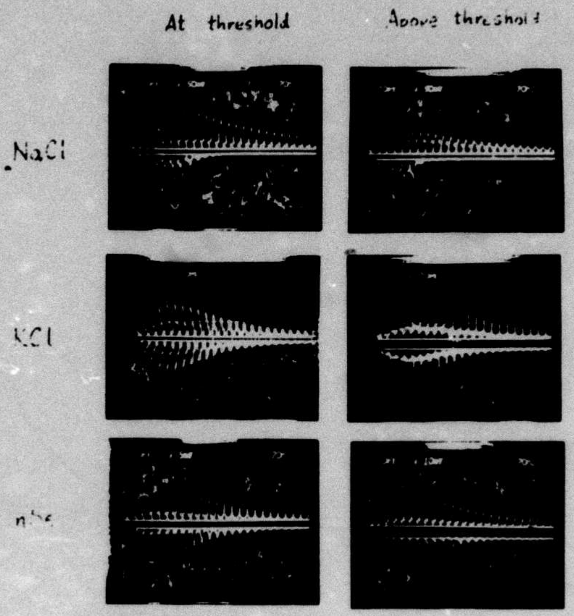

Figure 7. Typical waveforms for bulk damage in NaCl, KCl, and ZnSe at damage threshold and above threshold.

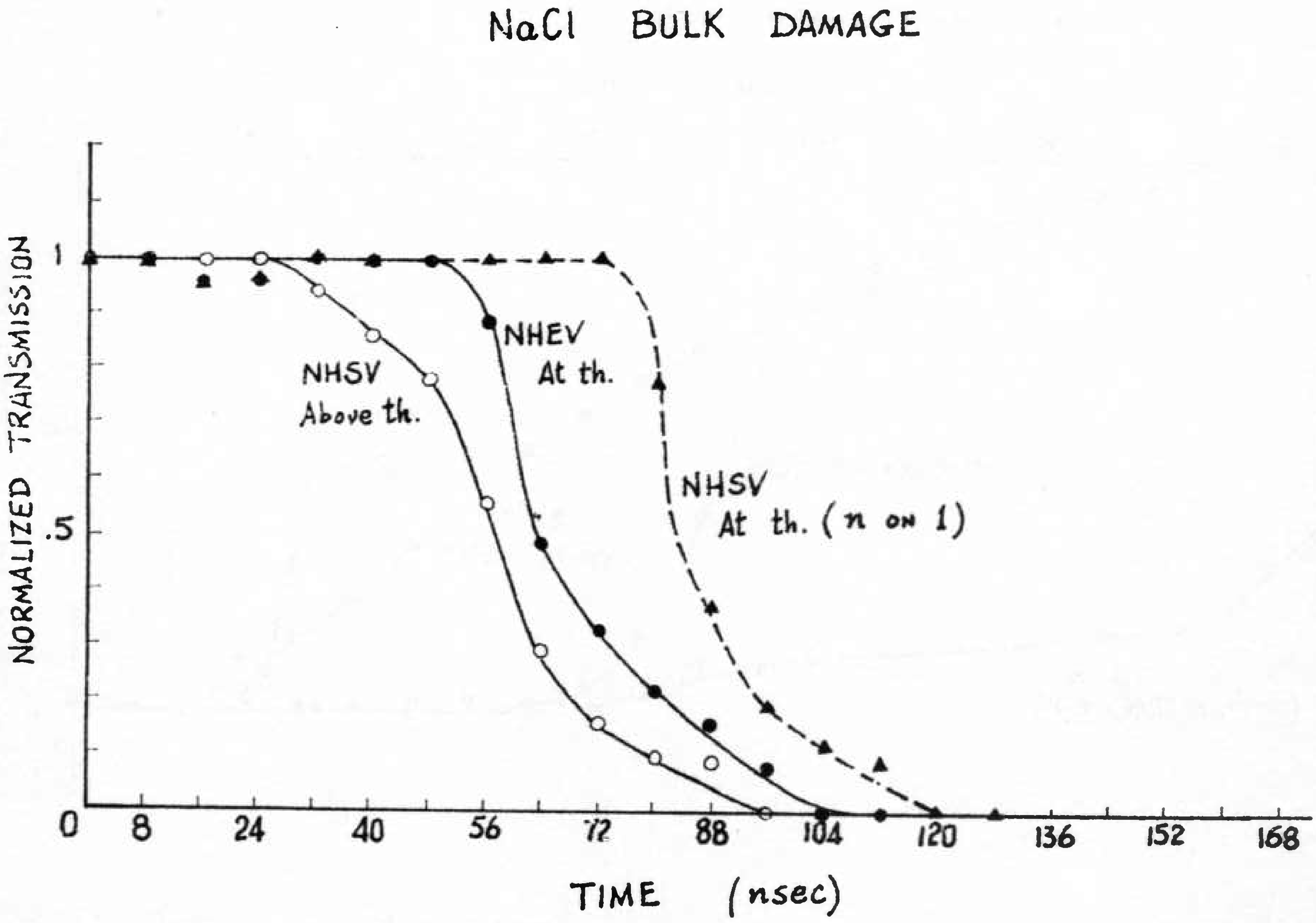

Figure 8. Normalized transmission of CO_2 TEA laser pulse as a function of survival time for NaCl bulk damage.

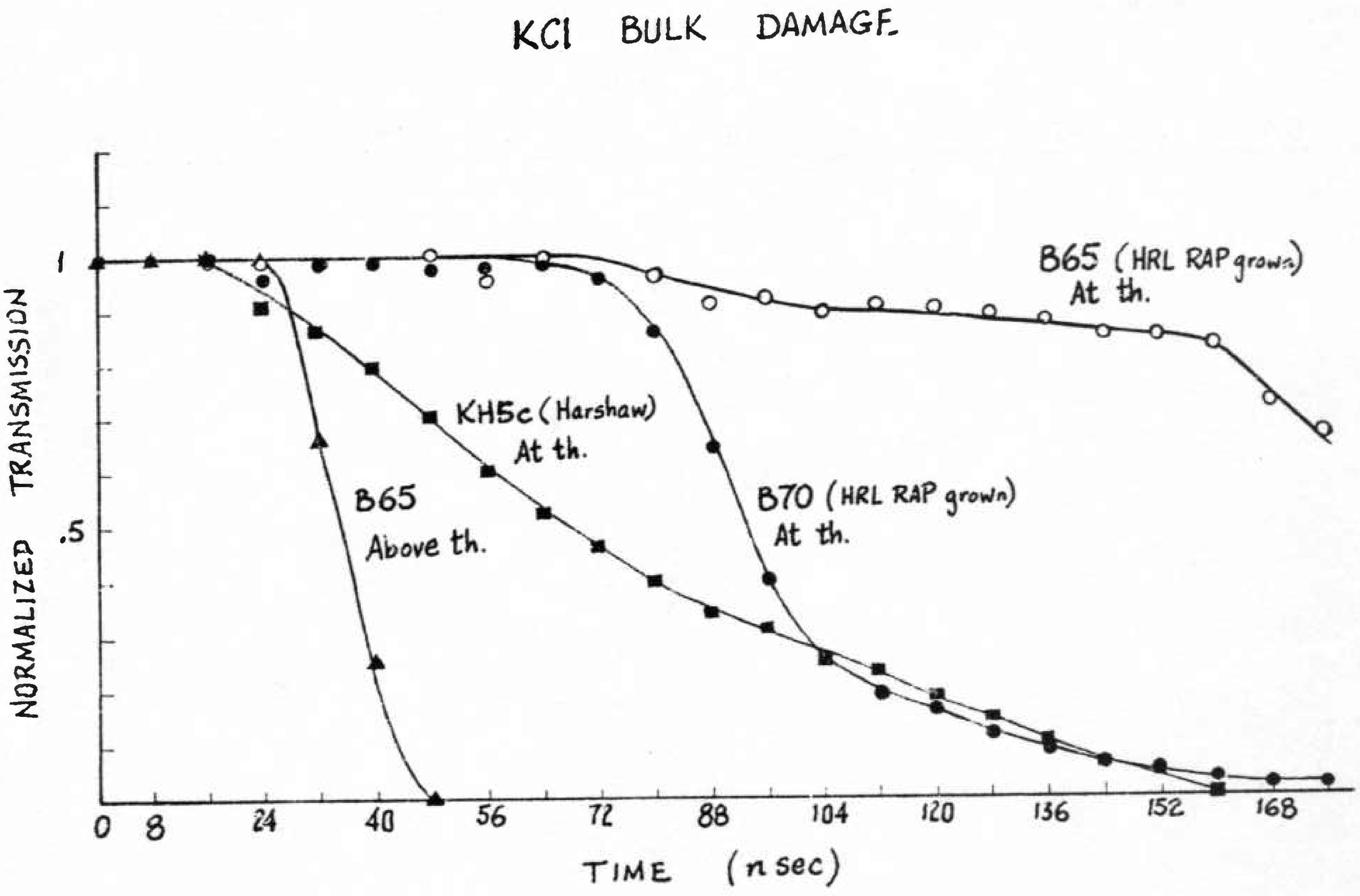

Figure 9. Normalized transmission of CO_2 TEA laser pulses as a function of survival time for KCl bulk damage.

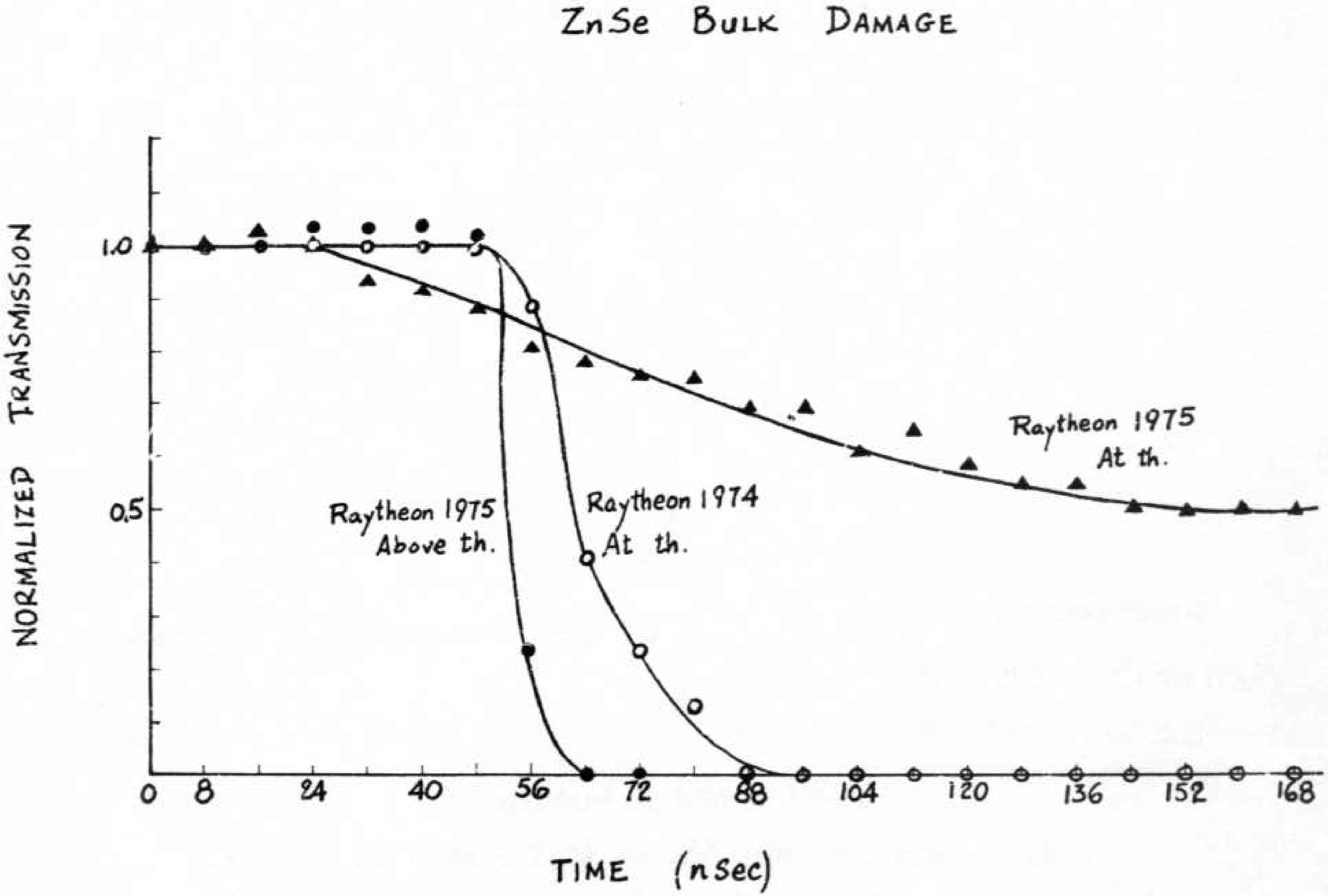

Figure 10. Normalized transmission of CO_2 TEA laser pulses as a function of survival time for ZnSe bulk damage.

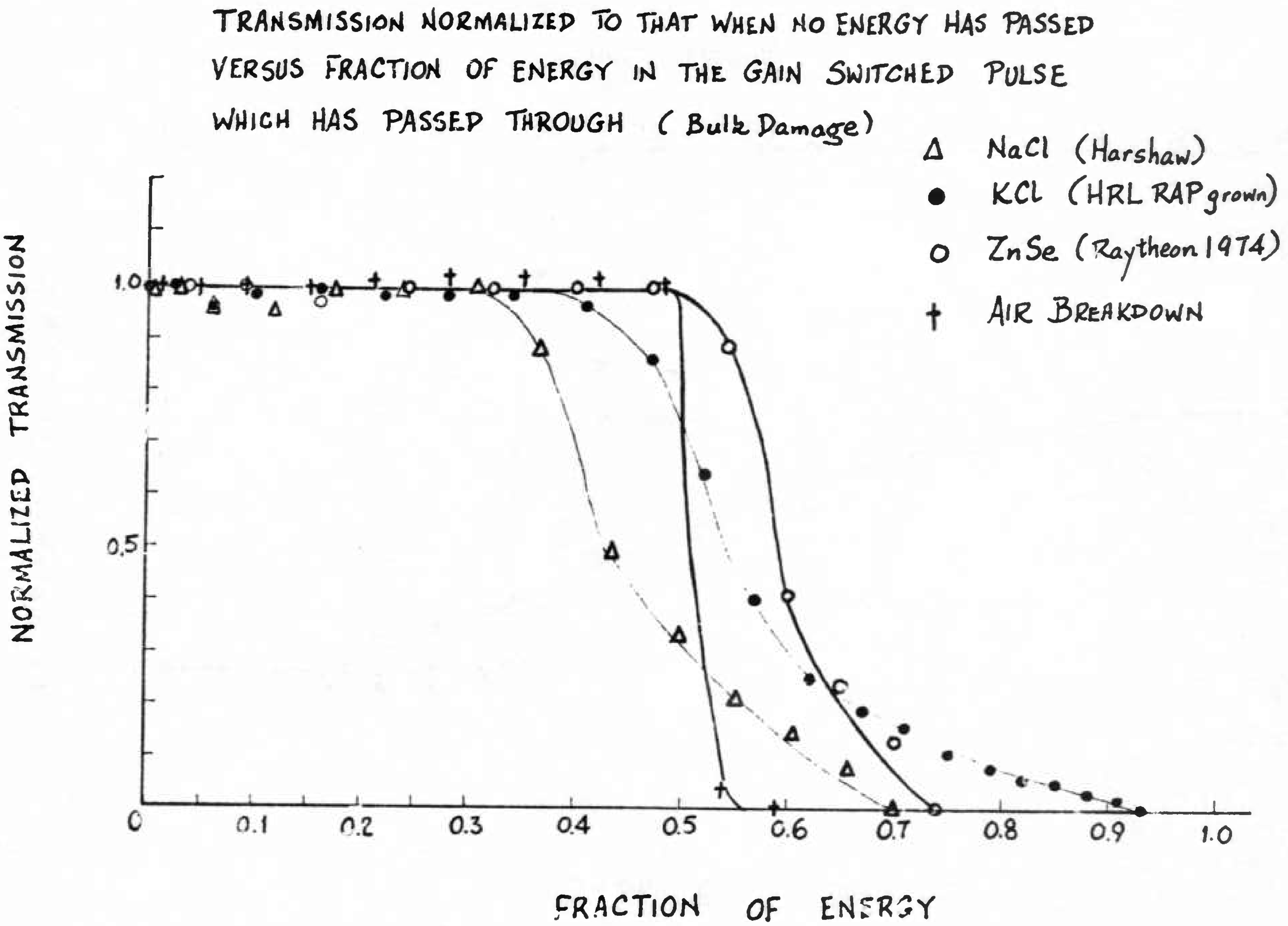

Figure 11. Normalized transmission versus fraction of energy contained in the gain-switched pulse for air breakdown, and bulk damage in NaCl, KCl, ZnSe.

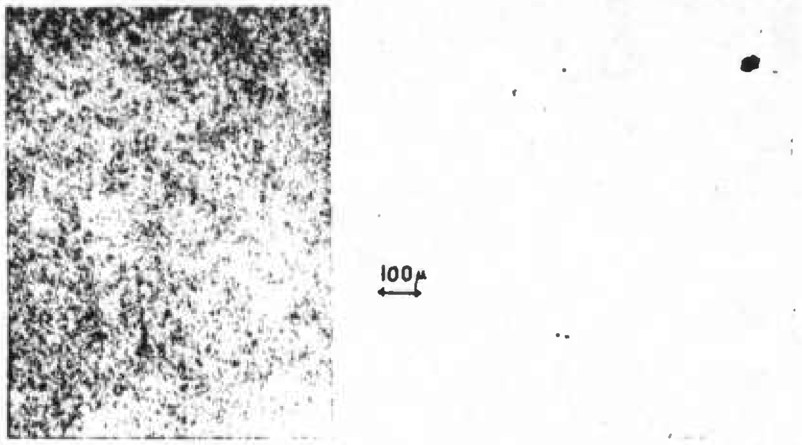

SPAWR SUPER-POLISHING RAYTHEON DIAMOND-POLISHING

Figure 12. Nomarski micrograph of surfaces on improved ZnSe prepared by both super-polishing and diamond-polishing. The spots on the diamond-polished surface are probably due to inadequate cleaning of the protective Opticoat coating.

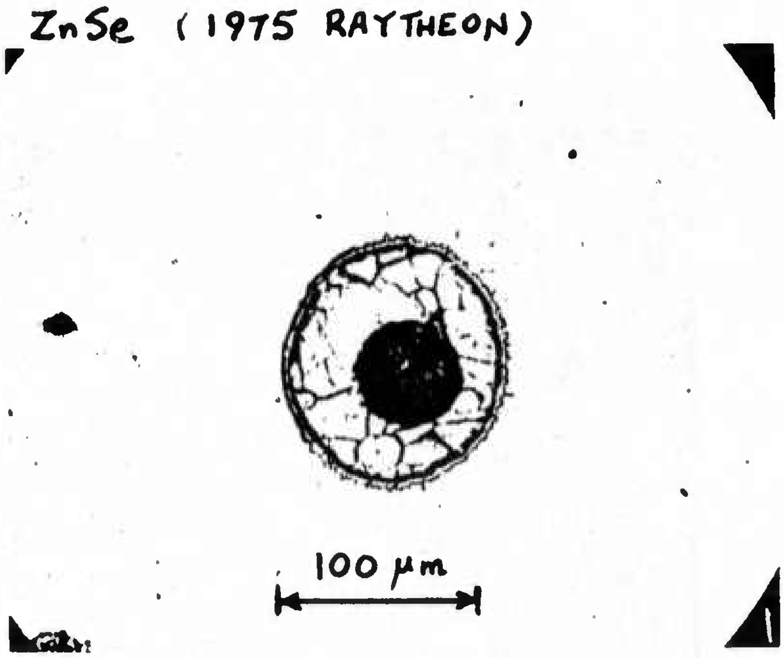

Figure 13. Damage site at threshold on a super-polishing surface of 1975 ZnSe observed with an optical microscope.

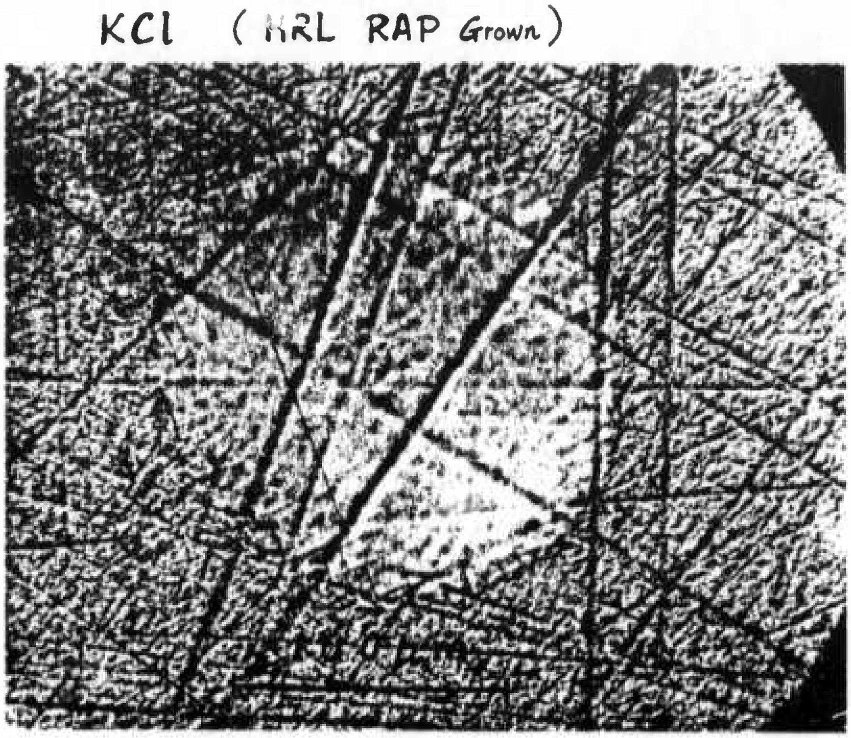

Figure 14. Nomarski micrograph showing a damage site on surface of RAP grown KCL (B70) at threshold.

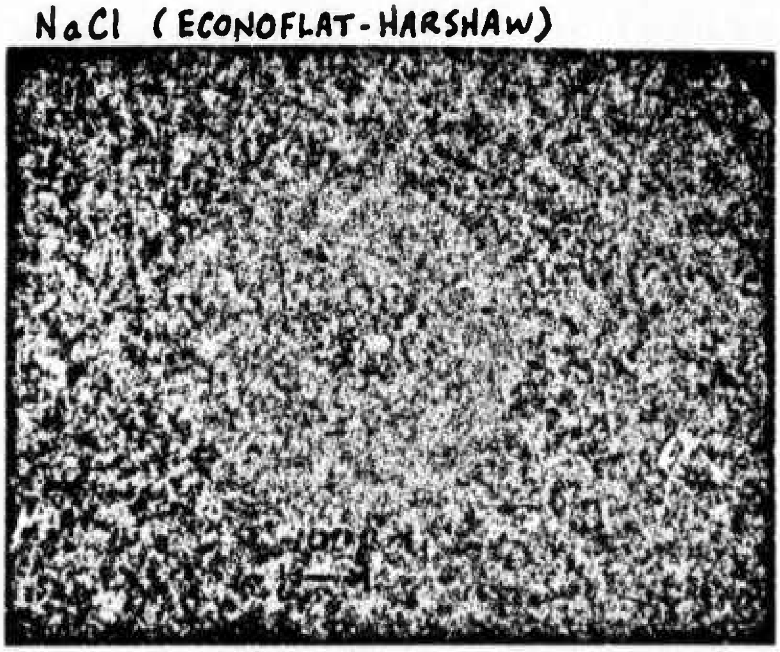

Figure 15. Damage site at threshold on a conventional surface of Harshaw NaCl observed under an optical microscope.

The Dependence of the Pulsed 10.6 μm Laser Damage Threshold on the Manner in which a Sample is Irradiated*

M. Bass and K. M. Leung
Center for Laser Studies
University of Southern California
Los Angeles, California 90007

The threshold for pulsed 10.6 μm laser induced surface and bulk damage in transparent materials has been shown to depend on the manner in which the samples are irradiated. When a site is irradiated several times, starting at a very low intensity and increasing the flux a few percent on successive shots until damage occurs, the threshold is often higher than if each site were irradiated only once. In addition, it has been shown that the damage threshold also depends on the sample tested and so the use of relative damage threshold measurements to identify the damage mechanism should be re-examined.

---

* This work was supported by the Defense Advanced Research Projects Agency and was monitored by the Air Force Cambridge Research Lab.

Thresholds for pulsed laser damage to transparent media have been determined in a variety of experiments. The importance of the beam's spatial mode and the pulse temporal waveform have been discussed.[1] There has also been extensive discussion of the relation between the size of the irradiated volume and the measured threshold.[2] In this paper we point out the importance of the number of times a site is irradiated in determining the reported damage threshold at 10.6 μm and how this fact affects comparisons between materials.

We have reported experiments in which each site was irradiated only once and the intensity was increased at each successive site until damage was produced with some degree of consistency (i.e., 50% of the sites are damaged).[3] Allen et al. reported damage thresholds obtained when each site was irradiated several times starting at a very low intensity and increasing the flux a few percent on successive shots until damage occurred.[4] Since our one shot on one site (1 on 1) and their several shots on one site (N on 1) experiments gave different results for the same materials, we have undertaken a direct comparison of these procedures on the same samples.

Our experiment is described in detail in Ref. 3 and is summarized in Table I. The results of our 1 on 1 and N on 1 comparison are given in Table II. Clearly when the diameter of the irradiated region is ~100 μm, the 10.6 μm laser damage threshold of ZnSe is independent of the manner of irradiation. KCl and NaCl, on the other hand, have higher damage thresholds when measured in an N on 1 experiment than in a 1 on 1 experiment. This increased threshold is observed for ~50% of the sites studied in both surface and bulk damage experiments. No dependence on interpulse interval was found for a range from 5 sec. to > 1 min.

As in Ref. 3, we also monitored the transmitted pulse waveform distortion during these experiments. We found that in an N on 1 experiment no distortion could be detected during any pulse prior to the one which produced a spark and left residual damage in the sample. The distortion of the last pulse was, in all respects, similar to that seen in a 1 on 1 damage measurement.

The increase in surface damage threshold in an N on 1 experiment might be due to either a cleaning of the surface by the laser at low intensities[5] or a smoothing out of the sharp edges of polishing scratches by some form of "laser polishing". If sharp edges are removed and "vee" like scratches become more nearly cylindrical, Bloembergen[6] would predict a ratio of damage intensities for N on 1 to 1 on 1 of

$$R = \frac{(\epsilon + 1)^2}{4}$$

where $\epsilon = n^2$ is optical frequency dielectric constant. R is the ratio of the square of Bloembergen's field enhancement factors for "vee" grooves to that for cylindrical grooves. Thus, for NaCl where n = 1.49, we should have $R_{NaCl} = 2.59$ and for KCl where n = 1.46 we should have $R_{KCl} = 2.45$. From Table II we see that the experimental ratios are 3.06-3.33 and 2.36 respectively. In other words, the change in the surface damage threshold between N on 1 and 1 on 1 experiments does not disagree with the "laser polishing" explanation. The fact that the surface damage threshold of ZnSe is independent of the type of experiment may be due to the fact that the damage mechanism in this material is absorption by particulate inclusions.[3] This mechanism is not sensitive to local field enhancement.

The foregoing model might explain the results for surface damage but does not suffice when we consider the results for bulk damage. The increased damage flux in an N on 1 experiment for bulk damage is both unexpected and troublesome. Consider, for example, the fact that the ranking of the two NaCl samples reverses when one goes from a 1 on 1 threshold to an N on 1 value. Consider, in addition, comparing KCl to NaCl. For each type of experiment one gets a different relative damage threshold. The fact that the relative damage threshold also depends on which samples are compared suggests that the use of such comparisons to identify the damage mechanisms[7] be re-examined.

In studying the statistics of laser damage, at 1.06 and 0.69 μm the site was irradiated several times with pulses of fixed intensity.[8] The irradiation continued until either damage occurred or until some predetermined number of pulses had been tried. At any particular intensity level the distribution of the number of pulses required to produce damage was given by the binomial distribution.[8,9] This is a characteristic of a process having a constant probability of occurrance on each trial. If low level irradiation caused an increase in the damage threshold of the materials studied at 1.06 and 0.69 μm, then the damage probability would not have been constant from pulse to pulse. The probability for damage would have decreased on each successive pulse so that if damage did not occur on the first pulse it would very likely not have occurred at all. The process would have appeared threshold-like instead of statistical. We feel, therefore, that the increased threshold in an N on 1 experiment at 10.6 μm does not conflict with the statistical properties of 1.06 and 0.69 μm laser damage. In fact, the statistics observed at the shorter wavelengths suggest that there would be no increase in threshold in an N on 1 experiment performed with either a Nd or a ruby laser.

The measured 10.6 μm laser damage threshold for both bulk and surface damage, in some materials has been shown to depend on the procedure used. This study has also shown that the relative ranking of materials according to their damage thresholds depends on which samples are compared and on the experimental procedure. As a result, the use of such rankings to identify the laser damage mechanism should be re-examined.

The authors acknowledge the assistance of C. Tang and M. Chang in this work. V. Wang participated in the initial experiments.

References

1. M. Bass, "Laser Induced Damage to Nonlinear Crystalline Materials," NBS Special Publication No. 341, 90 (Dec. 1970).
2. L.G. DeShazer, B.E. Newnam and K.M. Leung, "The Role of Coating Defects in Laser-Induced Damage to Thin Films," NBS Special Publication No. 387, 114 (Dec. 1973).
3. K.M. Leung, M. Bass and A.G.J. Balbin-Villaverde, "Damage to 10.6 μm Window Materials Due to CO_2 TEA Laser Pulses," presented at the 1975 Laser Damage Symposium, Boulder, Colorado, July 1975, and to appear in the proceedings of that meeting.
4. S.D. Allen, M. Braunstein, C. Giuliano and V. Wang, NBS Special Publication No. 414, 66 (Dec. 1974).
5. T.L. Barber, "Degradation of Laser Optical Surfaces," ECOM Report No. 5237 (March 1969).
6. N. Bloembergen, Applied Optics <u>12</u>, 661 (April 1973).
7. E. Yablonovitch, Appl. Phys. Letters <u>19</u>, 495 (Dec. 1971).
8. M. Bass and H.H. Barrett, IEEE J. Quantum Electr. <u>QE-8</u>, 338 (Mar. 1972).
9. M. Bass and D.W. Fradin, IEEE J. Quantum Electr. <u>QE-9</u>, 890 (Sept. 1973).

Table I. Summary of Experimental Parameters

Laser	CO_2 TEA
Wavelength	10.6 μm
Waveform	92 nsec gain switched pulse with self mode locked spikes $\lesssim$ 2.5 nsec duration and 8 nsec interpulse spacing
Transverse mode	TEM_{00}
Attenuation	ZnSe beamsplitter and two Brewster angle stacked plate polarizers
Focusing lens	Ge, 3.8 cm focal length, abberation free
Focal spot diameter	107 μm to $1/e^2$ in intensity
Detection system	Photon drag detectors and Tektronix 7844 Oscilloscope. Risetime = 2.5 nsec

Table II. Comparison of N on 1 and 1 on 1 Laser Damage Thresholds

		10.6 μm Damage Threshold* in GW/cm^2									
Material		ZnSe		KCl				NaCl			
Supplier and Supplier's Designation		Raytheon ZnSe 1975		Harshaw Econoflat Grade		HRL RAP Grown		Harshaw Econoflat Grade		Harshaw Spectrophotometer Grade	
		Surface	Bulk	Surface	Bulk	Surface	Bulk	Surface	Bulk	Surface	Bulk
Type of Experiment	N on 1	0.35	0.41	1.3	2.0	-	2.6	4.9	7.1	2.8	14.0
	1 on 1	0.35	0.46	.56	0.65	-	1.5	1.6	6.1	0.84	3.9
$R = \frac{I_{threshold}^{(N\ on\ 1)}}{I_{threshold}^{(1\ on\ 1)}}$		1.0	1.0	2.36	3.07	-	1.73	3.06	1.16	3.33	3.58

* Defined as that intensity which damages 50% of the sites.

Thermal Lensing

W. Steier, C. P. Christensen, R. Joiner

Thermal lensing experiments described in the previous report have been continued, and a rotating-mirror beam scanner has been constructed which allows continuous display of the radial profile of an optical beam. Anomolous lensing effects described in the previous report were found to arise from parasitic distortion in beam handling optics at high laser powers, and those problems were subsequently corrected.

In the current experimental set-up, the unfocussed output of a 50 w CO_2 laser is directed through the window sample and to the beam scanner, which is separated from the sample by a distance of 2m. The scanner uses a rotating mirror to sweep the beam across a pinhole aperature every 16 msec. A Ge:Au detector collects light transmitted through the pinhole, and the resulting signal is displayed on an oscillOscope. Timing circuitry triggered by the first scan is used to generate displays of the beam profile at selected times after sample illumination is begun. Examples of beam profiles obtained in this manner are shown in Fig. 1. For this Figure, the window sample was polished polycrystalline CdTe 5 cm in diameter by 13 mm thick with an absorption coefficient of 0.2 cm^{-1}. The laser power in the measurements was 30 watts. The Figure shows formation of a thermally-induced positive lens forming to a focal point which moves in from infinity to a point somewhere between the sample and the beam scanner, producing an on-axis intensity which first increases and then decreases. The side lobes on the beam profile which become very pronounced at long times are due to thermally-induced phase variations in the window which are not quadratic in the radial coordinate.

The radial intensity distribution at a distance z from the sample can be directly computed using the Kirchoff diffraction integral if the temperature profile in the sample is known. Assuming cylindrical symmetry, we have

$$I(r, z) \sim \left| \int_0^{\infty} x J_o(\beta r x)\, e^{-(1+ib)x^2/w^2}\, e^{-i\phi(x)}\, dx \right|^2$$

where

w = beam radius at sample = 3.3 mm

$b = \pi w^2 / \lambda z$

$\beta = \frac{2\pi}{\lambda} z$

$\phi(x)$ = phase shift from thermal effects

For CdTe the effects of thermally-induced strain and bulge are expected to be relatively small, so that a good first approximation in the absence of thermal conduction $(t < w^2/8D)$ is

$$\phi(x) = \frac{4\alpha L \quad P}{\pi w^2 \lambda} \frac{dn}{dT} e^{-x^2/w^2} t.$$

For the geometry used in obtaining Fig. 1, this approximation should hold for $t < 0.5$ sec.. Figure 2 shows intensity profiles obtained by numerical integration of the diffraction integral using parameters appropriate to Fig. 1. Good agreement is found to exist between the calculated and experimental results over the time interval in which conduction may be neglected. The onset of thermal conduction introduces much greater complexity into the theoretical calculations. However, a computer program is under development which will enable calculation of intensity profiles at arbitrary times.

Oriented, single crystal samples are in preparation which are expected to be useful in investigating strain effects in the thermal lensing measurements. Since these samples will be free of the uncertainties of characterization associated with polycrystalline samples, the lensing data obtained should also be well suited for comparison with the theory of Marburger and Flannery.

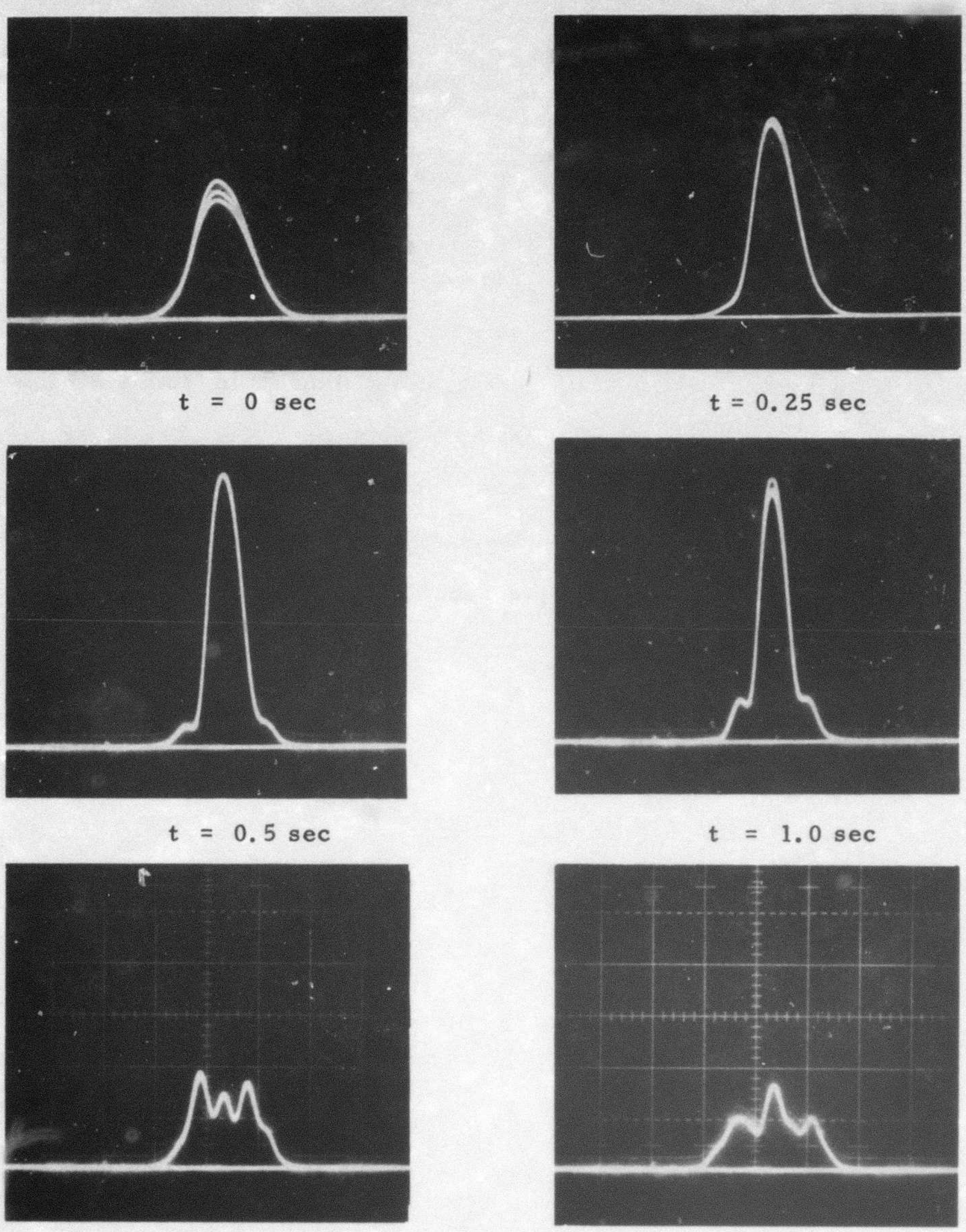

t = 0 sec

t = 0.25 sec

t = 0.5 sec

t = 1.0 sec

t = 5.0 sec

t = 10. sec

Fig. 1. Cross-sectional beam scans obtained 2 m from a CdTe window having $\alpha l = 0.25$. The laser power is 30 watts, and the beam radius at the sample is 3.3 mm.

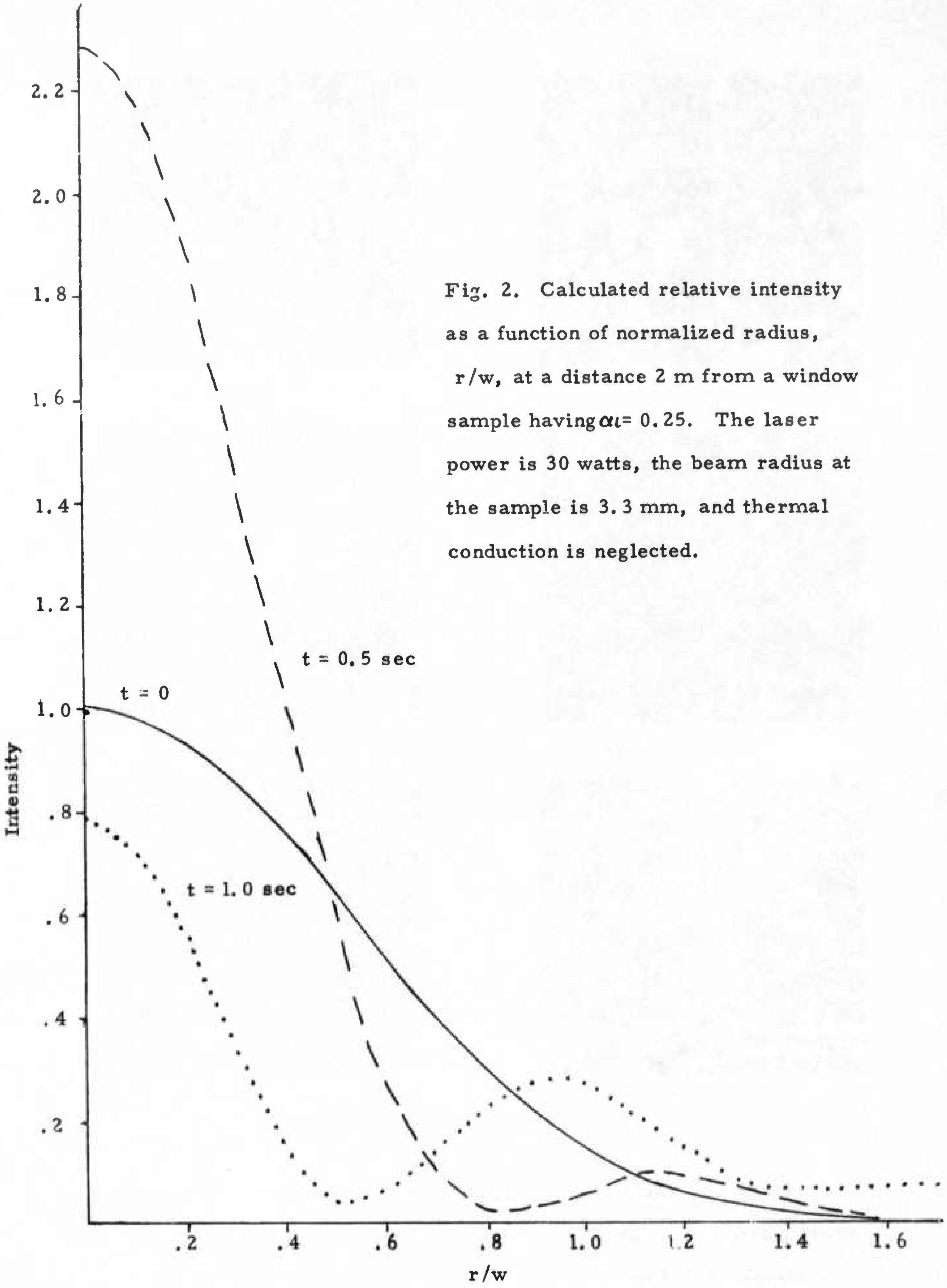

Fig. 2. Calculated relative intensity as a function of normalized radius, r/w, at a distance 2 m from a window sample having $\alpha l = 0.25$. The laser power is 30 watts, the beam radius at the sample is 3.3 mm, and thermal conduction is neglected.

Strain-Optic Tensors for Polycrystalline Aggregate Materials

J. Marburger and M. Flannery

In this report we continue the investigation of the optical properties of polycrystalline aggregates of cubic crystals. As described in Semiannual Report No. 1, our technique is to assume the polycrystalline aggregate is statistically homogeneous and isotropic and then compute the effective isotropic elastic and elasto-optic tensor components in terms of the single crystal tensor components.[1] We found this procedure to be well devloped and completely adequate for the elastic properties, but attempts to carry these results over directly to the corresponding elasto-optic tensor gave relatively poor results. In this report we describe our investigations into some of the averaging procedures used in the elastic problem, their applicability to the optical case, and an analysis of a number of real materials.

For cubic crystal classes $\bar{4}3m$, 432 and m3m, the strain-optic tensor and the stiffness tensor have identical forms except that the components of the stiffness tensor must obey the stability conditions:

$$C_{44} > 0, \quad C_{11} > |C_{12}|, \quad C_{11} + 2C_{12} > 0 \tag{1}$$

in order that the crystal structure be energetically stable.[2] These conditions are generally used at some point in derivations of effective isotropic stiffnesses because many of the methods are based on an energy variational technique and because the conditions produce great simplifications in the solutions. However, since the stability conditions are not obeyed by the components of the strain-optic tensor, we must be careful to acquire results from elastic theory before the conditions are applied.

We examined the derivation by Hershey[3] of the effective isotropic stiffness constants of cubic polycrystalline aggregates, and applied the results to the strain optic tensor.

We will state the results in terms of the optical variables which may be related back to the elastic problem by carrying out the replacements

$$p_{11} \rightarrow C_{11}, \quad p_{12} \rightarrow C_{12}, \quad p_{44} \rightarrow C_{44} \tag{2}$$

throughout. We define the cubic crystalline moduli by:

$$\begin{aligned} A &= (p_{11} + 2p_{12})/3 \\ B &= (p_{11} - p_{12})/2 \\ C &= p_{44}. \end{aligned} \tag{3}$$

Then the effective isotropic polycrystalline moduli, A* and B*, are given by Hershey's self-consistent averaging scheme as

$$A^* = A \tag{4}$$

and a root of

$$\begin{aligned} 64B^{*4} + 16(9A+2B)B^{*3} + 3(3A(9A+4B) - 8(A+4B)C)B^{*2} \\ - 3AB(9A+52B)B^* - 54A^2BC = 0. \end{aligned} \tag{5}$$

In the elastic case the stability condition (1) can be used to assure there is only one acceptable root of equation (5) and thus both elastic constants are fixed. Unfortunately in the optical case, while A* is fixed, there are as many as four possibilities for B*. This number can be reduced to a maximum of three if we use the cubic equation derived by Kroner, et al.,[4]

$$8B^{*3} + (9A+4B)B^{*2} - 2C(A+4B)B^* - 6ABC = 0 \tag{6}$$

which results from a self-consistent averaging of the inverse of the strain-optic tensor. Equations (5) and (6) are closely related to each other because it is possible to show analytically that the real roots of the cubic equation are included among the real roots of the quartic, but in the optical case it is not clear how one can pick out the remaining root of the quartic.

Finally we could try to identify the specific root of (5) or (6) by using the Hashin-Shtrikman[5] bounds (hereafter called HS bounds) which become:

$$
\begin{aligned}
B^*_- &= B + 3\left(\frac{5}{C-B} + \frac{12(A+2B)}{5B(3A+4B)} \right]^{-1} \\
B^*_+ &= C + 2\left(\frac{5}{B-C} + \frac{18(A+2C)}{5C(3A+4C)} \right]^{-1}.
\end{aligned}
\qquad (7)
$$

We have written these as upper, B^*_+, and lower, B^*_-, bounds, but in general they may switch positions. These bounds were derived from a variational principle for elastic energy which uses the stability conditions to guarantee the positive definite nature of the energy. Thus the validity of assuming that equations (7) represent bounds on B^* is in question and we can not assume they bound only the correct root. Suppose for the moment that one of the real roots of the cubic (6) is the correct value for the effective isotropic strain-optic coefficient B^*. We need to know when we will require the bounds to distinguish between multiple roots and if the expressions for the bounds remain valid for those cases.

First convert the cubic equation to the standard form

$$x^3 + ax + b = 0 \qquad (8)$$

where

$$x = \left(B^*/B + (9A+4B)/24\right). \qquad (9)$$

Now the solutions of (8) may be characterized by its discriminant

$$\Delta = \frac{b^2}{4} + \frac{a^3}{27} \qquad (10)$$

according to:

$\Delta > 0$; one real and two complex conjugate roots,
$\Delta = 0$; three real roots with at least two equal,
$\Delta < 0$; three real, unequal roots.

Thus if $\Delta > 0$, there is only one real root and we may take this as the correct value of B*. When $\Delta \leqslant 0$ there will be two or three real roots and we will need the bounds to specify the correct root. It is easy to show that if the components of the stress-optic tensor obey the stability conditions (1), then the discriminant is less than zero and the HS bounds will bracket the correct root as in the elastic case. However, there are still cases where $\Delta \leqslant 0$ while the tensor components do not obey (1), but we believe the HS bounds can still be used to designate the correct root.

Consider the following procedure. Suppose we have a cubic material with strain-optic tensor components that fail one or more of the stability conditions and also has $\Delta < 0$. Then we could arrive at these values for the tensor components by a smooth variation from a suitable set obeying the stability conditions which also have the physical root bracketed by the HS bounds. During this variation, the roots of (8) and the HS bounds will generally vary together in a smooth way such that a root of the cubic equation remains between the HS bounds. It seems reasonable to accept this root as the correct value for B* provided the variational procedure does not fail due to passing through any singularities in the expressions for the HS bounds, or because an additional root of the polynomial moves between the HS bounds. This second possibility could occur when $\Delta \to 0$ and two or three roots coalesce. Unfortunately the expressions for the HS bounds and for the discriminant are such complicated functions of three independent variables that we have not carried out the general variation described above.

Instead of trying to carry through the general analysis we decided to examine the available strain-optic data for real materials to see how the polynomial roots and HS bounds behaved. The strain-optic data and averaging calculations for thirteen materials are summarized in Table I.

First we examined the signs of the p_{ij}'s themselves and found no correlation with the space group of the crystal, but at a fixed frequency, series of compounds whose components come from specific columns of the periodic table, such as the alkali halides or the alkaline earth halides, have the same pattern of signs.

Further we find that only β-ZnS and germanium have strain-optic coefficients that obey the stability conditions, so there is a real reason to extend the elastic solutions.

In successive columns of Table I we have listed A, B, the sign of Δ, the HS bounds and the roots of the cubic equation (6) followed by the fourth root from (5). The first root listed in Table I is the physical root B* either because it is the only root of (6) or because it is the root that falls between the HS bounds. We can divide the materials in Table I into two rather different groups. The first group has: $\Delta < 0$, so there are three real roots of the cubic equation; both HS bounds are either positive or negative, they bracket one root, and they are not too widely spread; and B and C have the same signs. The second group has: $\Delta > 0$, so there is only one root of the cubic equation; the HS bounds bracket zero, and for KCl and KBr they do not include the root of the cubic equation; and B and C have opposite signs.

The second group is the one that would have particularly poor predictions for the thermal lensing behavior of the material if B* were allowed to vary within the HS bounds because the lensing parameters are poorly defined if the range of B* includes zero.[1] In this group the fact that B and C have opposite signs means that they cooperate to increase the isotropic optical defect, $\delta = \frac{1}{2}(p_{11}-p_{12})-p_{44} = B-C$, whereas in the first group they tend to decrease it. Since HS bounds B^*_- and B^*_+ are identical for $\delta = 0$, and tend to become widely spread as the isotropic defect becomes large in magnitude, we expect materials with $\Delta > 0$ to give poor predictions if we base them on the HS bounds.

There is one very disturbing point left: the HS bounds fail to bracket the root of the cubic equation for KCl and KBr. Although the HS bounds are not needed in these cases to specify the correct root, the failures led us to examine our results carefully.

First we calculated the simpler Voigt and Reuss bounds[7] on B*,

$$B^*_v = (2B + 3C)/5, \quad B^*_r = 5BC/(3B + 2C), \qquad (11)$$

as verification of the HS bounds. These bounds were developed in elastic theory assuming continuous strain and continuous stress, respectively, and were later shown by Hill[8] to be upper and lower bounds on the effective isotropic aggregate shear modulus. The VR bounds are listed in Table II and generally behave quite similarly to the HS bounds for each material. B* was found to lie outside the VR bounds only for LiF, KCl and KBr, but in the case of LiF, B* is outside by only ½%. This result gives us some confidence that the bounds may be correct.

Second, we calculated the effective isotropic strain-optic tensor components,

$$\begin{aligned} p^*_{11} &= A + 4B^*/3 \\ p^*_{12} &= A - 2B^*/3 \qquad\qquad (12) \\ p^*_{44} &= B^* = \tfrac{1}{2}(p^*_{11} - p^*_{12}) \end{aligned}$$

in order to compare them to the crystalline p_{ij}'s. It was thought that perhaps the averaging procedure might have difficulty with the large anisotropies that could result when B and C have opposite signs. To check this, we defined a normalized anisotropy

$$\delta' = \delta/||\overleftrightarrow{P}||^{\frac{1}{2}} = (B-C)/||\overleftrightarrow{P}||^{\frac{1}{2}} \qquad (13)$$

where $||\overleftrightarrow{P}||$ is the norm of the fourth rank strain-optic tensor,

$$||\overleftrightarrow{P}|| = P_{ijkl}P_{ijkl} \qquad (14)$$

or in terms of the matrix form of the strain-optic tensor,

$$||\overleftrightarrow{P}|| = p_{ij}p_{ij} = 3(p^2_{11} + 2p^2_{12} + p^2_{44}). \qquad (15)$$

The values of δ′ listed in Table II clearly indicate that KCl and KBr are not among the most anisotropic materials; in fact they are almost an order of magnitude more isotropic than CaF_2 and BaF_2. However, we expect that if a material is nearly isotropic, then δ′ is small and $p_{ij} \sim p^*_{ij}$, while if a material is highly anisotropic, δ′ is large and the p^*_{ij}'s may differ appreciably from the p_{ij}'s.

From Table II we find that except for KCl and KBr, the materials generally follow the relations;

$$|\delta'| \sim 0.25 \implies |p^*_{ij} - p_{ij}|_{max} < |\delta'|/3$$

$$|\delta'| \sim 1.00 \implies |p^*_{ij} - p_{ij}|_{max} < \tfrac{1}{2}|\delta'| \qquad (16)$$

$$|\delta'| \sim 7.00 \implies |p^*_{ij} - p_{ij}|_{max} < 2|\delta'|$$

while KCl and KBr would give,

$$|\delta'| \sim 1.00 \implies |p^*_{ij} - p_{ij}|_{max} < 3.5|\delta'|. \quad (17)$$

The large variations for KCl and KBr are rather unexpected and run contrary to our physical intuition when compared to the other materials.

Therefore we carefully checked all calculations and ruled out the possibility of either errors in computation or numerical sensitivity of the solutions. Then we examined the cubic equations of the four materials; KCl, KBr, CaF_2 and BaF_2, which have only one real root. CaF_2 and BaF_2 were found to have no local minima in their cubic equations, but KCl has one at $B^* = -0.0082$, and KBr one at $B^* = -0.0062$. If we calculate the p^*_{ij}'s on the basis of these values for B^*, we find:

Table III

	p^*_{11}	p^*_{12}	p^*_{44}
NaCl	1.2024	1.4788	-0.1382
KCl	1.6594	1.8003	-0.0705
KBr	2.0023	2.1139	-0.0558

We noted earlier that the alkali halides have similar patterns in the values of their crystalline strain-optic coefficients as seen in Table I. Thus we would expect the similarity of patterns found for their polycrystalline strain-optic coefficients in Table III, instead of the radical departure of the patterns of KCl and KBr from NaCl that we found in Table II.

It appears that we may have to include the values given by local minima of (5) and (6) as well as real roots among the possible solutions for B^*.

We emphasize that the derivations of equations (5) and (6) do not allow us to consider local minima among possible solutions to the original problems based in elastic theory. We conclude that we will have to carry out these derivations directly in terms of the optical variables, checking each step to be sure it holds for the optical case, before we can be certain of these results.

Finally, because of the difficulties with KCl and KBr, we have not yet calculated the thermal lensing parameters for the polycrystalline aggregates and compared them to calculations that used the cubic strain-optic tensor components as if they were isotropic tensor components. However, noting that the relative birefringence parameter, Δ_0, is proportional to B^*, we can see how this parameter changes merely by comparing it to B. In particular, CaF_2, BaF_2, KCl and KBr will all have about one third the birefringence predicted using crystalline p_{ij}'s.

TABLE I

OPTICAL PROPERTIES OF MATERIALS[6] (×10)

	λ(Å)	P_{11}	P_{12}	P_{44}	A	B	Δ
LiF	5893	0.16	1.30	-0.64	0.92	-0.57	< 0
NaCl	5893	1.10	1.53	-0.10	1.3867	-0.215	< 0
KCl	5893	2.10	1.58	-0.27	1.7533	0.26	> 0
KBr	5893	2.41	1.91	-0.23	2.0767	0.25	> 0
CaF_2	5893	-2.59	4.29	11.2	1.9967	-3.44	> 0
BaF_2	5893	-1.44	1.97	9.4	0.8333	-1.705	> 0
GaP	6328	-1.51	-0.82	-0.74	-1.05	-0.345	< 0
GaAs	1.15μ	-1.65	-1.40	-0.72	-1.4833	-0.125	< 0
β-ZnS	6328	0.91	-0.1	0.75	0.2367	0.505	< 0
Ge	10.6μ	2.7	2.35	1.25	2.4667	0.175	< 0
Si	?	-1.45	0.22	-0.74	-0.3367	-0.835	< 0
MgO	5890	-3.1	-0.7	-1.07	-1.5	-1.2	< 0
Diamond	5893	-4.3	1.9	-1.6	-0.1667	-3.1	< 0

TABLE I (continued)

OPTICAL PROPERTIES OF MATERIALS

(×10)

	B^*_-	B^*_+	B^*	Roots of polynomials in B^*		
LiF	-0.6132	-0.6155	-0.6143	0.5759	-0.7116	-1.0350
NaCl	-0.1405	-0.1365	-0.1382	0.1134	-1.4277	-1.5601
KCl	-0.2316	0.0895	-1.9833	min. at -0.082		-1.9716
KBr	-0.1789	0.1239	-2.3651	min. at -0.064		-2.3359
CaF_2	-34.3835	0.5125	-1.1511			-2.2463
BaF_2	-9.4107	1.7878	-0.4706			-0.9375
GaP	-0.5407	-0.5521	-0.5477	0.2181	1.6834	1.1813
GaAs	-0.3233	-0.4080	-0.3790	0.1337	1.9765	1.6687
β-ZnS	0.6379	0.6399	0.6391	-0.0994	-1.0584	-0.2663
Ge	0.4935	6.782	0.6157	-0.2005	-3.2777	-2.7750
Si	-0.7765	-0.7765	-0.7765	0.1403	1.4325	0.3788
MgO	-1.1203	-1.1202	-1.1202	0.4336	2.9741	1.6875
Diamond	-2.0799	-2.0454	-2.0630	0.0808	3.7196	0.1875

TABLE II

OPTICAL PROPERTIES OF MATERIALS

(×10)

	B_v^*	B_r^*	δ'	P_{11}^*	P_{12}^*	P_{44}^*
LiF	-0.6100	-0.6120	0.2069	0.1009	1.3295	-0.6143
NaCl	-0.1272	-0.1460	-0.2733	1.2024	1.4788	-0.1382
KCl	-1.4625	-0.0580	0.9941	-0.8911	3.0755	-1.9833
KBr	-0.9914	-0.0380	0.7640	-1.0768	3.6534	-2.3651
CaF_2	-15.9470	5.3440	-6.5027	0.4619	2.7641	-1.1511
BaF_2	-5.8557	4.9580	-6.4701	0.2059	1.1471	-0.4706
GaP	-0.5076	-0.5820	1.1164	-1.7803	-0.6849	-0.5477
GaAs	-0.2479	-0.4820	1.2837	-1.9887	-1.2307	-0.3790
β-ZnS	0.6281	0.6520	-1.1910	1.0888	-0.1894	0.6391
Ge	0.3616	0.8200	-1.3914	3.2876	2.0562	0.6157
Si	-0.7753	-0.7780	-0.3309	-1.3720	0.1810	-0.7765
MgO	-1.1185	-1.1220	-0.2191	-2.9936	-0.7532	-1.1202
Diamond	-1.9840	-2.2000	-1.6288	-2.9174	1.2086	-2.0630

REFERENCES

1. J. Marburger, M. Flannery, Semiannual Technical Report No. 1, AFCRL-TR-75-0236 (15 March 1975).

2. J. F. Nye, Physical Properties of Crystals, (Oxford University Press; London, Eng., 1967), p. 142.

3. A. V. Hershey, J. Appl. Mech. 21, 236 (1954).

4. E. Kroner, B. K. Datta, and D. Kessel, J. Mech. Phys. Solids, 14, 21-24 (1966).

5. Z. Hashin, S. Shtrikman, J. Mech Phys. Solids, 10, 343 (1962).

6. The data in the table comes from: CRC Handbook of Lasers, Robert J. Pressley, ed. (Chemical Rubber Co.; Cleveland, Ohio, 1971), p. 481; C. S. Sahagian and C. A. Pitha, Compendium on High Power Infrared Laser Window Materials, AFCRL-72-0170, (9 March 1972).

7. W. Voigt, Lehrbuch der Kristallphysik, Teuber, Berlin, 1910; and A. Reuss, "Calculation of the flow limit of mixed crystals on the basis of the plasticity condition of single crystals," ZAMM, 9, (1929), 49-58.

8. R. Hill, "The elastic behavior of a crystalline aggregate," Proc. Phys. Soc. (London), Ser. A, 65, (1952), 349-354.

DISCUSSION

The work performed under this contract may be divided into three categories: IR window material characterization, identification of window failure mechanisms (chemical and optical damage), and window system evaluation. We shall discuss each in turn.

A. IR Window Material Characterization.

Several novel microscopic techniques of potential value in window characterization were shown to be feasible in studies on ZnSe and GaAs. In one, scanning cathodoluminescence microscopy (SCM), grain boundaries, inclusions, and residual damage due to mechanical polishing are revealed. In another, SCM with modulation of the specimen current by optical illumination, deep impurity levels can be identified. Both techniques were employed on vapor grown ZnSe. Another microscopy investigation employed thin foil transmission electron microscopy to characterize the influence of post-growth annealing on impure CdTe and ZnSe. We found that massive inclusions and precipitates which occur particularly in early vapor grown ZnSe could be eliminated by annealing in a Se rich atmosphere. A Zn rich atmosphere also improved the structure, but introduced some residual dislocations.

Infrared absorption spectroscopy was used to locate a variety of absorption bands attributable to both single (Al,P) and double (P with In, Ga, Al, Cu) species in CdTe. In ZnSe only Al impurities were examined. The extent of each identified absorption band is included in the body of the report. Models for the defect structure of unconventionally doped CdTe (with P, Cr or Ge) were developed, and efforts made to reduce the 10.6μm absorption of Ge-doped CdTe below that of the more conventional In-doped material. The absorption decreases as expected with decreasing hole concentration until it reaches about the lowest value obtained in the In-doped material ($\beta \sim .005\text{cm}^{-1}$)

but then stops decreasing. The origin of the residual absorption is still unknown.

Other material measurements include determination of 10.6μm strain-optic coefficients for GaAs. These measurements are useful for testing the validity of theories used to extrapolate the values of such coefficients from their previously measured values in the near infrared (1.15μm). Two of the three independent coefficients were in good agreement with the theory, but the third, p_{12}, deviates by nearly 50% from the expected value. Sensitive measurements of the temperature and frequency dependence of the refractive index of ZnSe were also performed. This information is required for implementation of the scheme proposed by Hellwarth to determine the mechanism of multiphonon absorption in this material.

The surface acoustical wave technique for determining surface optical absorption was substantially perfected during this contract period, and has been used to determine surface absorption of KCl samples. The percentage of power lost in the surface (about .01% per surface) is comparable to the value of .02% for similar samples determined by length dependent calorimetry. Measurements made by this technique confirm the reduction of surface absorption by chemical etching, but indicate the existence of a residual layer of excess surface absorption even after substantial etching.

B. IR Window Failure Mechanisms.

The appreciable increase in 10.6μm absorption in NaCl windows exposed to atomic oxygen, observed by Prof. Wittig during the course of experiments on chemical laser action, was investigated more closely during this contract period. The effect is attributable to the formation of ClO_3 on the exposed surface. While strikingly large in NaCl, the effect is fortunately rather weak in KCl and KBr, but we do not understand why.

The extensive program of 10.6μm optical damage measurements undertaken by Bass and Leung has led to the conclusion that damage thresholds in KCl and ZnSe are still inclusion limited, but that the damage characteristics of recent vapor grown ZnSe samples have improved noticeably compared with earlier samples. By comparison, the limiting mechanism in commercially available NaCl is intrinsic (i.e. avalanche breakdown). We have also found that repeated irradiation of the same region, with incrementally increased flux on successive shots, leads often to higher thresholds for bulk and surface damage on alkali halides.

C. Window System Evaluation.

A series of quantitative experiments designed to test the thermal lensing theories which are commonly employed to derive figures of merit for window systems has verified the theory for simple lensing. Birefringence effects have still not been examined experimentally. Efforts to predict parameters necessary for the estimation of birefringence effects in polycrystalline materials have led to a prescription for determining effective isotropic parameters (e.g. elasto-optic tensor components) for an ideal polycrystal given the single crystal parameters. The scheme fails for the important cases of KBr and KCl, but can be modified to be generally applicable. Results for the effective parameters differ significantly in some cases from values assumed in elementary treatments of thermally induced birefringence.

PUBLICATIONS AND PRESENTATIONS

4.1 Publications

1. "The Dependence of the Pulsed 10.6μm Laser Damage Threshold on the Manner in Which a Sample is Irradiated," M. Bass and K.M. Leung, accepted for publication in IEEE Journ. of Quantum Electronics.

2. "The Defect Structure of CdTe: Self-diffusion Data," S.S. Chern and F.A. Kröger, J. Solid State Chem. 14, 44 (1975).

3. "The Relative Magnitude of the Diffusion Constants of Cd Vacancies and In-V_{Cd} Pairs in CdS and CdTe," S.S. Chern and F.A. Kröger, Phys. Stat. Solidi 25(a), 215 (1974).

4. "The Defect Structure of CdTe: Hall Data," S.S. Chern, H.R. Vydyanath and F.A. Kröger, Journ. Solid State Chem. 14, 33 (1975).

5. "Investigation of Infrared Loss Mechanisms in High Resistivity GaAs," C.P. Christensen, R. Joiner, S.T.K. Nieh and W.H. Steier, Journ. Appl. Phys., 45, 4957 (1974).

6. "Point Defects, Localized Vibrational Modes, and Free-carrier Absorption of Al-doped CdTe," B.V. Dutt, M. Al-Delaimi and W.G. Spitzer, accepted for publication in Journ. Appl. Phys.

7. "Localized Vibrational Modes of Al Paired with Cu, Ag or Au in ZnSe," B.V. Dutt and W.G. Spitzer, accepted for publication in Journ. Appl. Phys.

8. "Relation Between Optical Breakdown Field and Stokes Spectral Broadening," J. Marburger, Optics Commun. 14, 92 (1975).

9. "NaCl Surface Reaction in Chemical-Laser Devices," Alan B. Petersen and Curt Wittig, IEEE Journ. of Quantum Electronics, March 1975, p. 110.

10. "A Technique for Acoustic Surface Studies of Nonpiezoelectric Materials," D.A. Rockwell and J.H. Parks, J. Appl. Phys. 46, 5088 (1975).

11. "Theory of Acoustic Surface Wave Detection of Radiative Absorption," D.A. Rockwell and J.H. Parks, accepted for publication in Journ. Appl. Phys.

12. "Precipitation in Pure and Indium-doped CdTe as a Function of Stoichiometry," F.A. Selim, V. Swaminathan and F.A. Kröger, Phys. Stat. Solidi 29(a), 465 (1975).

13. "The Reaction of Alkali Halides with Active Oxygen," Dong Shim and Curt Wittig, accepted for publication in Applied Optics.

14. "Comment on 'Evidence of a Precipitatelike Zone in As-grown GaAs and Its Influence on Optical Absorptivity'," V. Swaminathan, G.H. Narayanan, and S.M. Copley, Journ. Appl. Phys. 46, 3687 (1975).

15. "Diffuse Streaks in the Electron Diffraction Patterns from CdTe Single Crystals," V. Swaminathan, G.H. Narayanan, and S.M. Copley, Journ. Appl. Phys. 46, 3716 (1975).

16. "Effect of Heat Treatment on the Microhardness of Indium-doped CdTe Single Crystals," V. Swaminathan, F.A. Selim and F.A. Kröger, Phys. Stat. Solidi 30(a), 721 (1975).

4.2 Presentations

1. "Influence of Crystal Anisotropy on Composite Window Design for Reducing Thermal Distortion," B. Bendow, P.D. Gianino, M. Flannery, J. Marburger, in Proceedings of the Fourth Laser Window Conference, Tucson, Ariz., 1974.

2. "A Quantitative Experimental Investigation of Thermal Lensing," C. Christensen, W. Steier and R. Joiner, Proceedings of the Fifth Laser Window Conference, Las Vegas, Nev., Dec. 1975 (to be published).

3. "Impurity Induced Absorption in P-doped CdTe," B.V. Dutt and W.G. Spitzer, Proceedings of the Fifth Laser Window Conference, Las Vegas, Nev., Dec. 1975 (to be published).

4. "Diffraction Theory of Absorbing Windows," M. Flannery and J. Marburger, Proceedings of the 1974 Conference on Laser Induced Damage in Optical Materials, NBS Special Publication (1975).

5. "Theory of Stress Induced Birefringence in Polycrystalline IR Window Materials," M. Flannery and J. Marburger, Proceedings of the Fifth Laser Window Conference, Las Vegas, Nev., 1975 (to be published).

6. "Measurement of Strain-optic Coefficients by Acousto-optic Interactions in Window Materials," R. Joiner, W. Steier and C. Christensen, Proceedings of the Fifth Laser Window Conference, Las Vegas, Nev., Dec. 1975 (to be published).

7. "Single Crystal CdTe as a CO_2 Laser Window," F.A. Kröger, Proceedings of the Fifth Laser Window Conference, Las Vegas, Nev., Dec. 1975 (to be published).

8. "Damage to 10.6μm Window Materials Due to CO_2 TEA Laser Pulses," K.M. Leung, M. Bass and A.G.J. Balbin-Villaverde, Laser Damage Symposium, Boulder, Colorado, 1975.

9. "Determination of Multiphonon Absorption Mechanism by Refractive Index Measurements," M. Mangir and R. Hellwarth, Proceedings of the Fourth Conference on High Power IR Laser Windows, Tucson, Ariz., 1974.

10. "Experimental Determination of Multi-Phonon Absorption Mechanism and Parameters in CVD Zinc Selenide," M. Mangir and R. Hellwarth, Proceedings of the Fifth Laser Window Conference, Las Vegas, Nev., 1975 (to be published).

11. "Surface Studies with Acoustic Probe Techniques," D.A. Rockwell, T.S. Colbert and J.H. Parks, Proceedings of the International Conference on Optical Properties of Highly Transparent Solids, ed. by S.S. Mitra and B. Bendow, Plenum Press, New York, 1975, p. 493.

12. "Identification and Elimination of Impurity-induced 10.6μ Absorption in KBR," P.J. Shlichta, J. Yee, R.E. Chaney, Proceedings of the Fourth Annual Conference on Infrared Laser Window Materials, Tucson, Ariz., 1974. p. 173.

13. "The Charging of Semi-insulating Specimins in Electron Microscope Instruments," D.B. Wittry and C.J. Wu, Proceedings of the 8th Annual Scanning Electron Microscope Symposium, IIT Research Institute, 1975, pp. 441-445.

14. "Measurement of Surface Voltages Using the Voltage Dependence of X-ray Intensities," C.J. Wu and D.B. Wittry, Proceedings of the 10th National Conference on Electron Probe Analysis, Las Vegas, Nev., 1975.

4.3 Reprints and Manuscripts

1. "Theory of Elasto-optic Coefficients in Polycrystalline Materials," M. Flannery, J. Marburger, submitted to Appl. Phys. Letters. (This paper contains material also included in the Proceedings of the Fifth Laser Window Conference.)
2. "Surface Acoustic Wave Velocity Dispersion Induced by Radiative Absorption," J.H. Parks, D.A. Rockwell, submitted to Journ. Appl. Phys.
3. "Studies of Radiative Absorption at KCl Surfaces Using Acoustic Techniques," D.A. Rockwell and J.H. Parks, submitted to Appl. Phys. Lett.